UNIVERSITÀ
DEGLI STUDI
DI BRESCIA

DIPARTIMENTO DI INGEGNERIA DELL'INFORMAZIONE

DOTTORATO DI RICERCA IN INGEGNERIA DELL'INFORMAZIONE

CURRICULUM:
INGEGNERIA ELETTRONICA, SENSORI E STRUMENTAZIONE

ING-INF/01 ELETTRONICA

XXXVI CICLO

TESI DI DOTTORATO DI RICERCA

TECHNIQUES, CIRCUITS AND DEVICES FOR NONCONTACT SENSING THROUGH WIRELESS COUPLING

Dottorando:

Marco ZINI

Supervisori: *Prof. Vittorio FERRARI*
Prof. Marco FERRARI

Ringraziamenti

Non sempre riusciamo a dire tutto ciò che vogliamo. A volte le parole ci sfuggono, si perdono nel vento o restano intrappolate nel labirinto dei nostri pensieri. Ma anche se le parole non trovano la loro strada verso l'esterno, i sentimenti continuano a vivere. È nel battito del cuore, nel calore di uno sguardo, nella gentilezza di un gesto che troviamo la vera espressione della nostra gratitudine e ammirazione. Anche quando le parole possono mancare, il sentimento rimane inciso nell'anima, un tesoro prezioso che nulla può cancellare.

Partendo da queste parole, prima di procedere all'esposizione del lavoro di Tesi conclusivo del mio Dottorato di Ricerca, voglio dedicare questo piccolo spazio per ringraziare tutti coloro che mi hanno permesso di portare a termine anche questa esperienza.

Il ringraziamento più grande va sicuramente alla mia Famiglia. Non so trovare le parole giuste per ringraziare i miei genitori e tutta la mia Famiglia, però vorrei che questo mio traguardo possa essere un premio anche per loro e per gli insegnamenti che mi hanno sempre trasmesso. Un infinito grazie per esserci sempre, per sostenermi, per avermi indirizzato verso la giusta strada. Senza di voi certamente non sarei la persona che sono.

Un ringraziamento va poi ai Supervisori di questa Tesi e a tutto il gruppo di ricerca con cui ho collaborato per la loro immensa pazienza e disponibilità, per i loro indispensabili consigli e per le conoscenze condivise durante tutto il dottorato e in particolare nella stesura di questo elaborato.

Un ringraziamento speciale lo devo alla Famiglia Universitaria, o meglio all'Effeu, che non mi ha semplicemente ospitato durante questi anni di studi a Brescia, ma mi ha permesso di vivere intensamente e con serenità questo periodo della mia vita e mi ha spinto a crescere non solo dal punto di vista accademico, ma anche dal punto di vista umano e relazionale.

Un ringraziamento particolare lo devo a Don Roberto, che in questi anni mi ha accompagnato e sostenuto con grande amicizia e disponibilità insegnandomi a cogliere e a coltivare tutti gli aspetti belli della vita.

In generale ci tengo a ringraziare tutti coloro che ho incontrato durante questo percorso di studi e che in qualche modo hanno contribuito al raggiungimento di questo ulteriore traguardo della mia vita.

Cerco sempre di fare ciò che non sono capace di fare,
per imparare come farlo – Pablo Picasso

Sintesi

Le tecnologie per la misurazione di grandezze fisiche senza contatto sono diventate sempre più centrali in vari settori, che vanno dal monitoraggio industriale alle applicazioni sanitarie. In questo contesto, la tesi si concentra sullo sviluppo e l'implementazione di tecniche innovative, circuiti elettronici e dispositivi per la rilevazione senza contatto.

L'analisi presentata all'interno di questa tesi considera lo scenario del rilevamento senza contatto a distanza nel campo elettromagnetico lontano (far-field) e al rilevamento senza contatto di prossimità, sfruttando le interazioni elettromagnetiche in campo vicino (near-field). Ogni scenario è distintamente caratterizzato dalle proprie specifiche tecnologie, applicazioni e metodologie, riflettendone gli ambiti operativi e i principi alla base del loro funzionamento. Nell'ambito del rilevamento senza contatto a distanza, la tesi indaga l'uso delle onde elettromagnetiche per il monitoraggio non invasivo del livello di solidi granulari all'interno di silos. Questo sistema, sviluppato impiegando un sensore radar commerciale a onda continua modulata in frequenza, dimostra il potenziale di questa tecnologia nel monitoraggio non invasivo e senza contatto in contesti agricoli e industriali.

Considerando invece lo scenario del rilevamento senza contatto di prossimità, la tesi fornisce un'analisi dell'interrogazione senza contatto di sensori passivi e ne presenta diversi approcci e applicazioni. Vengono affrontate le problematiche delle misurazioni senza contatto, proponendo alcune soluzioni per migliorarne l'affidabilità e l'accuratezza, permettendo in particolare di renderle indipendenti dalla distanza di interrogazione. La tecnologia proposta risulta particolarmente rilevante nello sviluppo di dispositivi a basso costo, usa e getta e sostenibili, per applicazioni cha vanno dal campo sanitario a quello industriale.

In particolare, la tesi presenta un sistema per la misurazione senza contatto della frequenza di risonanza di risonatori MEMS piezoelettrici. La tecnica proposta sfrutta l'accoppiamento magnetico tra un'unità di interrogazione ed un'unità sensore ed è applicata in modo innovativo per la rilevazione della temperatura, sfruttando le proprietà dei risonatori a disco in nitruro di alluminio (AlN) su silicio sottile piezoelettrico (TPoS) ed una tecnica di interrogazione senza contatto a tempo commutato.

Inoltre, la tesi presenta un'etichetta flessibile per la misurazione della temperatura corporea, che combina il rilevamento a contatto della temperatura con una lettura senza contatto dell'unità sensore sfruttandone l'accoppiamento magnetico con un unità di interrogazione. L'etichetta flessibile, che costituisce l'unità sensore, è composta da una bobina induttiva che consente l'accoppiamento magnetico, un condensatore ceramico utilizzato come elemento sensibile alla temperatura, sfruttandone il coefficiente di temperatura della capacità, ed un induttore aggiuntivo utilizzato per rendere la frequenza di risonanza del circuito risonante RLC indipendente dalla flessione dell'etichetta.

In modo analogo, le tecniche di interrogazione proposte sono state applicate ad un nuovo metodo per l'interrogazione senza contatto di un sensore induttivo, utilizzato per rilevare target conduttivi. Il sistema proposto presenta una bobina avvolta collegata con un condensatore per formare un circuito LC risonante, la cui frequenza di risonanza cambia quando un target conduttivo viene introdotto nel campo magnetico generato dalla bobina stessa. Attraverso una bobina di interrogazione esterna, accoppiata elettromagneticamente al sensore induttivo, è possibile interrogare senza contatto il sensore induttivo, permettendo quindi la rilevazione a distanza di target conduttivi.

Infine, lo studio esposto in questa tesi introduce una tecnica avanzata per l'interrogazione senza contatto di sensori resistivi passivi, sfruttando risonatori a cristallo di quarzo come dispositivo risonante e basandosi sulla stima del fattore di qualità del circuito che costituisce l'unità sensore. Il metodo proposto supera i limiti delle tecniche basate su misure di ampiezza, legati in particolare all'influenza della distanza di interrogazione.

In conclusione, le attività di ricerca descritte nella tesi riguardano gli sviluppi tecnologici dei sistemi per la rilevazione senza contatto e ne dimostrano la versatilità ed il potenziale in un'ampia gamma di applicazioni. L'integrazione di tecnologie innovative utilizzate nei sensori con metodi computazionali sempre più avanzati posiziona la rilevazione senza contatto tra le tecnologie sempre più fondamentali, destinato a guidare le future innovazioni nel settore della sensoristica, dall'ambito industriale fino al campo sanitario.

Abstract

Noncontact sensing technologies have become increasingly central in a variety of fields, ranging from industrial monitoring to healthcare applications. In this context, the thesis focuses on the development and implementation of innovative techniques, electronic circuits, and devices for contactless sensing via wireless coupling, responding to the growing interest in noncontact measurement methods.

The themes treated in this thesis regard both the scenario of distant noncontact sensing in the electromagnetic far field, and proximate wireless sensing, leveraging on near-field electromagnetic interactions. Each domain is distinctly characterized by its specific technologies, applications, and methodologies, reflecting their operational ranges and fundamental principles. In the domain of distant wireless sensing, the thesis investigates the use of electromagnetic waves for unobtrusive level monitoring of granular solids in silos. This system, developed employing a commercial frequency-modulated continuous-wave radar sensor, demonstrates the potential of this technology in unobtrusive monitoring in agricultural and industrial environments.

Considering the proximate wireless sensing domain, the thesis provides an analysis of noncontact interrogation of passive sensors and it presents different approaches and applications. It addresses the challenges and offers solutions for enhancing the reliability and accuracy of contactless measurements, which can be advantageously independent of the interrogation distance. This can path the way to the development of low-cost, disposable and sustainable devices for healthcare and industrial applications.

In particular, the thesis presents a system for the noncontact measurement of the resonant frequency of piezoelectric MEMS resonators. The technique exploits magnetic coupling

between interrogation and sensor units, and it is innovatively applied for temperature sensing exploiting a thin-film piezoelectric on silicon (TPoS) aluminium nitride (AlN) disk resonators and a contactless interrogation time-gated technique.

Furthermore, the thesis presents a flexible patch for body temperature measurement, combining contact sensing with contactless readout, and exploiting magnetic coupling between interrogation and sensor units. The flexible patch, forming the sensor unit, is composed of an inductive coil for magnetic coupling, a ceramic capacitor used as the temperature sensing element exploiting its temperature coefficient of capacitance and an additional inductor to make the resonant frequency of the resulting resonant RLC circuit independent from the bending of the patch.

Similarly, interrogation techniques have been applied to a novel method for contactless interrogation of an inductive sensor used for detecting conductive targets. The system features a solenoidal coil connected with a capacitor to form a resonating LC circuit, whose resonant frequency changes when a conductive target is introduced in the generated magnetic field. An external interrogation coil electromagnetically coupled to the inductive sensor enables the wireless measurement for conductive target detection.

Lastly, the study introduces an advanced technique for the contactless interrogation of passive resistive sensors. The novel approach exploits the resonant frequency stability and the high quality factor of a quartz crystal resonator, used as a resonant element, with a series-connected resistor acting as the sensing element. This method overcomes the limitations of amplitude measurements techniques typically affected by the interrogation distance.

In conclusion, the research activities treated in the thesis concern the technological advancements of noncontact sensing systems through wireless coupling, and demonstrate their versatility and potential across a wide range of applications. The integration of innovative sensor technologies with noncontact sensing approach, can further extend the sensing application possibilities, from industrial up to healthcare fields.

List of publications

The research activities reported in this PhD thesis have led to the following publications.

International journals:

[R01] **Zini, M.**; Baù, M.; Nastro, A.; Ferrari, M.; Ferrari, V. “Flexible Passive Sensor Patch with Contactless Readout for Measurement of Human Body Temperature”. Biosensors 2023, 13, 572. https://doi.org/10.3390/bios13060572

Proceedings of international conferences:

[I03] **Zini, M.**; Baù, M.; Nastro, A.; Ferrari, M.; Ferrari, V.; "Inductive sensor with contactless interrogation for conductive target detection", XXXV Eurosensors conference, Lecce (Italia), 11-13 September 2023, Proceedings 2024, vol. 97, no. 1, Art. no. 1, DOI: 10.3390/proceedings2024097095.

[I02] Baù, M.; **Zini, M.**; Nastro, A.; Ferrari, M.; Ferrari, V.; "Electronic technique and system for non-contact reading of temperature sensors based on piezoelectric MEMS resonators," IEEE International Symposium on Circuits and Systems (ISCAS), Texas, 28 May – 1 June 2022, , DOI: 10.1109/ISCAS48785.2022.9937328.

[I01] **Zini, M.**; Baù, M.; Ferrari, M.; Ferrari, V.; “Flexible Passive Sensor Patch with Contactless Readout for Measurement of Human Body Temperature” V

International Workshop “quantum & Biomedical Applications, Technologies and Sensors”, Switzerland, 20-21 June 2022.

Proceedings of national conferences:

[N04] **Zini, M.**; Baù, M.; Nastro, A.; Ferrari, M.; Ferrari, V.; "Inductive sensor with contactless interrogation for conductive target detection", 54rd Annual Meeting of the Associazione Società Italiana di Elettronica (SIE), Noto (Italia), 6-8 September 2023.

[N03] **Zini, M.**; Baù, M.; Nastro, A.; Ferrari, M.; Ferrari, V.; "Flexible Passive Sensor Patch with Contactless Readout for Measurement of Human Body Temperature", 53rd Annual Meeting of the Associazione Società Italiana di Elettronica (SIE), Pizzo Calabro (Italia), 7-9 September 2022.

[N02] **Zini, M.**; Baù, M.; Scubla, F.; Loda, M.; Stefini, G.; Nastro, A.; Ferrari, M.; Ferrari, V.; “Radar sensor system for unobtrusive level monitoring of granular solids stored in silos”, 53rd Annual Meeting of the Associazione Società Italiana di Elettronica (SIE), Pizzo Calabro (Italia), 7-9 September 2022.

[N01] **Zini, M.**; Baù, M.; Scubla, F.; Loda, M.; Stefini, G.; Nastro, A.; Ferrari, M.; Ferrari V.; “Radar sensor system for unobtrusive level monitoring of granular solids stored in silos”, XXI Conferenza Nazionale Sensori e Microsistemi (AISEM 2022), Rome (Italy), 10-11 February 2022, Lecture Notes in Electrical Engineering, vol 999. Springer, Cham. https://doi.org/10.1007/978-3-031-25706-3_24 .

Awards

The research activities carried out during the PhD course have led to the following awards:

- The paper entitled *"Flexible Passive Sensor Patch with Contactless Readout for Measurement of Human Body Temperature"*, M. Zini, M. Baù, A. Nastro, M. Ferrari and V. Ferrari has been awarded with the "Best paper Award" at the *V International Workshop on: Quantum & Biomedical Applications, Technologies and Sensors* (qBATS).held in Lugano (Switzerland), 20-21 June 2022.

Table of contents

Chapter 1

Introduction on noncontact sensing

Noncontact sensing is an emerging field with growing relevance in many areas, offering significant advancements over traditional wired solutions. This technology enables measurement and monitoring in environments where physical connections are either impractical or inconvenient. The key advantage of noncontact sensing lies in its ability to operate without direct physical connections, broadening the range of applications from industrial automation up to healthcare diagnostics. An overview on noncontact sensing system is reported in this chapter, focusing on battery-free systems in two main different scenarios: distant noncontact sensing and proximate noncontact sensing. The main technology utilized in these scenarios are reported to give an introduction of the topics reported in the successive chapters.

1.1 Noncontact sensing systems

Noncontact sensing systems represent a growing frontier in the field of data acquisition and environmental monitoring, marking a significant shift from traditional, cabled sensing solutions. At the heart of noncontact sensing lies its ability to gather information without the need of physical connections. This capability has opened new frontiers in numerous fields, ranging from environmental monitoring and healthcare to industrial automation and consumer electronics. The market for noncontact sensors has been expanding, driven by an increasing demand for real-time monitoring and automation solutions. This growth is not only a testament to their utility but also points to their potential future impact.

Noncontact sensing can be based on either mechanical waves, such as acoustic waves, or electromagnetic waves, ranging from radio frequencies to gamma rays, each offering unique capabilities for diverse applications.

In the realm of electromagnetic waves, the concept of noncontact sensing can be broadly divided into two distinct domains based on the operational range: distant noncontact sensing in the far field and proximate noncontact sensing in the near field. This division is not merely a measure of physical distance but reflects a fundamental difference in the underlying technologies, applications, and methodologies of these systems.

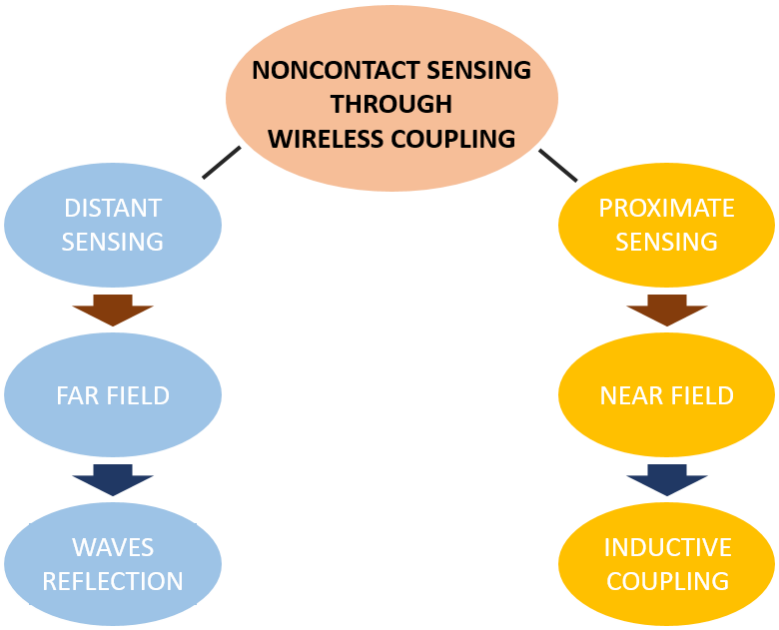

Figure 1.1 – Overview of electromagnetic noncontact sensing scenarios.

Distant noncontact sensing, operating in the far-field region, encompasses technologies that detect and analyse phenomena or objects at considerable distances. This form of sensing leverages the propagation and reflection characteristics of mechanical or electromagnetic waves, extending the reach of sensors to vast and inaccessible areas. Far-field noncontact sensing finds its applications in diverse fields, from environmental monitoring to space exploration, where direct access is either impractical or impossible.

In contrast, proximate noncontact sensing, functioning in the near-field region, focuses on data acquisition within a relatively short range. This type of sensing relies on the principles of electromagnetic and mechanical near-field interactions. Near-field sensing is particularly advantageous in applications where localized data are crucial. It plays a significant role in scenarios like healthcare monitoring, where sensors need to operate in close proximity to the subject without causing discomfort or intrusion.

Both distant and proximate noncontact sensing technologies are instrumental in creating less invasive and smarter sensing systems, particularly in enclosed environments or applications that require through-wall sensing. This is especially apparent in scenarios where traditional sensing methods face challenges, such as in hostile areas or when monitoring moving targets. Noncontact sensors, capable of functioning through barriers or from a distance, facilitate continuous monitoring and data collection without compromising the integrity of the space or target being observed. This approach not only enhances the safety and effectiveness of the monitoring process but also contributes to the development of more adaptive and responsive sensing systems aligning with the ongoing trend towards creating smarter and more integrated technological systems.

1.2 Distant noncontact sensing

Distant noncontact sensing, one of the scenarios of noncontact sensing through wireless coupling, involves the detection and characterization of objects or phenomena at significant distances from the sensor. This technology generally leverages mechanical or electromagnetic waves to observe and analyse targets in the far-field region, which is generally defined as a distance greater than several wavelengths from the source [1].

Mechanical wave-based distant sensing primarily relies on acoustic or seismic waves. These waves, generated naturally or artificially, travel through mediums like air, water, or the earth crust, interacting with objects or features along their path, as shown in Figure 1.2. By analysing the reflected or refracted waves, these systems can deduce valuable information about the properties of the target, such as its location, composition, and structural integrity.

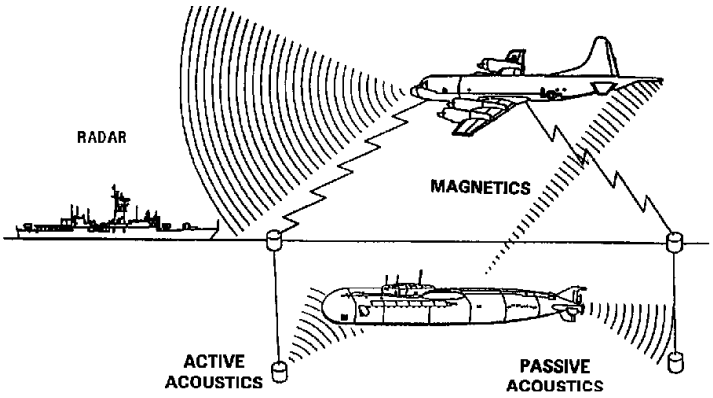

Figure 1.2 – Examples of mechanical and electromagnetic wave-based noncontact distant sensing [2].

Applications of mechanical wave-based sensing include level and target positioning monitoring [3], structural health monitoring of infrastructure [4], medical imaging [5,6], and many other application in industrial [3,7] and automotive [8–10] fields.

Electromagnetic wave-based sensing, on the other hand, utilizes the spectrum of electromagnetic radiation, which includes radio waves, microwaves, infrared, visible light, ultraviolet, X-rays, and gamma rays, as shown in Figure 1.3 [11]. The choice of wavelength depends on the specific application and the nature of the information required. For instance, radar systems use radio or microwaves to detect and locate objects, while optical and infrared sensors are employed in applications ranging from environmental monitoring to astronomical observations.

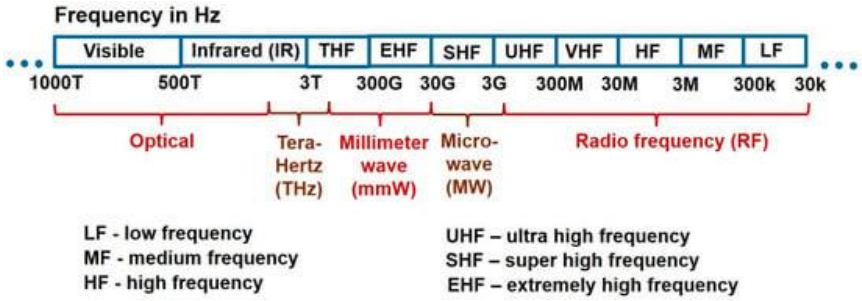

Figure 1.3 – Electromagnetic spectrum showing the radio frequency, millimeter wave, microwave, terahertz, infrared and visible band ranges [11].

Key to the operation of noncontact sensing systems in the far-field region is their reliance on the propagation characteristics of electromagnetic waves, such as reflection, scattering, and diffraction, which occur when these waves interact with objects in their path [12]. By analysing the altered waves, these systems can extract valuable information about the properties and dynamics of the target, such as size, shape, distance, speed, and material composition. Electromagnetic waves-based sensing is extensively used in satellite remote sensing [13], military and security applications [14], environmental monitoring [15], industry [16,17], automotive [18], agriculture [19], and also bio-medical applications [11,20].

The advancement in distant noncontact sensing technologies is driven by innovations in sensor design, signal processing techniques, and data analysis algorithms. The integration of these systems with advanced computational methods, such as machine learning and artificial intelligence, has further expanded their capabilities. These improvements have enabled higher resolution, greater accuracy, and the detection of a broader range of frequencies, thereby expanding the scope and efficiency of these systems.

1.2.1 Radar sensors

Radar (Radio Detection and Ranging) sensors represent a pivotal technological domain that spans an extensive range of applications, from long-range detection, for example in satellite and airport surveillance, to short-range uses, for example in speed and position detection and through-wall measurements. The first radars were developed as early as the 1930s [21]. However, in the early years, their use limited in the military sector due to their bulky sizes and high costs [21]. These sensors, functioning on the principle of emitting radio waves and analysing the echoes received from objects, have significantly evolved since their inception, adapting to a multitude of operational environments.

Radar sensors working up to K-band are generally used in applications requiring extensive spatial coverage and high-altitude detection capabilities. For instance, in satellite technology, they play a critical role in earth observation, weather forecasting, and space exploration, providing vital data from vast distances [22,23]. Figure 1.4 show the principle of operation of a weather radar.

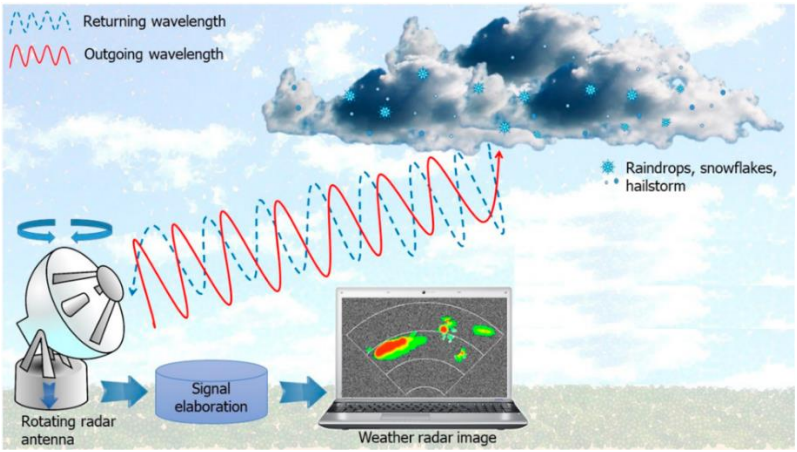

Figure 1.4 – Weather radar principle of function.

Similarly, in aviation, airport surveillance radars are indispensable for air traffic control, offering the ability to track and manage aircraft movements over large distances, ensuring safety and efficiency in airspace management [24].

Conversely, millimeter wave radar sensors, operating at higher frequencies as shown in Figure 1.5, offer finer resolution and are adept at detecting and measuring objects within a limited spatial domain. These sensors are increasingly employed in various sectors including automotive, for applications such as collision avoidance systems, speed control, and parking assistance [18]. Additionally, their capability to penetrate different materials renders them precious in through-wall sensing applications, widely used in security, rescue operations, and structural health monitoring [20,25,26].

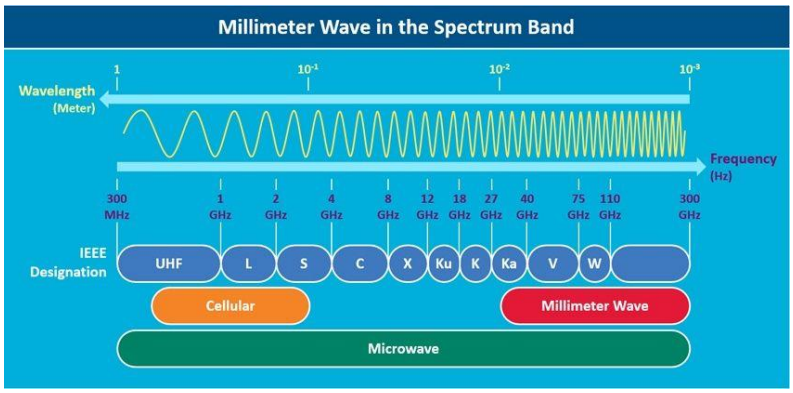

Figure 1.5 – Millimeter wave in the frequency spectrum band [27].

All type of radar sensors share a common foundation in their operational principle but differ significantly in their technical implementation, frequency bands, and application areas. This diversity underscores the versatility of radar technology and its integral role in advancing various aspects of modern society.

1.2.2 Millimeter wave radar

Millimeter wave radar sensors are a pivotal technology in the field of distant noncontact sensing. Initially confined to military applications due to their size and cost, advancements in high-frequency integrated circuits (IC) and monolithic microwave integrated circuits (MMIC) have revolutionized these systems [28,29]. Today, they can be miniaturized and integrated onto printed circuit boards (PCBs), with advancements even allowing for the integration of entire radar systems into single chips using antenna-on-chip (AoC) or antenna-in-package (AiP) technologies [30].

The operation frequencies of radar systems have shifted to higher bands, such as the K-band (24 GHz) and W-band (77 GHz). Higher frequencies has not only improved sensitivity and resolution but also allowed for further compactness of radar systems. These developments have broadened the applications of radar technology from strictly military to diverse commercial areas [31].

Radar systems have become instrumental in unobtrusive through-wall detection [25,26], indoor localization [32], driver assistance [18] and also bio-medical applications [20]. Their microwave signal penetration capability makes them invaluable in scenarios that require unobtrusive detecting. Radar systems, in contrast to camera-based technologies, ultrasound systems and infrared technology, can effortlessly provide accurate information on target ranges, speeds, and angles [31].

One of the main features of millimetre wave radars is their high resolution. Operating at higher frequencies compared to X-band radars, they can detect smaller objects and offer finer resolution. They are also particularly robust against environmental factors such as fog,

rain, or dust, making them reliable in various conditions. Another advantage is their compact size, making them ideal for integration into a variety of devices and platforms.

Common applications include the automotive sector, such as parking assistance systems, blind spot detection, and collision prevention systems. They are also used in industrial automation for monitoring and controlling machine operations, as well as in consumer electronics, for example in smart home devices for gesture recognition and security monitoring. In recent years, bio-medical has become another important area of application of short-range radar systems [20,33]. Indeed they have the capability to remotely detect and monitor tiny vital signs, such as breathing and heart rate [17].

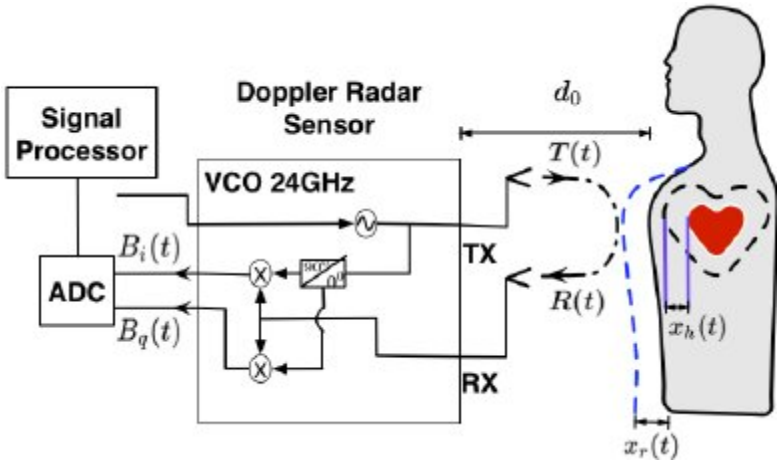

Figure 1.6 – Heartbeat and respiration detection using a radar sensor [34].

Radar systems are broadly categorized into continuous-wave (CW) radar [35,36] and impulse radar [37,38]. Impulse radars are utilized in various applications including vital sign detection, gesture recognition, and human tracking, with integrated chip solutions available for these systems. CW radars, with its simpler architecture, are ideal for mobile and portable applications due to their lower power consumption [31]. Various commercial CW radar chips and systems are available, especially for automotive applications.

Doppler and interferometry radar systems utilize a monochromatic waveform to acquire motion-related information, a process facilitated by the Doppler effect [29,39]. The signal

processing involved in Doppler radar systems, though relatively straightforward, enables them to achieve exceptional accuracy in measuring motion and displacement [40].

In contrast, frequency modulated continuous wave (FMCW) radars employ a modulated continuous wave to simultaneously ascertain both the range and doppler characteristics of targets. This makes FMCW radars particularly suitable for applications necessitating range information, such as localization, level monitoring, fall detection, monitoring of life activities, gesture recognition and automotive. Figure 1.7 shows a typical application of radar sensors in an automotive scenario.

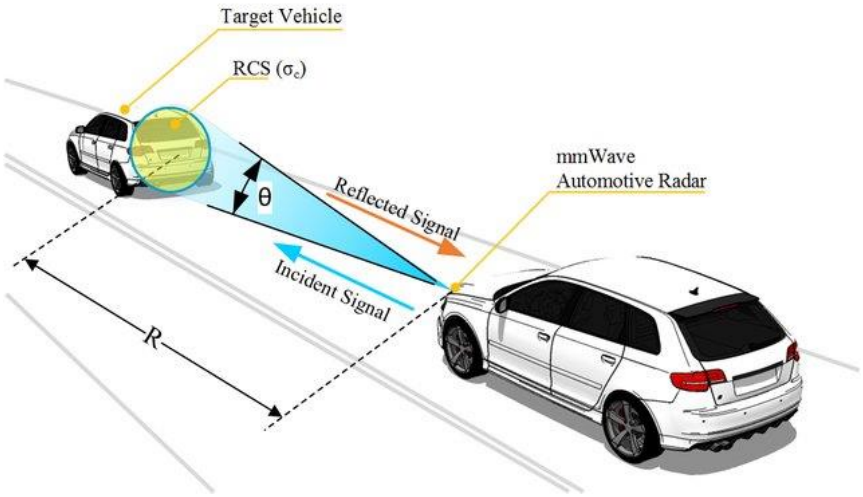

Figure 1.7 – Typical application of radar sensors in an automotive scenario [41].

The design and advancement of radar systems are inclusive of components such as the radar transceiver, the antenna or antenna array, and the processes involved in radar signal processing. Progressive enhancements in these domains are imperative for augmenting performance, diminishing size, and curtailing costs [17,42,43]. In pursuit of extending the capabilities of radar systems, techniques such as phased array, digital beamforming, and Multiple-Input Multiple-Output (MIMO) methods are increasingly employed. Furthermore, contemporary approaches in radar signal processing are progressively incorporating machine learning and artificial neural networks to bolster the intelligence of these systems [44].

1.3 Proximate noncontact sensing

Proximate noncontact sensing represents another scenarios in the noncontact sensing through wireless coupling, characterized by the employment of near-field interactions, where electromagnetic waves are utilized for communication and power transfer over relatively short distances and in particular where a sensing element, coupled with the target of interest, is wireless energized and interrogated. This approach leverages the principles of near-field communication (NFC), distinguishing it from far-field noncontact methods which operate over extended ranges and often necessitate substantial power. Proximate noncontact sensing are characterized by their ability to facilitate interactions within a limited range, typically not exceeding a few meters. The key advantages of this method include enhanced power efficiency, minimized signal interference, and augmented security measures.

The features of proximate noncontact sensing make it particularly apt for a spectrum of applications such as healthcare monitoring, localized environmental sensing, smart device interactive functionalities, and also industrial automation [45–47]. In healthcare, for instance, this technology facilitates the monitoring of vital signs or the functioning of implanted medical devices, offering a seamless integration into the daily lives of patients [45,48]. In industrial settings, it enables the monitoring of machinery and environmental conditions without the need of extensive wiring [49]. In consumer electronics, it enhances the user experience through seamless connectivity and interaction between devices.

As shown in Figure 1.8 the architecture of proximate noncontact sensing systems typically involves two primary components: a sensor unit and an interrogation unit [50]. The sensor unit is placed in direct contact or in close proximity to the target of measurement. This could range from environmental parameters to biometric data [45]. The interrogation unit, on the other hand, communicates with the sensor, often energizing it and retrieving the necessary data [51].

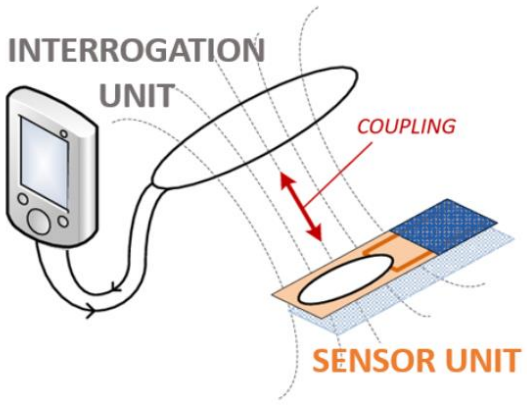

Figure 1.8 – Typical architecture of proximate noncontact sensing systems.

Sensor units can be categorized into two distinct types based on their operational mechanisms and component composition. The first type encompasses sensor units that integrate active electronics. These units are designed with the capability to store energy, which is crucial for powering an internal active circuit. This circuit is necessary for the operational functionality of the sensor and for the transmission of information [52].

Within this sphere of proximate noncontact sensing, near-field communication (NFC) sensors represent a significant and growing segment [52]. NFC technology, widely recognized for its use in secure payment systems and data exchange in smartphones, exemplifies a practical and user-friendly application of proximate noncontact sensing exploiting inductive coupling.

The second type of sensor units is instead characterized by the absence of active electronics. These units are composed exclusively of passive components serving both as the sensitive elements, responding to environmental stimuli or changes and for information exchange [53].

In this context, passive resonant contactless interrogated sensors represents a growing area of interest. These sensors are gaining traction due to their ability to operate without active electronics and open up possibilities for creating low-cost, disposable, and implantable devices [45].

In medical applications, for example, passive resonant sensors are being explored for use in biodegradable implants, offering a sustainable solution to health monitoring. In industrial applications, the lack of active electronic components facilitates deployment in environments characterized by harsh conditions and elevated temperatures [49].

1.3.1 Near-field communication sensors

Near-field communication (NFC) sensors stand at the forefront of proximate noncontact sensing technologies. Originally developed as a high-security, short-range wireless data exchange technology, NFC has evolved to offer unique capabilities for the design of miniature, battery-free sensing systems [46]. These sensors are especially useful in health care and food quality monitoring. Figure 1.9 shows an example of NFC based wireless device [54].

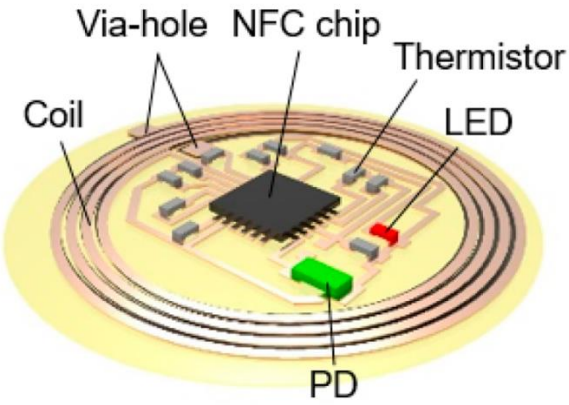

Figure 1.9 - Near-field communication (NFC) based wireless device [54].

NFC operates on a simple but effective principle. It involves two coils of conductors placed in close proximity, typically less than 5 cm apart, which can wirelessly exchange power and data through inductive coupling. The technology generally operates at a frequency of 13.56 MHz [46]. Data transfer is achieved through modulation techniques like amplitude or phase shift keying [54].

The appeal of NFC sensors lies in their ability to transfer sufficient power to activate low-power electronics, such as microcontrollers and sensors, without the need for batteries. This

feature, combined with the potential for high-volume, low-cost production on substrates like polyethylene terephthalate (PET) or paper, makes NFC sensors highly economical and scalable for widespread applications. The integration of NFC in smart devices and cards like electronic passports further demonstrates its versatility [54].

NFC-based sensing technologies are increasingly gaining traction, especially in healthcare and food quality monitoring. Wearable sensors on thin flexible substrates, as shown in Figure 1.10, provide non-invasive biophysical measurements using, for example, smartphones as readers. These sensors, while promising, face challenges in durability, noise levels, and manufacturing costs. Additionally, NFC-based electrochemical sensors offer viable alternatives for point-of-care diagnostics, and implantable NFC sensors address issues related to battery use in medical devices [52,55,56].

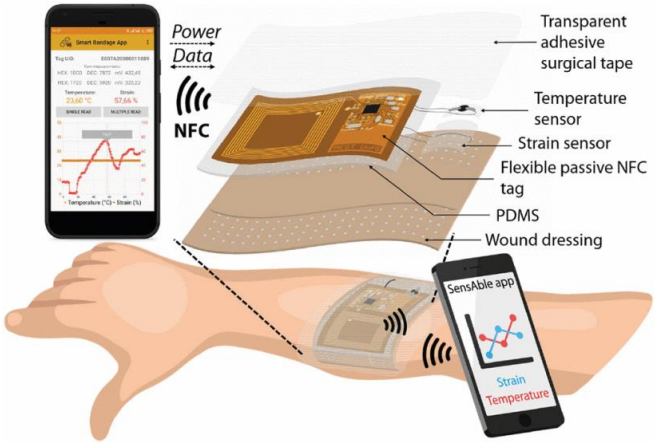

Figure 1.10 – NFC-based smart bandage for wireless strain and temperature real-time monitoring [57].

Commercially, NFC-based sensors are finding their place in health monitoring, with devices such as intraocular pressure sensors and glucose monitoring systems. In the food industry, they are being piloted for applications like tamper-proofing and ensuring food safety [45]. Increasing exploration of NFC sensors in academic research, particularly in wearable health sensors and disposable formats, underscores its potential in advancing proximate noncontact sensing [52].

1.3.2 Passive resonant contactless interrogated sensors

Passive resonant contactless interrogated sensors constitute an integral part of proximate noncontact sensing, characterized by their operation without active electronics and power sources. These sensors typically employ resonant circuits, which react to changes in external stimuli by altering their resonance properties.

Dating back to the 1960s, the development of passive resonant sensors has seen significant advancements, particularly with the integration of microelectromechanical systems (MEMS) technology in the 1990s [53,58]. These sensors were first proposed by Collins in 1967 with the invention of a miniature pressure sensor for intraocular pressure monitoring [59]. The remote query capability of these sensors is a standout feature, enabling the gathering of sensor data without the need for physical connections or precise alignment. This makes them particularly advantageous in scenarios where wired connections are impractical or impossible, such as in dynamic or rotating parts, medical implants inside the human body, and environments exposed to extreme conditions [46].

One of the primary benefits of passive resonant sensors is their operation without an external power source, making them ideal in applications where size and longevity are critical. This battery-free operation is not only cost-effective but also ensures a smaller sensor footprint and an extended operational lifespan. Another relevant benefit of this kind of contactless interrogated sensors is the absence of any active electronics, allowing to employ this sensors in harsh, high-temperature environments [47]. The simplicity of their structure, often based on LC (inductor-capacitor) resonant circuits as shown in Figure 1.11, further contributes to their cost-effectiveness. These circuits react to changes in external stimuli, such as temperature, pressure, or chemical composition, by altering their resonance properties, often contactless detected through a shift in resonant frequency [47,58,60].

The efficacy of passive resonant sensors in noncontact sensing has been verified across various sensor types, including quartz crystal resonators (QCR) [51], quartz crystal microbalances (QCM) [61], resonant piezolayer (RPL) sensors [62], MEMS resonators [63,64], and LC resonant sensors [47,58,65].

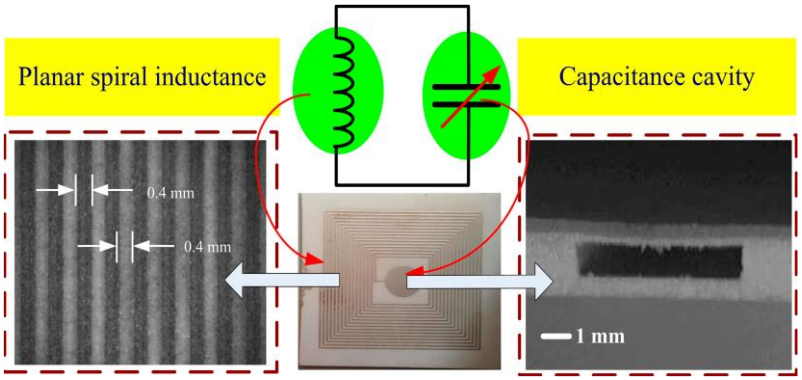

Figure 1.11 – Example of noncontact interrogable LC resonant ceramic pressure sensor [47].

The versatility of these sensors is further highlighted by their compatibility with both frequency-domain and time-domain interrogation techniques [51]. In the frequency-domain approach, parameters such as impedance, reflection coefficients, or specific transfer functions are measured by concurrently exciting and sensing the resonator [49,66,67]. On the other hand, time-domain techniques, capitalize on the transient free response of the resonator. This is achieved by distinctly separating the phases of excitation and detection [68].

Thanks to the absence of active electronics and consequently the possibility to realize this sensor with printed electronics, a promising area of development is the integration of biocompatible materials in implantable devices [48]. As healthcare technology advances, there is a growing focus on creating sensors that not only perform reliably when in contact with biological tissues but also degrade safely within the body, eliminating the need for surgical removal. The use of biodegradable polymers and conductive materials is being explored to achieve these goals, as shown in Figure 1.12.

In addition to medical and harsh environments applications, passive resonant sensors are being adapted for wearable devices, leveraging flexible substrates for a broader range of applications. This adaptability opens up possibilities in wellness monitoring and environmental sensing, offering convenient and non-invasive solutions for health and safety monitoring.

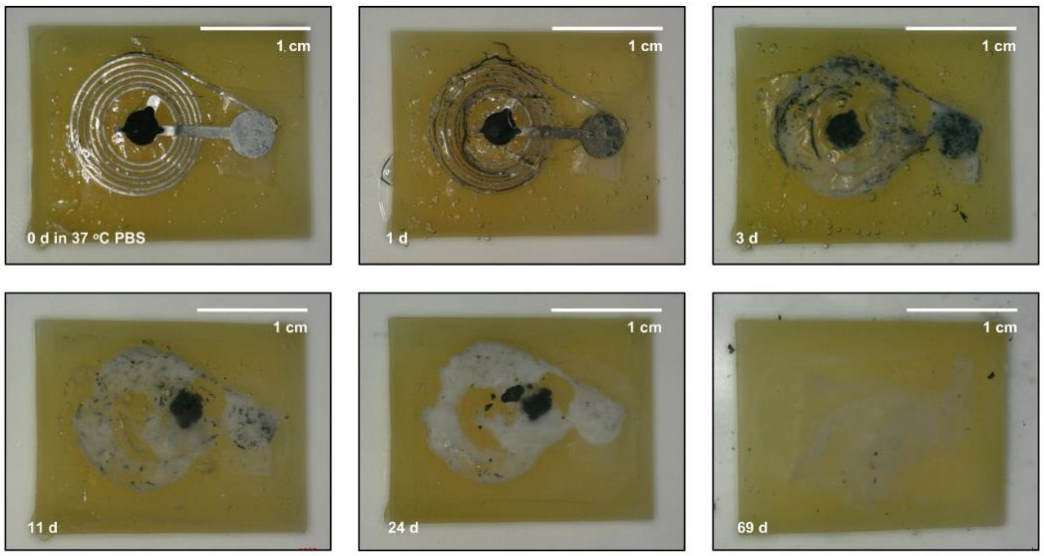

Figure 1.12 – Example of bioresorbable, contactless interrogated, passive sensor [48].

Furthermore, these sensors hold significant potential in intelligent packaging, especially in the food industry, promising advancements in food safety and quality monitoring [45,46,69].

Recent developments in the field of passive resonant contactless interrogated sensors have focused on overcoming challenges such as limited interrogation distances due to geometrical constraints and the influence of the interrogation distance in the measurement [51]. Efforts are being made to enhance the coupling between the readout coil and the inductor, improve sensor sensitivity and quality factor, incorporate resonant repeaters to extend the sensor operational range and implement fully integrated and low-cost compact system [68,70].

1.4 Motivations and aims of the research activity

The research presented in this thesis is fundamentally driven by the goal of advancing noncontact sensing technologies, both for distant and proximate sensing, aiming to enhance their flexibility, extend the range of their monitoring applications, and unlock novel opportunities for practical implementation in many scenarios, ranging from industrial monitoring to healthcare applications. This involves delving into the development of noncontact sensing technologies that are more adaptable, reliable, and capable of operating under diverse and challenging conditions by exploiting advancement in sensors technology, such as fully integrated or printable electronics.

Another key aspect of this research is the ease of installation of these sensors also into existing systems. The goal is to design sensors that can be seamlessly integrated into current technological infrastructures, minimizing the need for extensive modifications. This aspect is crucial in ensuring that the benefits of noncontact sensing technologies can be readily accessed and utilized by a broader range of users.

In summary, this research aims to contribute significantly to the evolution of noncontact sensing through wireless coupling technologies, ensuring they are not only advanced and versatile but also cost-effective and easily integrable, to pave the way for future innovations in noncontact sensing, making it an accessible and indispensable tool in diverse technological domains.

1.5 Thesis organization and contents

The manuscript is organized into eight chapters, as briefly summarized in the following:

Chapter 1: Introduction

An overview on noncontact sensing systems is reported in this chapter, focusing on two different scenarios: distant noncontact sensing and proximate noncontact sensing related in particular to electromagnetic far field and near field, respectively. The main technology utilized in these scenarios are reported to give an introduction of the topics reported in the successive chapters.

Chapter 2: Radar sensor system for unobtrusive level monitoring of granular solids stored in silos

In the field of distant sensing, the possibility of measuring from the outside of a fiber-glass silo the level of stored granular solids, such as grains, flour, sand, or feed, by employing an unobtrusive millimeter wave radar sensor system without the need for a specific hatch has been explored in this chapter. A prototype embedding a frequency-modulated continuous-wave (FMCW) radar sensor system operating at 76-81 GHz, combined with a dedicated electronic board has been developed to acquire and manage data through Wi-Fi connection. The obtained experimental results show the effectiveness of the proposed radar sensor system in estimating the level of the material stored into the silo, without the need for a dedicated opening in the silo.

Chapter 3: Proximate noncontact interrogation techniques

This chapter gives a theoretical background in the noncontact interrogation of resonant passive sensors within the near field, focusing on techniques for the interrogation of resonant sensor units which are inductively coupled to an interrogation unit. These techniques utilize the resonant frequency and quality factor as key readout signals. Various types of sensor units, based on capacitive, inductive, and electromechanical piezoelectric resonator sensor units are analyzed. Furthermore, two interrogation techniques present in

literature, one based on the frequency-domain and the other on the time-domain, are explained.

Chapter 4: Noncontact interrogation of piezoelectric MEMS resonators for temperature measurement

The development and experimental characterization of an electronic technique and system for noncontact reading of the temperature-dependent resonant frequency of a piezoelectric MEMS resonators is presented in this chapter. The proposed approach integrates the noncontact interrogation method presented in Chapter 3, applied to a piezoelectric MEMS (Micro-Electro-Mechanical System) resonator, with a post-processing technique based on autocorrelation analysis. This innovative method has been applied to temperature sensing by exploiting the temperature-dependent characteristics of an aluminum nitride (AlN) thin-film piezoelectric on silicon (TPoS) resonator operating in the radial contour-mode configuration. The experimental results obtained using the proposed technique are independent from the interrogation distance.

Chapter 5: Noncontact interrogation of a flexible passive sensor patch with capacitive sensing element for human body temperature

A novel approach for human skin temperature measurement based on a passive flexible patch combining contact sensing with contactless interrogation is presented in this chapter. Specifically, the proposed approach extends the contactless interrogation technique described in Chapter 3 to a flexible sensor patch attached onto a curved surface and achieves contactless interrogation independently of the bending of the flexible patch. The sensor patch is based on a RLC resonant circuit, featuring an inductive copper coil for magnetic coupling, a ceramic capacitor serving as the temperature sensing element, and an additional series inductor added to mitigate the dependency of the resonant frequency on the bending of the patch. The sensor has been interrogated using a time-gated technique involving an external readout coil electromagnetically coupled to the patch coil. A proof-of-concept prototype, developed by employing a paper-based flexible patch and off-the-shelf components, has been experimentally tested.

Chapter 6: Noncontact interrogation of inductive sensors for conductive target detection

This chapter introduces a novel method for the contactless interrogation of an inductive sensor used for detecting conductive targets. The system features a solenoidal coil connected with a capacitor to form a resonating LC circuit, whose frequency changes when a conductive target is introduced in the generated magnetic field. An external interrogation coil electromagnetically coupled to the inductive sensor enables the measurement of resonant frequency changes without direct contact. Experimental results demonstrate the sensor effectiveness in detecting conductive targets, highlighting its potential for applications in environments where traditional cabled sensing methods are impractical.

Chapter 7: Noncontact interrogation of passive resistive sensors

A novel contactless interrogation technique for passive resistive sensors is presented in this chapter. By exploiting quartz crystal resonator (QCR) as resonant device it has been possible to overcome limitations related to amplitude measurements techniques. Indeed, this method effectively utilizes the stable resonant frequency and high-quality factor of QCRs to achieve accurate sensor resistance measurements, independent from the interrogation distance. Experimental validation confirms the method robustness and precision, with a notable sensor resolution.

Chapter 8: Conclusions

The thesis contents, purposes and obtained results are summarized in this chapter.

.

Chapter 2

Radar sensor system for unobtrusive level monitoring of granular solids stored in silos

In the field of distant sensing, the possibility of measuring from the outside of a fiber-glass silo the level of stored granular solids, such as grains, flour, sand, or feed, by employing an unobtrusive millimeter-wave radar sensor system without the need for a specific hatch has been explored in this chapter. A prototype embedding a frequency-modulated continuous-wave (FMCW) radar sensor system operating at 76-81 GHz, combined with a dedicated electronic board has been developed to acquire and manage data through Wi-Fi connection. The prototype has been installed on the outside of a fiberglass silo containing granular and dusty material with a density of about 800 kg/m³ while employing four load cells as reference measurement system. The proposed prototype has been tested over repeated cycles of load and unload of the silo, during which the level of the stored granular solids has varied between 0.5 and 5.2 m. The measurement repeatability, which defines the equivalent resolution of the sensor system, has been estimated at one standard deviation resulting in 0.037 m. The obtained experimental results show the effectiveness of the proposed radar sensor system in estimating the level of the material stored into the silo, without the need for an opening in the silo.

2.1 Level monitoring of granular solids stored in silos

Level monitoring of granular solids stored in silos, such as grains, flour, sand, or feed is often required in industrial and agricultural applications [71]. Typically, mechanical sensors, such as load cells, are employed for these purposes. Even though these types of sensors are relatively cheap, tailored container designs and demanding installation procedures are typically needed. Furthermore, the density of the material stored in the silo must be known to define the filling level [71]. Alternatively, optical sensors can be used, but with the drawback of being ineffective in dusty environments or with poorly-reflective materials [72]. Similarly, ultrasound sensors can be used, yet they are unavailing with sound-absorbing materials and are affected by the speed of sound, which depends largely on the propagation medium composition and, on the environmental pressure and temperature [73].

Frequency-modulated continuous-wave (FMCW) millimeter-wave radar sensor systems have proven to be a viable alternative to overcome such issues [74,75]. Compact systems are nowadays available thanks to the recent progresses in the fabrication of fully-integrated radar microchips, promoted by the intensive use in the automotive field that has made available this technology at low cost [42,43].

In this context, the possibility of measuring unobtrusively the level of granular material stored inside a fiberglass silo by means of a millimeter-wave radar sensor system has been explored. A prototype embedding a FMCW radar sensor system operating at 76-81 GHz, and an electronic board to acquire the data and manage a remote communication through Wi-Fi connection has been developed and experimentally verified.

2.2 Frequency modulated continuous wave radar

A FMCW radar system continuously transmits frequency-modulated electromagnetic waves, named chirp, and detects signal reflections due to the presence of one or more objects in its field of view (FOV).

Typically, a FMCW radar is composed of a synthesizer that generates a chirp signal represented by $x_{TX} = \sin(2\pi f_{TX}+\Phi_{TX})$, where f_{TX} and Φ_{TX} are respectively the frequency and phase of the generated and transmitted signal. It also consists of transmitting (TX) and receiving (RX) antennas, and a mixer. The mixer processes the received signal $x_{RX} = \sin(2\pi f_{RX}+\Phi_{RX})$, where f_{RX} and Φ_{RX} are respectively the frequency and phase of the received signal, with the transmitted one x_{TX} generating the intermediate signal x_{IF}, as shown in Figure 2.1.

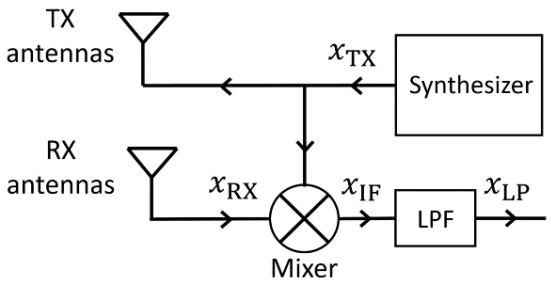

Figure 2.1 – FMCW radar block diagram.

The signal x_{IF} is low-pass filtered to reject high-frequency spectral components, thus leading to x_{LP}, which presents the following expression where the component given by the sum of the frequency of the signals x_{TX} and x_{RX} is filtered:

$$x_{LP} = \frac{1}{2}\cos[2\pi(f_{TX} - f_{RX})t + (\Phi_{TX} - \Phi_{RX})] \tag{2.1}$$

Figure 2.2 shows the typical trend over time of the frequencies f_{TX} and f_{RX} of x_{TX} and x_{RX}, respectively. Specifically, f_{TX} is assumed to vary linearly from the starting frequency f_c and span the bandwidth B during the chirp time T_c.

Considering a single object placed within the FOV at a fixed distance d from the radar, which causes the reflection of the transmitted signal, f_{RX} is expected to have the same trend of frequency variation over time as f_{TX} but delayed by a time $\tau = 2d/c$, where c is the speed of light.

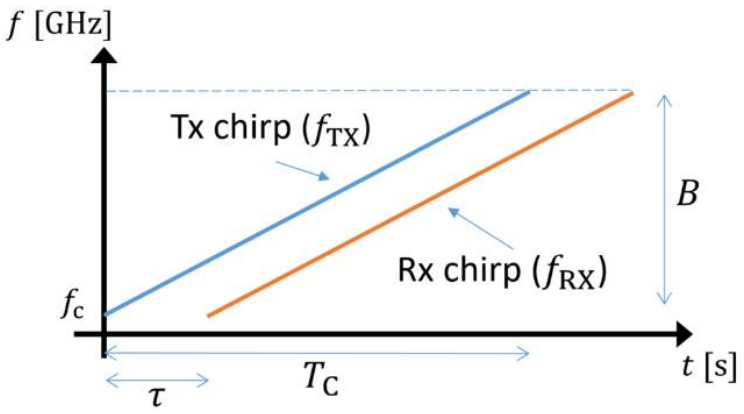

Figure 2.2 – Frequency of the transmitted and received signals over time.

Figure 2.3 shows how the presence of one or more objects in the FOV induces peaks in the normalized reflected power P_r of x_{LP}, thus allowing to estimate the distances between the objects and the radar.

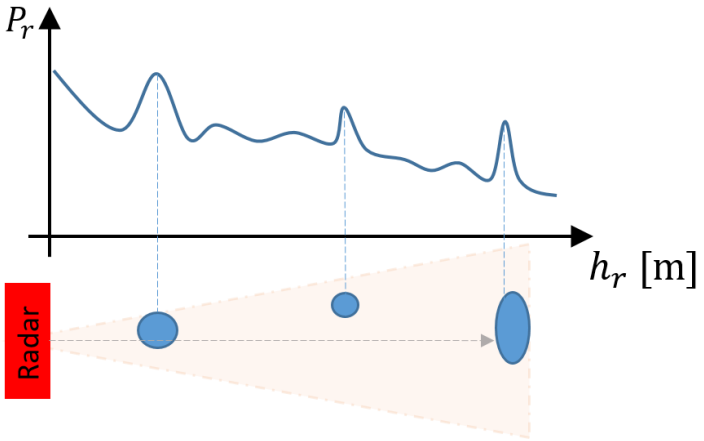

Figure 2.3 – Normalized reflected power P_r as a function of d showing peaks corresponding to three objects concurrently within the FOV of the antennas.

2.3 Proposed system description

Figure 2.4 shows the block diagram of the developed prototype. The radar sensor is based on the Texas Instruments IWR1443BOOST development board featuring a 76-81 GHz FMCW radar sensor fabricated in TI's 45-nm RFCMOS process, as shown in Figure 2.5.

Figure 2.4 – Block diagram of the developed radar system.

The chip is equipped with built-in electronics that also comprises hardware supporting front-end configuration, calibration, and complex operations. The board is equipped with an antenna array composed of 3 transmitting (Tx) and 4 receiving (Rx) antennas with a maximum transmission power of 12 dBm, allowing for a theoretical detection range of up to 50 m. A Raspberry PI board interfaces the radar sensor, acquires data and manages the remote communication through a Wi-Fi connection.

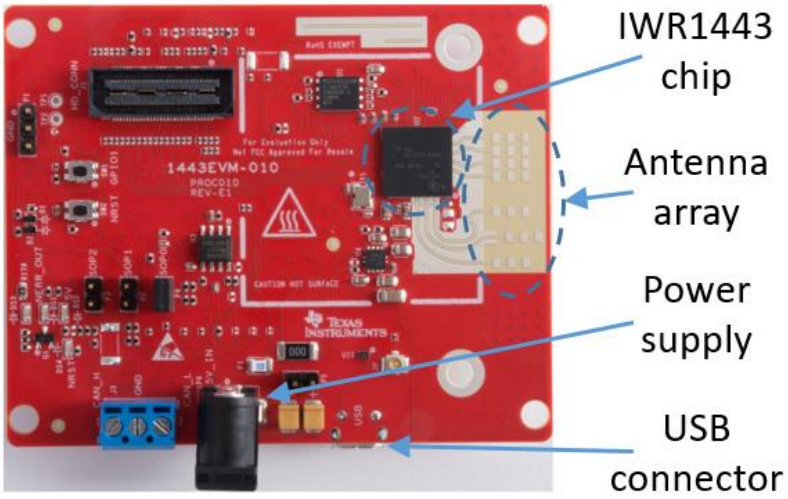

Figure 2.5 – Picture of the Texas Instruments IWR1443BOOST board.

The prototype has been installed on the top and outside of a fiberglass silo containing sound-absorbing, granular and dusty material with a density ρ of about 800 kg/m³, as shown in Figure 2.6.

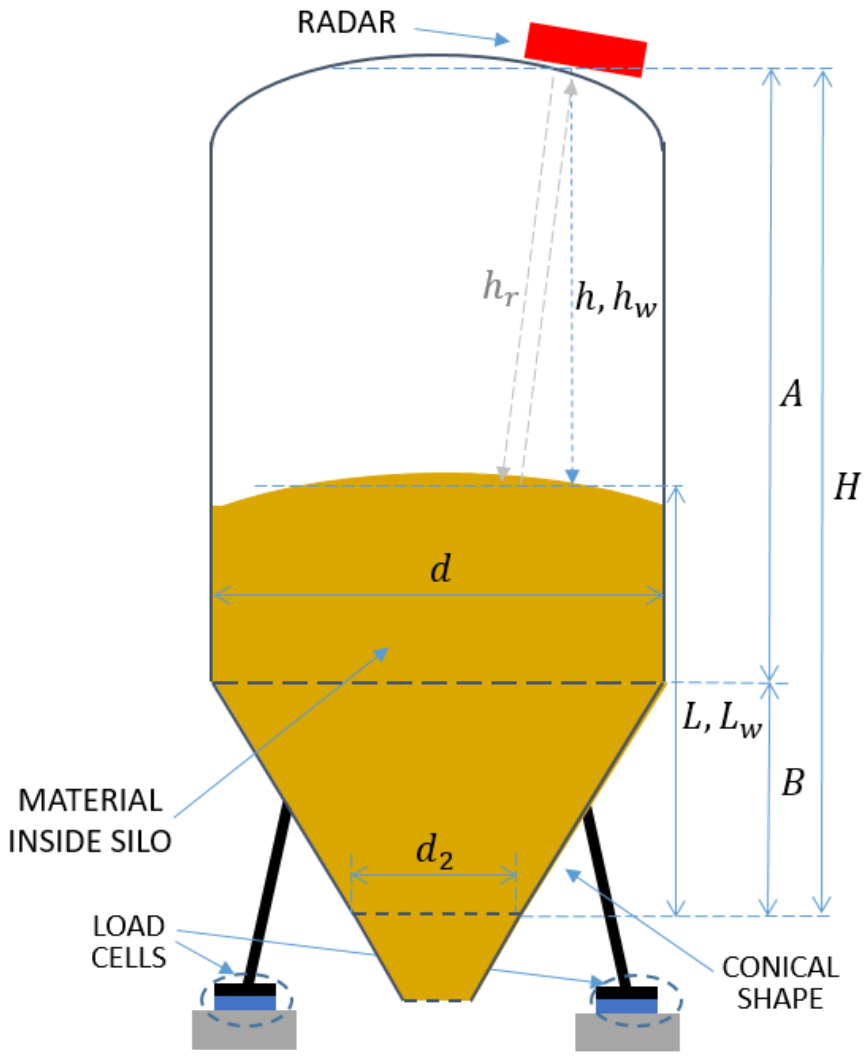

Figure 2.6 – Schematic diagram of the silo structure and radar positioning.

The silo has a total height *H* of 6.1 m with a cylindrical section with height *A* of 4.2 m at the top with diameter *d* of 2.48 m, and a truncated cone with height *B* of 1.7 m at the bottom with a lower diameter d_2 of 0.8 m. The radar sensor has been mounted tilted to accommodate for the curved cover of the silo as shown in Figure 2.7. Given the silo dimensions, the radar board has been set with a detection range of 10 m and configured

with one transmitting and two receiving antennas. The silo embeds four load cells under the feet anchors that allow for real-time measurements of the weight of the stored granular material.

Figure 2.7 – Image of the prototype installed outside the circular fiberglass silo.

Considering the weight w, the geometry of the silo, and the mass density ρ of the material, the level L_w of material stored in the silo has been estimated and used as the reference value. The volume v_w of the material inside the silo is determined as $v_w = w/\rho$. From v_w and taking in account separately of the cylindrical and conical section of the silo, it is possible to determine the reference height h_w with the following equation:

$$h_w = \begin{cases} A + B - \dfrac{B \cdot v}{V_B}, & v < V_B \\ A - \left\{ \dfrac{v - V_B}{\pi \cdot \dfrac{d^2}{4}} \right\}, & v \geq V_B \end{cases} \tag{2.2}$$

where V_B is the volume of the truncated cone section:

$$V_B = \frac{\pi \cdot B \left(\dfrac{d^2}{4} + \dfrac{d_2^2}{4} + \dfrac{d \cdot d_2}{4} \right)}{3}. \tag{2.3}$$

The level of material inside the silo estimated form the load cell measurements is consequently determined as $L_w = H - h_w$

From the radar measurement, the level of the material L inside the silo is similarly determined as $L = H - h$, with the assumption of $h \approx h_r$, as the tilt of the radar has been considered negligible. Moreover, since granular solids tend to build up a heap with non-planar surface, h_r has to be considered as an average value [71]. The distance h_r is determined from the reflected power P_r normalized to its maximum amplitude, as shown in Figure 2.8.

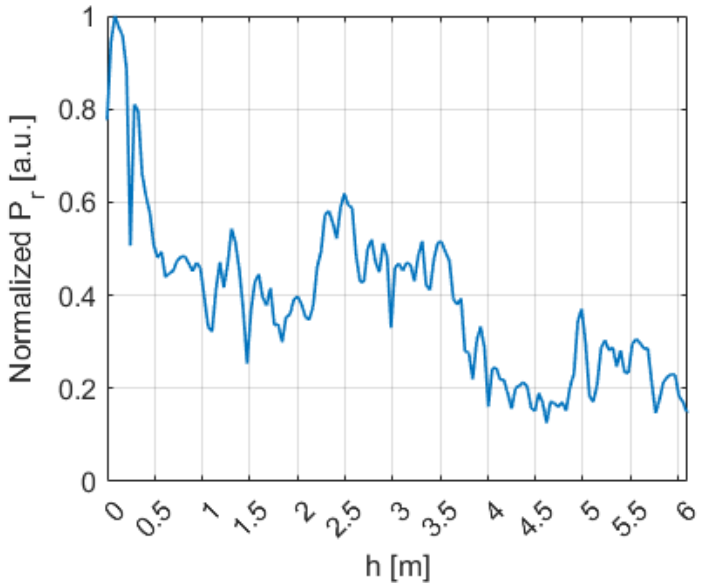

Figure 2.8 – Measured normalized reflected power P_r as a function of h.

Each peak of P_r corresponds to an object within the FOV of the antenna array. Excluding peaks located at $h < 0.5$ m, corresponding to the reflections between the radar and the top cover of the silo, no distinct peaks are evident in the reflected power.

Therefore, to improve the signal-to-noise ratio and to estimate the average distance h, an algorithm based on consecutive acquisitions of P_r and linear filtering techniques has been devised [76].

2.4 Experimental results

A measurement campaign of 15 consecutive days during which the silo has been loaded and progressively unloaded has been performed. Figure 2.9 compares the experimental values of L and L_w measured every minute, when the level has been varied between 0.5 and 5.2 m.

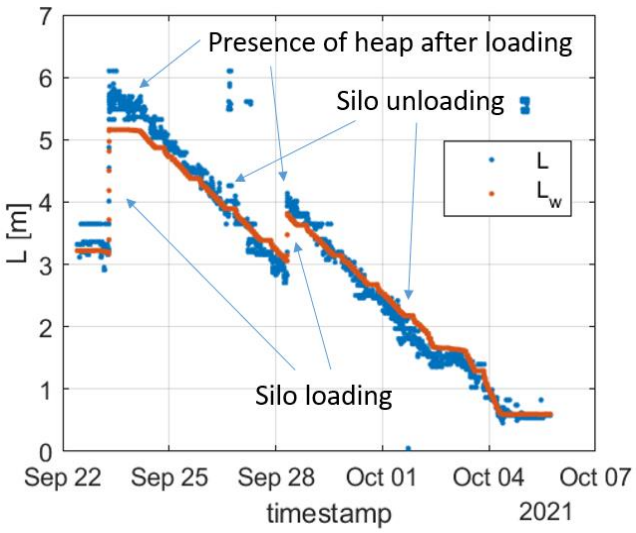

Figure 2.9 – Estimated and reference levels L and L_w obtained employing the radar and load cells systems, respectively, for a measurement campaign of 15 days, measured every minute.

The discrepancy between L and L_w after the first silo loading is probably related to the formation of heap due to the loading process of the silo from the top. This discrepancy is also present after the second loading even if less accentuated, probably due to a lower amount of loaded material. Minor deviations between L and L_w can be observed for $L < 2$ m that correspond to the beginning of the conical part of the silo. Such deviations can be attributed to inaccuracies in the estimation of the material level from the load cells system.

As shown in Figure 2.10, the best fit line of L against L_w has a slope of 1.06, i.e. close to the ideal line, showing the effectiveness of the radar sensor system to estimate from the outside the level of the material stored into the silo, within the explored range. The discrepancy that can be observed for L around 5 m has been ascribed to the formation of a heap in the loading process.

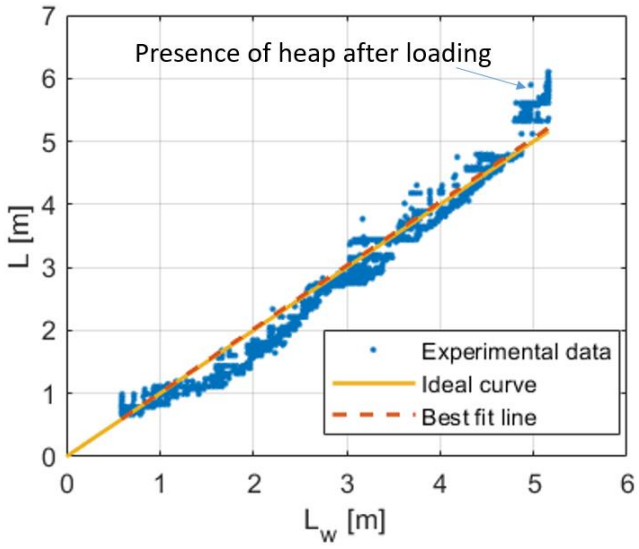

Figure 2.10 – Comparison between the radar estimated level *L* and reference level L_w.

The measurement repeatability, which defines the equivalent resolution of the sensor system, has been estimated at one standard deviation over 100 repeated measurements at the fixed level L_w = 3.63 m, resulting in 0.037 m.

Chapter 3

Proximate noncontact interrogation techniques

In the field of proximate sensing, this thesis investigates into the area of noncontact interrogation of passive sensors. This chapter, in particular, lays out the foundational concepts for the noncontact interrogation of resonant passive sensors within the near field, a process that hinges on the principles of inductive coupling. The focus is particularly on techniques for the interrogation of sensor units that operate based on resonance, which are inductively coupled to an interrogation unit. These techniques utilize the resonant frequency and quality factor as key readout signals. Various types of sensor units, based on capacitive, inductive, and electromechanical piezoelectric resonator sensor units are analyzed. Furthermore, two interrogation techniques present in literature, one based on the frequency-domain and the other on the time-domain, are explained. These methodologies are theoretically independent to the coupling factor, a critical feature that aims to ensure that sensor readings remain accurate and consistent regardless of the distance of interrogation. However, due to practical limitations, it is shown that unavoidable parasitic capacitance introduces distance-dependent variables. This factor adds an undesired layer of complexity, as it influences the accuracy of sensor readings based on the distance of interrogation for both the frequency-domain and time-domain techniques. Mitigating techniques, derived from literature, are presented to inhibit such effects and to enhance the reliability and accuracy of this noncontact sensing techniques.

3.1 Near-field interrogation of passive resonant sensors

3.1.1 Passive resonant sensors

In physics, resonance is the tendency of a system to oscillate with greater amplitude at some frequencies, called resonant frequencies, than at others. Resonance occurs when a system is able to store and easily transfer energy between two or more different storage modes, e.g. kinetic energy and potential energy for example in the case of a pendulum, or electric and magnetic energy in the case of an inductance-capacitance circuit. From cycle to cycle, there are some losses, called damping. The resonant frequency of a specific object is related to its parameters. Any change in one of these parameters can reflect in a change of the resonant frequency [77].

Passive resonant sensors are a class of sensing devices that leverage resonant frequency characteristics to detect and respond to various physical and environmental parameters. These sensors operate without an integrated power source and instead rely on external excitation, making them suitable for a wide range of applications.

Resonant sensors are utilized in a wide range of applications: environmental monitoring, structural health monitoring, food packaging, healthcare, IoT, and industrial monitoring. These sensors operate on various principles, including changes in mass, electrical field, mechanical stress, and temperature [77].

Passive sensors, in contrast to their active counterparts, do not require a dedicated power supply for their operation. Instead, they rely on the modulation of the exciting signal. Resonant sensors utilize this fundamental concept, where their electrical properties, generally resonant frequency, change in response to the physical or chemical quantity they are designed to monitor.

These sensors are characterized by a resonant frequency, which is the frequency at which they exhibit maximum sensitivity to external stimuli. The alteration of resonance parameters due to changes in the sensed parameter, such as temperature, humidity, pressure, force, or specific analytes, serves as the basis for their sensing mechanism. By

measuring the shift in resonance parameters, the environmental changes can be quantified and obtaining valuable information. To excite and detect oscillation of resonant sensors, several methods are employed which can exploit piezoelectric, electrostatic, optical, and electromagnetic principles [78,79].

In principle, the measured resonant frequency does not depend on the specific interrogation method adopted, making resonant sensing a robust approach for contactless operation [78–81]. Indeed, one of the significant advancements in passive resonant sensors is their integration with contactless interrogation techniques based on electromagnetic coupling. This noncontact interrogation method eliminates the need for physical connections, making it particularly useful in situations where sensor placement is challenging, for example in enclosed environments.

The continuous development of these sensors and their contactless interrogation methods holds the promise of further innovations, driving the advancement of scientific research and technological applications in various domains.

3.1.2 Resonant principle

Harmonic oscillators are a fundamental concept in classical mechanics, representing systems that exhibit periodic motion when displaced from their equilibrium or balanced position. These systems are characterized by a restoring force *F* that acts to return the system to its equilibrium state. This force is directly proportional to the displacement from equilibrium, a relationship mathematically described by Hooke's Law:

$$F = -kx \tag{3.1}$$

where *k* represents a positive constant, indicative of the inherent resistance of the system to displacement.

In instances where *F* constitutes the sole force acting upon the system, we refer to it as a simple harmonic oscillator. This oscillator is characterized by simple harmonic motion, displaying sinusoidal oscillations around its equilibrium point. Remarkably, these oscillations

maintain a constant amplitude and frequency, the latter being independent of the harmonic motion amplitude. When the system is subject to a frictional (damping) force, proportional to velocity, it transforms into a damped oscillator.

With reference to Figure 3.1, the equation of motion for a linear harmonic oscillator, assuming no external force acts upon the system, can be mathematically formulated as:

$$m\frac{d^2x}{dt^2} + c\frac{dx}{dt} + kx = 0. \tag{3.2}$$

In this equation, *x* represents the displacement from equilibrium, *m* the mass of the system, *c* the damping coefficient, and *k* the spring constant or elastic coefficient. Equation (3.2) can be also rewritten into the form:

$$\frac{d^2x}{dt^2} + 2\zeta\omega_0\frac{dx}{dt} + \omega_0^2 x = 0, \tag{3.3}$$

where $\omega_0 = (k/m)^{½}$ is the undamped angular frequency of the oscillator, while $\zeta = c/2(mk)^{½}$ is the damping ratio.

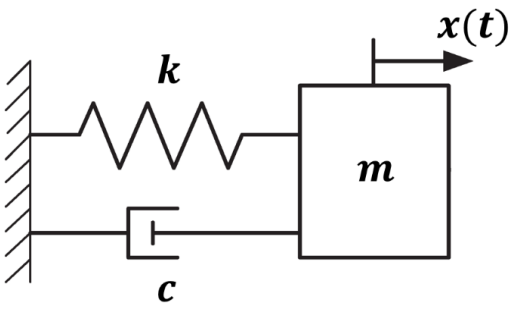

Figure 3.1 – Mass-spring-damper representation of a linear harmonic oscillator.

In the idealized scenario where damping is either absent or negligible (i.e., *c* = 0), an harmonic oscillator, once displaced from its equilibrium point and released, will continue to oscillate indefinitely with a constant amplitude and frequency. This perpetual motion persists in the absence of any external interference.

However, in practical applications, oscillators experience damping due to frictional forces, which reduces their motion over time. Unlike simple harmonic motion, which is influenced solely by the restoring force, damped harmonic motion also experiences frictional forces. These forces typically scale with the object velocity, leading to a gradual decrease in the amplitude of oscillation until the motion eventually ceases.

When damping is present (i.e., $c \neq 0$), the system behaves as a damped oscillator. The presence of damping causes the oscillator to have a lower frequency than in the undamped case, and the amplitude of vibration diminishes over time [82]. Numerous real-world examples of damped harmonic oscillators exist, ranging from mechanical systems like pendulums and mass-spring assemblies to electrical systems like RLC circuits.

Energy dissipation in a damped harmonic oscillator occurs during its oscillatory motion due to the presence of damping. The quality factor (Q) is defined as the ratio of the energy stored in the system to the energy it loses per oscillation cycle:

$$Q = 2\pi \frac{stored\ energy}{lost\ per\ cycle\ energy} = \frac{1}{2\zeta}. \tag{3.4}$$

Depending on ζ and thus on Q, a damped harmonic oscillator can be classified as overdamped ($\zeta > 1$, $Q < 1/2$), critically damped ($\zeta = 1$, $Q = 1/2$), or underdamped ($0 < \zeta < 1$, $Q > 1/2$).

In the underdamped case, the oscillator still exhibits oscillatory behaviour, albeit with a progressively decreasing amplitude, as shown in Figure 3.2. The decay time τ, during which the amplitude diminishes to $1/e$ of its original value, is defined as $\tau = 1/\zeta\omega_0$.

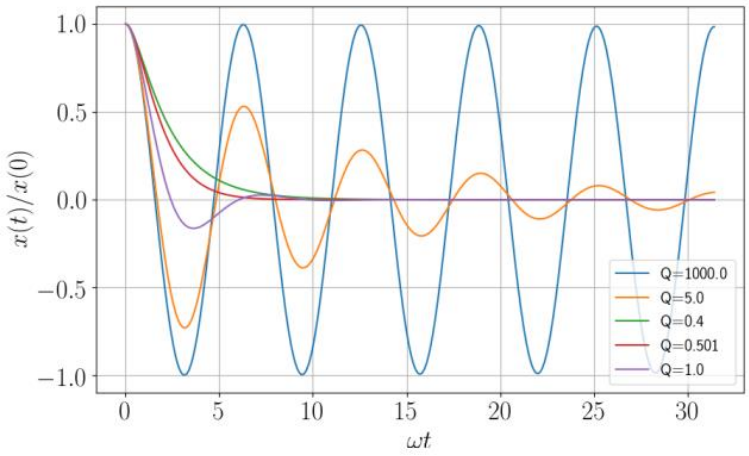

Figure 3.2 – Time domain response of a damped harmonic oscillation, varying the damping (i.e., the quality factor *Q*), keeping the resonant frequency $f_0 = \omega_0/2\pi$ and initial condition fixed) [83].

The angular frequency of the underdamped harmonic oscillator is given by:

$$\omega_d = \omega_0 \sqrt{1 - \frac{1}{4Q^2}}. \tag{3.5}$$

Consequently, the equation of motion of a damped harmonic oscillator can be written as:

$$x(t) = Xe^{-t/2Q} \cos(\omega_d t - \theta\,). \tag{3.6}$$

Considering now the case of driven harmonic oscillators, which consider damped oscillator further affected by an externally applied force *F*(*t*), the Newton second law take the form:

$$m\frac{d^2x}{dt^2} + c\frac{dx}{dt} + kx = F(t), \tag{3.7}$$

which can be rewritten into the same form of Equation (3.3):

$$\frac{d^2x}{dt^2} + 2\zeta\omega_0\frac{dx}{dt} + \omega_0^2 x = \frac{F(t)}{m}, \tag{3.8}$$

Considering now the specific case of a sinusoidal driving force $F(t) = \cos(\omega t)$, where ω is the driving frequency, the steady-state solution of Equation (3.8) results:

$$x(t) = A\cos(\omega t + \phi), \tag{3.9}$$

where the amplitude A is given by:

$$A = \frac{Q}{\omega\omega_0}\frac{1}{\sqrt{Q^2(\omega_0/\omega - \omega/\omega_0)^2 + 1}}, \tag{3.10}$$

while the phase is given by:

$$\phi = -\arctan\left(\frac{Q^{-1}}{\omega_0/\omega - \omega/\omega_0}\right). \tag{3.11}$$

It results that the phase varies from slightly negative for low frequencies, passing rapidly (for large Q) through $-\pi/2$ on resonance, and decreasing to $-\pi$ for large frequencies, as shown in Figure 3.3.

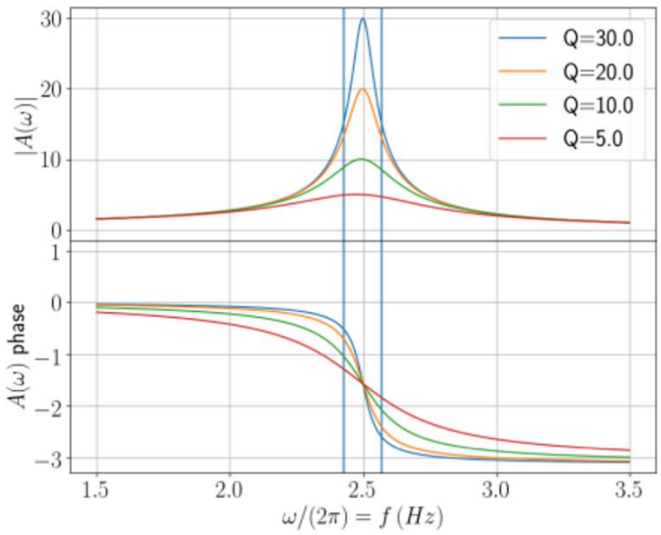

Figure 3.3 – Frequency response of a damped, driven harmonic oscillation, varying the damping (i.e. the quality factor Q), keeping the resonant frequency $f_0 = \omega_0/2\pi$ fixed at 2.5 Hz. The FWHM is shown only for the curve with the highest value of Q [83].

3.1.3 Near-field electromagnetic coupling and mutual inductance

Near-field electromagnetic coupling refers to the interaction between two closely spaced conductors, where the electromagnetic fields are not fully radiated into the surrounding space but are confined in the proximity of the conductors. This phenomenon is particularly relevant in applications involving short-range communication, wireless power transfer, and NFC systems. The near-field coupling strength is characterized by the spatial distribution of electric and magnetic fields. Maxwell equations play a crucial role in mathematically describing the near-field behaviour, considering factors such as distance between conductors, frequencies involved, and the geometric configuration of the system.

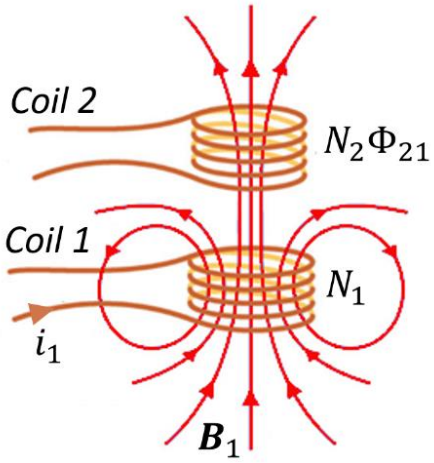

Figure 3.4 – Interaction between two coil placed near each other: changing current in coil 1 produces changing magnetic flux in coil 2.

Considering two coils placed in close proximity each other as shown in Figure 3.4, characterized by N_1 and N_2 turns respectively, the current i_1 flowing in the first coil generate a magnetic field $\boldsymbol{B}_1$ which pass through the second coil. By varying i_1 with time, there will be an induced electromotive force e associated with the changing magnetic flux in the second coil:

$$e_{21} = -N_2 \frac{d\Phi_{21}}{dt} = -\frac{d}{dt}\iint_{S_2} \boldsymbol{B}_1 d\boldsymbol{A}_2 \tag{3.12}$$

where Φ_{21} is the magnetic flux through the second coil caused by the current i_1, S_2 is the surface area enclosed by the second coil and $d\boldsymbol{A}_2$ is an infinitesimal area element on S_2.

The rate of change of magnetic flux Φ_{21} in the second coil is directly proportional to the rate of change of current i_1

$$N_2 \frac{d\Phi_{21}}{dt} = M_{21} \frac{di_1}{dt} \tag{3.13}$$

where M_{21} represents the mutual inductance which only depends on the geometrical properties of the two coils such as the number of turns and the radii of the two coils.

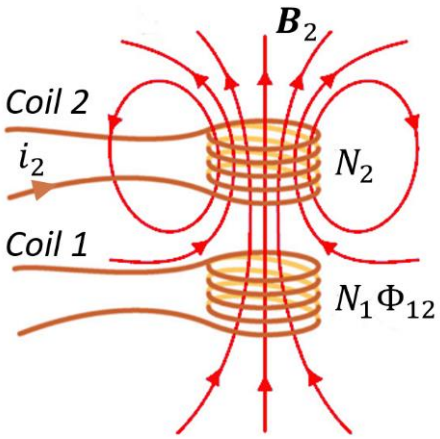

Figure 3.5 – Interaction between two coil placed near each other: changing current in coil 2 produces changing magnetic flux in coil 1.

Similarly, considering a current i_2 flowing in the second coil, as shown in Figure 3.5 the corresponding electromotive force induced in the first coil results:

$$e_{12} = -N_1 \frac{d\Phi_{12}}{dt} = -\frac{d}{dt} \iint_{S_1} \boldsymbol{B}_2 d\boldsymbol{A}_1. \tag{3.14}$$

Where Φ_{12} is the magnetic flux through the first coil caused by the current i_2, S_1 is the surface area enclosed by the first coil and $d\boldsymbol{A}_1$ is an infinitesimal area element on S_1.

The changing flux in the first coil is also in this case proportional to the changing current i_2 in the second coil:

$$N_1 \frac{d\Phi_{12}}{dt} = M_{12} \frac{di_2}{dt} \tag{3.15}$$

Considering a fixed geometry and using the reciprocity theorem which combines Ampere and Biot-Savart law, can be shown that the two mutual inductances are identical:

$$M_{12} = M_{21} = M \tag{3.16}$$

The mutual inductance *M* is a measure of the degree of coupling between the two coils. It quantifies how much the magnetic field generated by one coil influences the voltage induced in the other. Mutual inductance is a fundamental parameter in transformers, inductive sensors, and various noncontact communication systems.

Considering two coils characterized by inductance L_1 and L_2 respectively, the mutual inductance *M* can be expressed also as a function of the two coupled coils inductance:

$$M = k\sqrt{L_1 L_2} \tag{3.17}$$

The parameter *k* denotes the mutual inductive coupling coefficient, ranging between 0 and 1, reliant on the geometric configuration of both coils, the magnetic characteristics of the medium and the inductor cores, and the relative distance between the coupled circuits. Specifically, the mutual inductance *M* diminishes in accordance with the mutual inductive coupling coefficient *k* as the relative separation distance between the two coupled circuits or coils increases [84,85].

The sign of *M* depends on the direction of the current flowing in the two coils, as shown in Figure 3.6.

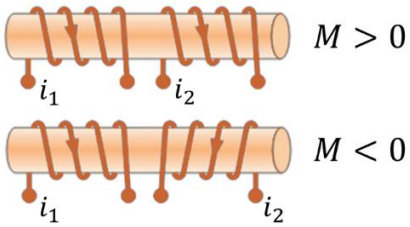

Figure 3.6 – Dependence of the sign of the mutual inductance *M* on the current flow directions on the coupled circuits.

When inductors are connected in series, allowing the magnetic field of one to interact with the other, mutual inductance affects the total inductance, either increasing or decreasing it based on the extent of magnetic coupling. This impact is contingent upon the distance between the coils and their relative orientations. Coils are cumulatively coupled when the magnetic flux generated by the current traverses through the coils in the same direction. Conversely, if the current flows in opposite directions through the coils, they are considered differentially coupled.

Considering two coils L_1 and L_2 cumulatively coupled with mutual inductance M, as shown in Figure 3.7a, the total inductance L_f of the pair results:

$$L_f = L_1 + L_2 + 2M \tag{3.18}$$

Conversely, when two coils L_1 and L_2 are differentially coupled, as shown in Figure 3.7b, the total inductance L_b of the pair is equal to:

$$L_b = L_1 + L_2 - 2M \tag{3.19}$$

Figure 3.7 – Cumulatively (a) and differentially (b) coupled coils with mutual inductance *M*.

The mutual inductance M can be calculated from the two total inductances L_f and L_b obtained with the two coils cumulatively and differentially coupled [85,86]:

$$M = \frac{L_f - L_b}{4} \tag{3.20}$$

By knowing the self-inductance values L_1 and L_2 of the two coils, the mutual inductance can be also calculated as:

$$M = \frac{L_f - L_1 - L_2}{2} \tag{3.21}$$

$$M = \frac{-L_b + L_1 + L_2}{4} \tag{3.22}$$

In the Laplace domain the inductive coupling between two purely inductive coils of inductance L_1 and L_2 respectively, can be written as:

$$V_1(s) = sL_1I_1(s) \pm sMI_2(s) \tag{3.23}$$

$$V_2(s) = sL_2I_2(s) \pm sMI_1(s) \tag{3.24}$$

where V_1 and V_2 are respectively the voltages across coil with inductance L_1 and L_2, and I_1 and I_2 are the respective current flowing in the coil.

These equations represent a system of coupled linear differential equations, and their solution can provide insights into the dynamic behaviour of coupled inductors. Analysing this system in the Laplace domain is particularly valuable for understanding transient responses and frequency-dependent behaviours.

3.1.4 Coil-coupled passive resonant sensors

As introduced in Section 3.1.1 the resonant behaviour of passive resonant sensors allows extracting the measurement information through the reading of the resonant frequency of the sensor. Resonant sensor can be effectively contactless interrogated by exploiting the electromagnetic coupling between two inductive coil and the resonant parameter of the sensor [51,66]. The adoption of the resonant measuring principle in contactless operation has two main advantages with respect to amplitude-based techniques [60,87]. Firstly, the resonant principle is robust against external interferences or nonidealities that affect the signal amplitude. Secondly, as it will be illustrated in Section 3.2, the resonant principle, combined with suitable electronic techniques, can ensure that the readout frequency is made independent from the interrogation distance.

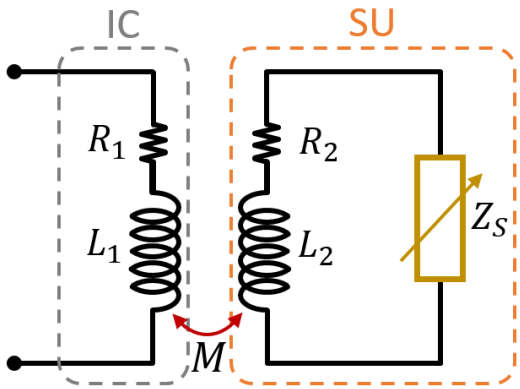

Figure 3.8 – Equivalent circuit of a coil-coupled passive sensor.

The contactless interrogation of coil-coupled passive sensors relies on the schematic circuit depicted in Figure 3.8, illustrating a generic resonant sensor unit (SU) magnetically coupled with a coil utilized for contactless interrogation of the SU. The interrogation coil (IC), commonly referred to as the primary coil, is represented schematically with inductance L_1 and series resistance R_1, and it is magnetically linked to the coil of the SU, typically referred to as the secondary coil, which is schematically represented with inductance L_2 and resistance R_2. The magnetic coupling between the coils is characterized by the mutual inductance M, which is contingent upon the geometrical configuration of primary and secondary coil, as well as their spatial orientation.

In standard noncontact interrogation scenarios, the parameters L_1, R_1, L_2, and R_2 can generally assumed to be constant, whereas the value of M can fluctuate based on alterations in the distance or alignment between the coils. However, certain specific applications may directly utilize the inductance L_2 of the SU coil as a sensing element. In this case, this inductance do not remain constant and can vary according to specific sensing conditions.

Within the SU, the secondary coil is connected to the generic impedance Z_S, which models the sensing element. Two main different SU operation mode can be considered. In one operation mode, Z_S forms with L_2, a second order network with complex conjugate poles. In this case Z_S is predominantly capacitive and L_2 influences the exploited resonant behaviour of the SU. In the other operation mode Z_S itself includes a second order network with complex conjugate poles, i.e., Z_S comprises an LCR resonant network and the dominant resonant behaviour depends mainly by Z_S. In both cases, resonance can occur in the secondary circuit where the quantity to be sensed via Z_S influences the resonant frequency and, possibly, the damping.

The following discussion considers three specific cases of the SU configuration, depicted in Figure 3.9.

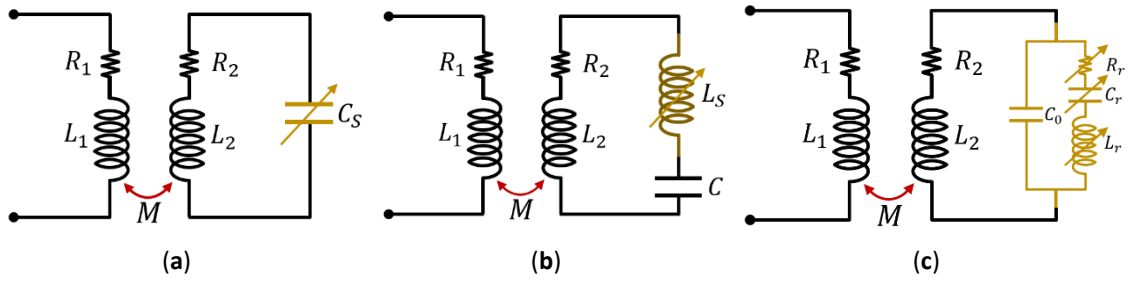

Figure 3.9 – Equivalent circuits of the three considered cases for a coil-coupled sensor unit: (a) capacitance sensor C_S; (b) inductive sensor L_S; (c) electromechanical piezoelectric resonator represented with its equivalent Butterworth–van Dyke (BVD) model.

Figure 3.9a illustrates the scenario in which Z_S is a capacitive sensor with a value of C_S, forming an LC resonant circuit in conjunction with L_2. The associated resonant frequency f_S and the quality factor Q_S of the resulting SU are determined as follows:

$$f_S = \frac{1}{2\pi\sqrt{L_2 C_S}} \tag{3.25}$$

$$Q_S = \frac{1}{R_2}\sqrt{\frac{L_2}{C_S}} \tag{3.26}$$

Figure 3.9b instead depicts the scenario where Z_S encompasses an inductive sensor L_S and a fixed capacitance C exclusively employed to achieve a resonant circuit. In this case, the associated resonance frequency and quality factor are as follows:

$$f_S = \frac{1}{2\pi\sqrt{(L_2 + L_S)C}} \tag{3.27}$$

$$Q_S = \frac{1}{R_2}\sqrt{\frac{L_2 + L_S}{C}} \tag{3.28}$$

In the last case, Z_S is a piezoelectric resonant sensor, including types such as quartz crystal resonators (QCR) and MEMS resonators To schematize their behaviour near the resonant point, the Butterworth-Van Dyke (BVD) model, a lumped-element circuit representation, is utilized, as shown in Figure 3.9c. This circuital model is divided into two primary sections: a motional or mechanical segment and an electrical component. The motional segment is a series arrangement of an inductance L_r, a capacitance C_r, and a resistance R_r, symbolizing the resonator effective mass, springiness, and energy loss mechanisms, respectively. In contrast, the electrical segment is characterized by a capacitance C_0 in parallel, reflecting the dielectric nature of the resonator material. When a voltage source stimulates the system, the mechanical resonance frequency f_r at which the motional arm current is at its maximum, aligns with the series resonance of the BVD circuit. This alignment occurs at the

frequency where the mechanical arm impedance reactance is minimal [88]. This allows for the calculation of both f_r and the resonator electromechanical quality factor Q_r:

$$f_r = \frac{1}{2\pi\sqrt{L_r C_r}} \tag{3.29}$$

$$Q_r = \frac{1}{R_r}\sqrt{\frac{L_r}{C_r}} \tag{3.30}$$

Commonly, in applications where electromechanical piezoelectric resonators function as sensors, the variable being measured induces changes in the characteristics of the motional arm components L_r, C_r, and R_r. These alterations, in turn, lead to variations in both f_r and Q_r of the sensor [51].

Due to the connection of Z_S with L_2 and R_2, the resulting resonant frequency and quality factor of the SU results:

$$f_S = \frac{1}{2\pi\sqrt{(L_r + L_2)C_r}} \tag{3.31}$$

$$Q_S = \frac{1}{R_r + R_2}\sqrt{\frac{(L_r + L_2)}{C_r}} \tag{3.32}$$

Typical electromechanical resonators, such as QCRs, exhibit substantially higher inductance values L_r compared to the coil inductances L_2 typically employed in these scenarios. In situations where $L_r \gg L_2$, it is feasible to approximate $f_S \approx f_r$.

3.2 Noncontact interrogation techniques

To effectively obtain data from the sensor unit SU via noncontact methods, specific interrogation electronic approaches are needed, particularly leveraging the benefits of coil-coupled operation. In this context, the most critical aspect to consider is the variation of the coupling factor *k* between the coils and consequently of the mutual inductance *M*, which are influenced by factors like the spatial separation, alignment, and orientation between the interrogation coil IC and the SU. Methods sensitive to changes in *k* usually necessitate maintaining these geometrical parameters stable to obtain a consistent measurement [51,89]. However, in most real-world scenarios, controlling the distance and alignment between coils consistently is often impractical or impossible. Consequently, for practical applications robust measurement techniques that remain unaffected by fluctuations in *k* are required.

Contactless interrogation passive resonant sensors can be effectively conducted using either frequency-domain or time-domain methods [51]. Frequency-domain techniques focus on the measurement of the resonator impedance, reflection coefficients, or a specific transfer function. This measurement is conducted by exiting and sensing the resonator simultaneously [49,66,67]. In contrast, time-domain approaches are based on the resonator transient free response after excitement. This involves a separation of the excitation and detection phases across different time intervals [68]. For both techniques, the independency of the sensing quantities from the reading distance has been demonstrated [51].

In the following sections, a frequency-domain technique and a time-domain technique are presented. These techniques are than employed in the succeeding chapters for the proposed application.

3.2.1 Frequency domain techniques applied to coil-coupled resonant sensors

The considered frequency domain technique for contactless interrogation of coil-coupled resonant sensor is based on the measurement and analysis of the impedance of the SU reflected to the IC.

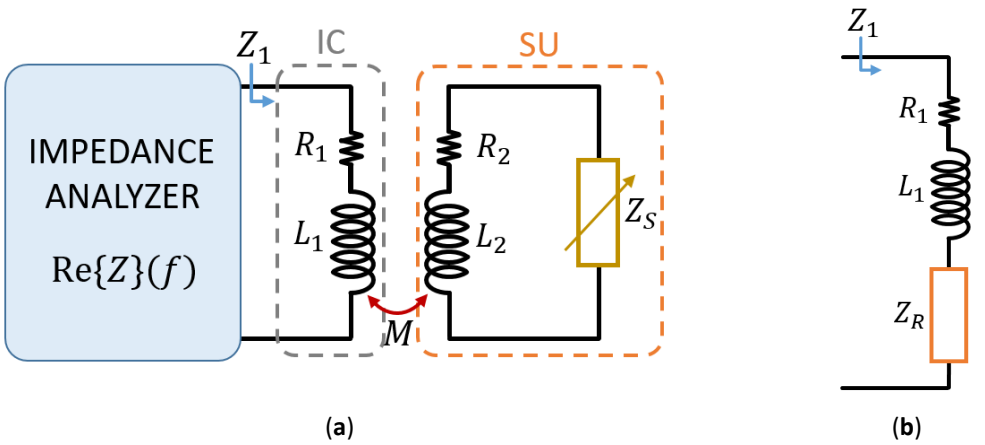

Figure 3.10 – (a) Block diagram of the readout technique based on impedance measurements; (b) equivalent circuit for the calculation of Z_1.

Figure 3.10a shows the block diagram of the readout technique based on impedance measurements, where the readout system consists in an impedance analyser connected to the interrogation coil IC schematized with L_1 and R_1. The effect of the coupling of the IC with the SU results in a reflected impedance Z_R in series with the primary coil as shown in Figure 3.10b, forming the impedance Z_1:

$$Z_1 = R_1 + j2\pi f L_1 + Z_R \tag{3.33}$$

Considering the case of a SU with capacitive sensing element C_S, which equivalent circuit is shown in Figure 3.11a, the impedance Z_1, as a function of f results:

$$Z_1 = R_1 + j2\pi f L_1 + 4\pi^2 f^2 k^2 L_1 L_2 \frac{1}{R_2 + j2\pi f L_2 + \frac{1}{j2\pi f C_S}} \tag{3.34}$$

It can be observed from Equation (3.34) that the effect of the coupling with the SU makes the total impedance Z_1 dependent on the coupling factor k.

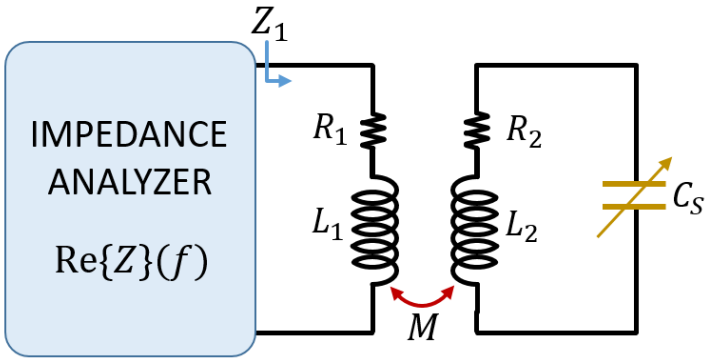

Figure 3.11 – Block diagram of the interrogation system based on impedance measurement with capacitive SU.

The resonant frequency f_S and the quality factor Q_S of the SU, defined in Equations (3.25) and (3.26), can be obtained from the real part of Z_1 [66], which is mathematically represented by the following relation:

$$\mathrm{Re}\{Z_1\}(f) = R_1 + 4\pi^2 f^2 k^2 L_1 L_2 \frac{R_2}{R_2^2 + \left(2\pi f L_2 - \frac{1}{2\pi f C_S}\right)^2}. \tag{3.35}$$

A local maximum in $\mathrm{Re}\{Z_1\}$ is observed at a frequency denoted as f_m. This maximum is discerned by nullifying the derivative of Equation (3.35) in respect to f. Can be derived that f_m is independent from k and it is related to f_S and Q_S [66]. Indeed, combining Equations (3.25), and (3.35), it results the following equation for $\mathrm{Re}\{Z_1\}$:

$$\mathrm{Re}\{Z_1\}(f) = R_1 + 2\pi f L_1 k^2 Q_S \frac{\frac{f}{f_S}}{1 + Q_2^2\left(\frac{f}{f_S} - \frac{f_S}{f}\right)^2}. \tag{3.36}$$

Consequently, it results:

$$f_m = f|_{\max(Re\{Z_1\})} = \frac{2Q_S}{\sqrt{4Q_S^2 - 2}} f_S \tag{3.37}$$

$$Q_S \approx \frac{f_S}{\mathrm{BW}_{f_{FWHM}}} \tag{3.38}$$

As shown in Figure 3.12,Figure 3.1 BW_{f_FWHM} is the full width at half maximum FWHM of Re{Z_1}, around f_m [51,66]. If Q_S is sufficiently large with respect to unit, f_m closely approximates f_S. Consequently, the measurement of f_m and BW_{f_FWHM} in Re{Z_1} allows to determine f_S and Q_S of the capacitive SU. This method is advantageous as it allows for the independent determination of these parameters without the influence of k which only affects the amplitude of Re{Z_1} as reported in [51].

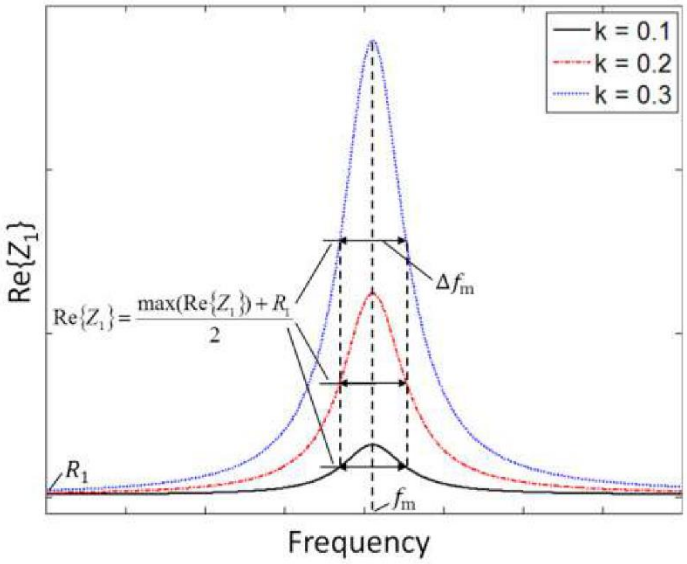

Figure 3.12 – Real part of Z_1 as a function of frequency for three different values of k [51].

The described approach can be also applied in the case with an inductive sensor L_S and a fixed capacitance C_R employed to achieve a resonant circuit, as described in Section 3.1.4.

Considering instead the case with an electromechanical piezoelectric resonator in the SU as shown in Figure 3.13, the impedance Z_1 measured at the IC results:

$$Z_1 = R_1 + j2\pi f L_1 + 4\pi^2 f^2 k^2 L_1 L_2 \frac{1}{R_2 + j2\pi f L_2 + \frac{1}{j2\pi f C_0} \parallel \left(j2\pi f L_r + \frac{1}{j2\pi f C_r} + R_r \right)} \tag{3.39}$$

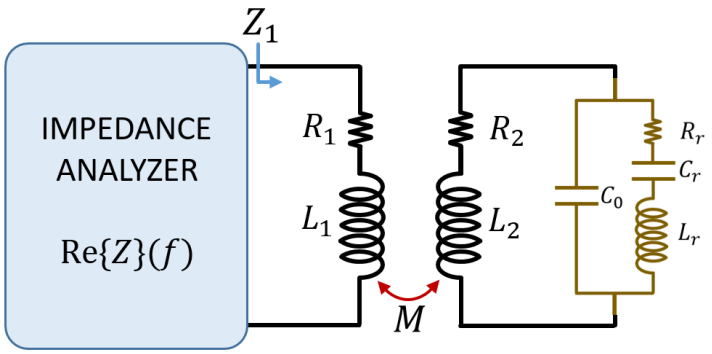

Figure 3.13 – Block diagram of the interrogation system based on impedance measurement with electromechanical piezoelectric resonator represented with its equivalent Butterworth–van Dyke (BVD) model.

Close to the resonant frequency $f_r = ½\pi(L_rC_r)^{1/2}$ of the electromechanical piezoelectric resonator, the impedance of its motional arm $Z_r = R_r + j2\pi fL_r + 1/(j2\pi fC_r)$ has a magnitude typically much smaller than that of the impedance of C_0, i.e., $|Z_r| \ll 1/2\pi f_r C_0$. Then, the presence of C_0 can be neglected, resulting in the simplified equivalent circuit of Figure 2.14a. With this assumption, around the resonant frequency $\mathrm{Re}\{Z_1\}$ can be approximated with:

$$\mathrm{Re}\{Z_1\}(f) \approx R_1 + 4\pi^2 f^2 k^2 L_1 L_2 \frac{R_r + R_2}{(R_r + R_2)^2 + \left[2\pi f (L_r + L_2) - \frac{1}{2\pi f C_r}\right]^2}. \tag{3.40}$$

Equation (3.40) has the same form as Equation (3.35) and hence, also in this case, can be applied the Equations (3.37) and (3.38) with the same consideration and where f_S and Q_S are given by Equation (3.31) and (3.32) respectively. In this case as well, the coupling factor k solely functions as an amplitude factor, thereby not affecting the resonant frequency and quality factor obtained from the real part of the impedance Z_1 [51].

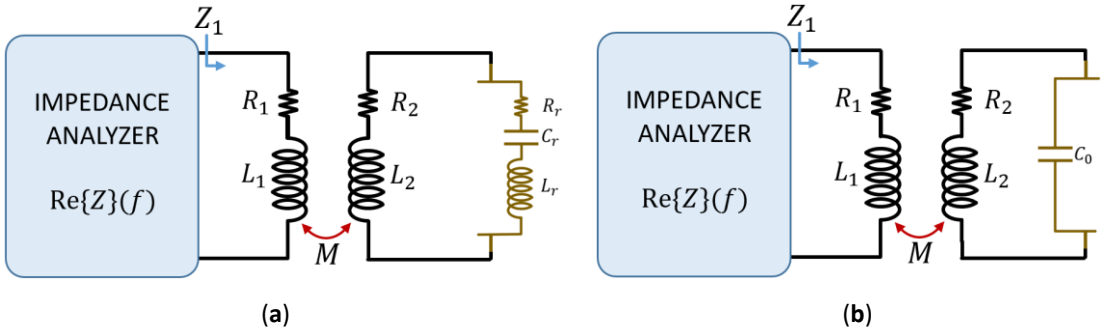

Figure 3.14 – (a) Block diagram of the interrogation system with equivalent circuit of electromechanical piezoelectric resonator around f_r; (b) block diagram of the interrogation system with equivalent circuit of electromechanical piezoelectric resonator for f>>f_r.

The presence of C_0 impact the behaviour of Z_1 for the frequencies $f \gg f_r$ where the impedance magnitude of C_0 is smaller than the impedance magnitude of Z_r, which therefore can be neglected. With reference with the consequent equivalent circuit of Figure 3.14b, $\mathrm{Re}\{Z_1\}$ results:

$$Re\{Z_1\} \approx R_1 + 4\pi^2 f^2 k^2 L_1 L_2 \frac{R_2}{R_2^2 + \left(2\pi f L_2 - \frac{1}{2\pi f C_0}\right)^2}. \tag{3.41}$$

Also Equation (3.41) has the same form as Equation (3.35), and it can be therefore derived that $\mathrm{Re}\{Z_1\}$ presents a maximum at f_{m_el}:

$$f_{m\_el} = f_{el} \frac{2Q_{el}}{\sqrt{4Q_{el}^2 - 2}}. \tag{3.42}$$

Where in this case the electrical resonant frequency and quality factor are:

$$f_{el} = \frac{1}{2\pi\sqrt{L_2 C_0}} \tag{3.43}$$

$$Q_{el} = \frac{1}{R_2}\sqrt{\frac{L_2}{C_0}}. \tag{3.44}$$

The preceding analysis elucidates that Re{Z_1} of SU including electromechanical piezoelectric resonators exhibits dual peaks: one corresponding to the mechanical resonance f_r and the other to the electrical resonance f_{el}. Considering L_r » L_2, coupled with the typical scenario where C_r « C_0, it ensures that f_{el} significantly exceeds f_r. Consequently, it becomes apparent that both resonances can be effectively leveraged for the contactless interrogation of sensors founded on electromechanical piezoelectric resonators.

3.2.2 Time domain techniques applied to coil-coupled resonant sensors

As introduced, the time-domain techniques for contactless interrogation of passive resonant sensors, also named time-gated techniques, are based on the resonator transient free response after excitement of the resonant elements of the SU.

The operational methodology of the time-gated technique is visually represented in Figure 3.15a, focusing on a SU equipped with a capacitive sensing element C_S . This technique is characterized by two distinct phases: the excitation phase and the detection phase [68].

In the excitation phase, the SU is energized through the coupling of IC with L_2 and as consequence of the sinusoidal excitement signal $v_{exc}(t)$ applied to L_1. Subsequently, during the detection phase, the switch shifts to the D position, disconnecting the excitation signal. The IC is then connected to a readout circuit characterized by a high-impedance input, ensuring negligible current flowing through L_1 and R_1.

During the detection phase, the readout circuit input voltage $v_1(t)$, can be obtained by applying the inverse Laplace transform to the corresponding voltage $V_1(s)$ in the Laplace domain, where s represents the complex frequency. Given the SU configuration as a second-order LCR network, the resultant $v_1(t)$ exhibits the form of a damped sinusoid, characterized by a frequency f_d and a decay time τ_d as explained in Section 3.1.2. These parameters allows determining the resonant frequency f_S and the quality factor Q_S of the SU, allowing this technique to be utilized for the contactless interrogation of passive resonant sensors.

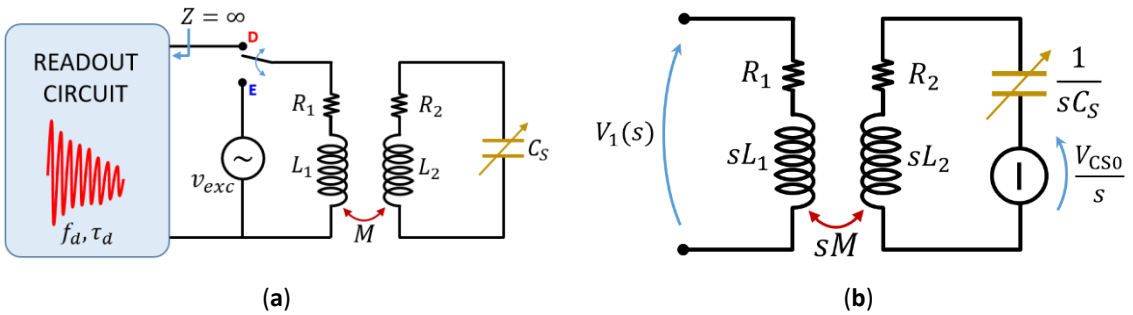

Figure 3.15 – (a) Block diagram of the time-gated technique with capacitive SU; (b) equivalent circuit of the time-gated technique with capacitive SU during the detection phase.

Considering the initiation of the detection phase D at t = 0, the readout voltage $v_1(t)$ is influenced by the initial states of the reactive elements C_S, L_1, L_2 and M at t = 0. These initial conditions primarily affect the starting amplitude of $v_1(t)$ for t > 0, while the complex frequencies of the network remain unchanged, thus preserving f_d and τ_d. Consequently, for simplification without loss of generality, the single initial condition V_{CS0}, defined as the voltage across C_S at t = 0, can be considered, setting aside the other initial conditions. As an equivalent alternative that does not change the consequences of the present treatment, V_{CS0} can also be seen as an effective initial condition. Figure 3.15b shows the time-gated configuration in the Laplace domain during the detection phase taking in account the considered hypothesis for the initial conditions. According, the expression of $V_1(s)$ in the Laplacian domain results:

$$V_1(s) = k\sqrt{\frac{L_1}{L_2}}V_{CS0}\frac{s}{s^2 + s\frac{R_2}{L_2} + \frac{1}{L_2 C_S}} \tag{3.45}$$

By applying the inverse Laplace transform the corresponding time expression $v_1(t)$ of $V_1(s)$ results:

$$v_1(t) = k\sqrt{\frac{L_1}{L_2}}\sqrt{\frac{4Q_S^2}{4Q_S^2 - 1}}V_{CS0}e^{t/\tau_d}\cos\left[2\pi f_d t - \arctan\left(\frac{1}{2\pi f_d \tau_d}\right)\right] \tag{3.46}$$

As can be seen from Equation (3.46) and from the plots of Figure 3.16, the signal $v_1(t)$ is a damped sinusoid with frequency f_d and decay time τ_d. From equation of underdamped harmonic oscillator can be derived that the relationship between f_d and τ_d with f_S and Q_S of the SU are the following:

$$f_d = f_S \sqrt{1 - \frac{1}{4Q_S^2}} \tag{3.47}$$

$$\tau_d = \frac{Q_S}{\pi f_S}. \tag{3.48}$$

Assuming Q_S sufficiently large with respect to unit, it results $f_d \approx f_S$.

As described in [51] and as evident from Equation (3.46), the coupling factor k only acts as a scaling factor on the amplitude of $v_1(t)$ without affecting f_d or τ_d.

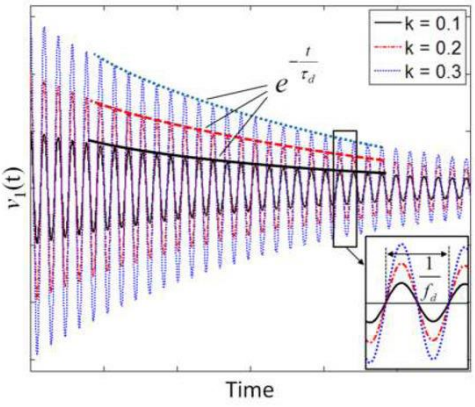

Figure 3.16 – Voltage $v_1(t)$ during the detection phase calculated for three different values of the coupling factor k [51].

Under the considered assumptions, the presented time-gated technique allows to determine the frequency f_S and quality factor Q_S of the capacitive SU, independently of k. This technique can be effectively applied also to the case with electromechanical piezoelectric resonator used as sensing element of the SU [68,90].

3.2.3 Effect of parasitic capacitance at the interrogation coil in frequency domain interrogation techniques

The proposed technique presented in Section 3.2.1 based on the measurements of the real part of the equivalent impedance at the interrogation coil, present limitation associated the presence of unavoidable parasitic capacitance. In particular unavoidable nonidealities result in a lumped parasitic capacitance C_P that appears in parallel to L_1 as shown in Figure 3.17. The represented parasitic capacitance encapsulates the cumulative effect arising from the parasitic capacitance of the inductor L_1, the capacitance of the connections, and the input stage of the electronics used for impedance measurements, all of which appear in parallel to the inductor L_1 of the interrogation coil.

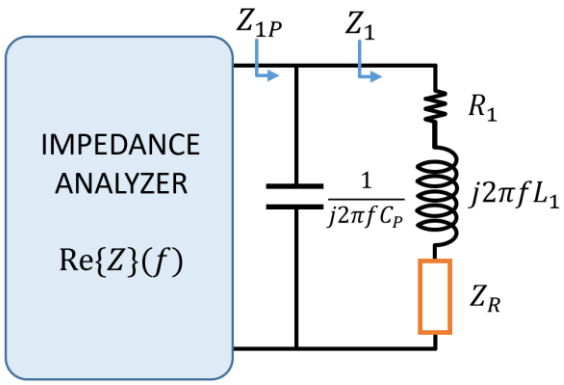

Figure 3.17 – Block diagram of the frequency-domain interrogation technique with parasitic capacitance and equivalent circuit of the impedance Z_{1P} of a coil-coupled capacitance sensor.

Considering the case with the sensor unit composed by only the coupling inductor L_2 and a capacitive sensing element C_S, taking in account the presence of C_P, the real part of the impedance Z_{1P} at the interrogation coil results [89]:

$$\mathrm{Re}\{Z_{1P}\} = \mathrm{Re}\left\{\frac{\left(R_1 + j2\pi f L_1 + \frac{4\pi^2 f^2 k^2 L_1 L_2}{R_2 + j2\pi f L_2 + \frac{1}{j2\pi f C_S}}\right)\frac{1}{j2\pi f C_P}}{R_1 + j2\pi f L_1 + \frac{4\pi^2 f^2 k^2 L_1 L_2}{R_2 + j2\pi f L_2 + \frac{1}{j2\pi f C_S}} + \frac{1}{j2\pi f C_P}}\right\} \tag{3.49}$$

Equation (3.49) shows that in this case the coupling coefficient k not only acts as an amplitude scaling factor, but also affect the resonance parameter of the SU and therefore it is not possible to independently extract the resonant frequency f_S , and quality factor Q_S of the SU [50]. Numerical analysis of Equation (3.49) shows that the real part of the equivalent impedance Z_{1P} presents two peak. The first peak can be associated to a primary resonance near $f_S = 1/2\pi(L_2C_S)^{½}$, while the second peak to a secondary resonance near $f_P = 1/2\pi(L_1C_P)^{½}$ [50,89,91].

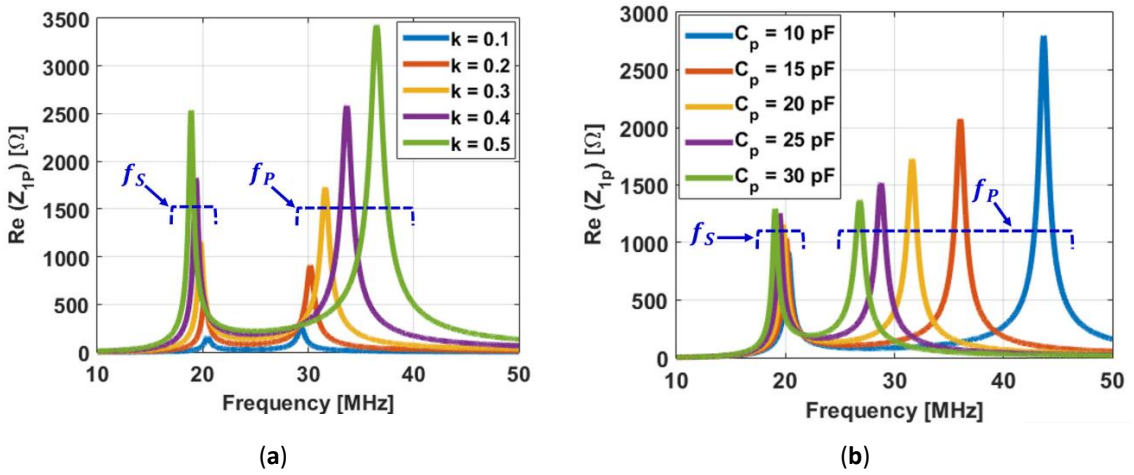

Figure 3.18 – (a) Numerical simulation of the real part of equivalent impedance under the presence of parasitic capacitance C_P with increasing values of coupling coefficient k [50]; (b) simulation of the real part with varying parasitic capacitance C_P [50].

Both the resonance are influenced by the coupling coefficient k and by the value of C_P. Figure 3.18a shows the obtained Re{Z_{1P}} for fixed C_P and variable k, while Figure 3.18b shows the obtained Re{Z_{1P}} for fixed k and variable C_P. It results that when C_P is not negligible it is not possible to determine with independence from k, and thus from the interrogation distance d, the resonant frequency f_S and quality factor Q_S of the SU [50,51].

3.2.4 Effect of parasitic capacitance at the interrogation coil in time domain interrogation techniques

In Section 3.2.2 has been exposed a time domain technique for contactless interrogation of coil-coupled resonant sensors. The presented analytic analysis shows that this approach is independent from the coupling factor *k*, and thus from the interrogation distance *d*. However, considering also in this case the presence of a parasitic capacitance C_P in parallel to the interrogation coil and considering a SU composed by the coil L_2 and a capacitive sensing element C_S, as shown in Figure 3.19, the expression (3.45) of $V_1(s)$ in the Laplacian domain became [51]:

$$V_{1P}(s) = k\sqrt{\frac{L_1}{L_2}}\frac{sV_{CS0}C_S L_2}{s^4 C_S C_P L_1 L_2(1-k^2) + s^3 x + s^2 y + sz + 1}, \tag{3.50}$$

where

$$\begin{aligned} x &= C_S C_P (L_1 R_2 + L_2 R_1) \\ y &= C_S L_2 + C_P L_1 + C_S C_P R_1 R_2 \\ z &= C_S R_2 + C_P R_1 \end{aligned} \tag{3.51}$$

and where V_{CS0} is the voltage across C_S at $t = 0$. From Equation (3.50) it can be observed that the coupling coefficient *k* not only acts as amplitude scaling factor, but also affects the fourth-order polynomial at the denominator. The decomposition of a fourth order polynomial can results in two pairs of complex conjugate roots. In this context, the s^4 term associated with the coupling coefficient, represented as $(1 - k^2)$, suggests a dependency of the complex frequencies ($s = j2\pi f$) on the coefficient *k* [51]. When performing the inverse Laplace transform on equation (3.50), it becomes evident that the output voltage signal is composed of two sinusoidal functions, each exhibiting a damping effect [50]:

$$v_{1P}(t) = A_1 e^{-\frac{t}{\tau_{d1}}}\cos(2\pi f_{d1} t - \theta_1) + A_2 e^{-\frac{t}{\tau_{d2}}}\cos(2\pi f_{d2} t - \theta_2), \tag{3.52}$$

where A_1 and A_2 are amplitude coefficients and θ_1 and θ_2 are phase angles which depend on the parameters of the circuit and the initial conditions. The damped frequencies f_{d1} and f_{d2} and the decay times, τ_{d1} and τ_{d2} can be calculated as the complex conjugate solutions $p_{1,2} = 1/\tau_{d1} \pm j2\pi f_{d1}$ and $p_{3,4} = 1/\tau_{d2} \pm j2\pi f_{d2}$ obtained by setting the denominator of Equation (3.50) equal to zero. It can be verified that f_{d1} is close to $f_P = 1/2\pi(L_1C_P)^{1/2}$, while f_{d2} is close to $f_S = 1/2\pi(L_2C_S)^{1/2}$ [89,91]. However both f_{d1} and f_{d2} results dependent on k. In the condition where R_2 is sufficiently smaller than R_1 it results a decay time τ_{d2} larger than τ_{d1}. Consequently the damped sinusoid at f_{d1} collapses more rapidly than that at f_{d2}, and it becomes negligible as time elapses [51]. Since f_{d2} depends on k due to the effect of parasitic capacitance C_P, also the independence from the interrogation distance of the time-domain technique is vanishes.

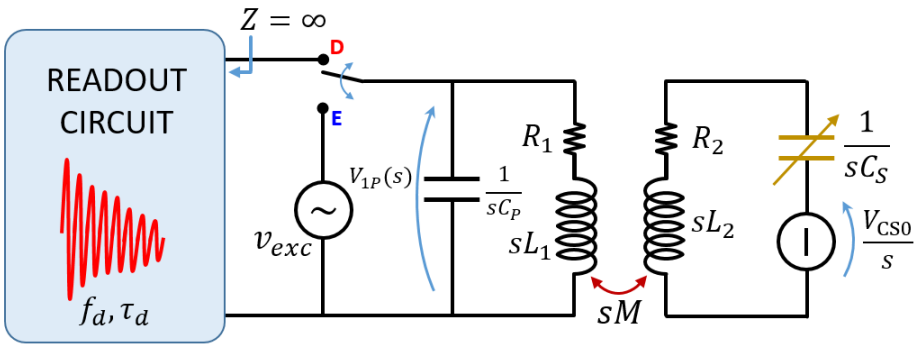

Figure 3.19 – Block diagram of the interrogation system with equivalent circuit in the Laplace domain to derive $V_{1P}(s)$ during the detection phase of the time-gated technique applied to a coil-coupled capacitance sensor.

Considering the case where the SU involve an electromechanical piezoelectric resonator, the time-gated technique again presents an extra damped sinusoid in $v_{1P}(t)$ due to the interaction of C_P with L_1 depicted in Figure 3.20. However, considering a value of L_r three orders of magnitude over L_2, which is a consistent condition considering the typical parameter of for example QCRs, numerical analysis shows that the extra damped sinusoid dissipates faster than due to the piezoelectric resonator response [51]. This indicates that considering a SU with electromechanical resonators like QCRs, the technique remain practically independent from the coupling factor k, and thus from the interrogation distance d, also with a not-negligible C_P.

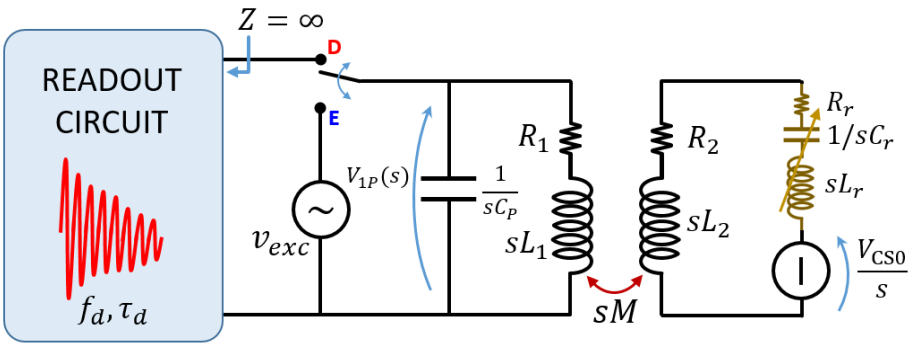

Figure 3.20 – Block diagram of the interrogation system with equivalent circuit in the Laplace domain to derive $V_{1P}(s)$ during the detection phase of the time-gated technique applied to an electromechanical piezoelectric resonator.

3.2.5 Parasitic capacitance compensation

As detailed in Sections 3.2.3 and 3.2.4 the presence of parasitic capacitances in parallel with the interrogation coil impacts the distance sensitivity during the contactless interrogation of coil-coupled resonant sensors. To counteract this intrinsic phenomenon, a compensation circuit has been proposed in [51]. This circuit can be connected in parallel to the interrogation coil and is designed to neutralize the parasitic capacitances in both frequency and time domain methodologies, thereby enhancing the precision of noncontact, distance-independent measurement of resonant sensors [51,89].

Figure 3.21 illustrates the schematic of a circuit proposed in [89] designed to mitigate parasitic capacitance effects.

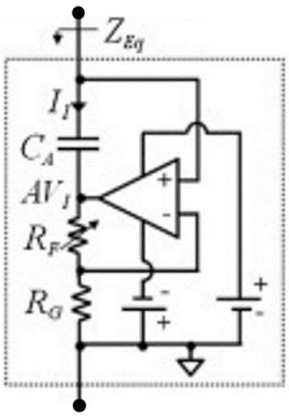

Figure 3.21 – Block diagram of circuit for the compensation of the parasitic capacitance C_P [89].

This design utilizes a high-bandwidth operational amplifier configured as a negative impedance converter (NIC), thereby generating an effective negative capacitance of $-C_C$.

Specifically, the voltage V_1 across the interrogation coil is fed to a non-inverting amplifier A_C which features a gain $A = (1 + R_F/R_G) > 1$. This amplifier is arranged in a positive feedback loop with the capacitor C_A. As a consequence, the current flowing through C_A can expressed as:

$$I_1 = j2\pi f C_A (V_1 - AV_1) \tag{3.53}$$

Subsequently, the equivalent input impedance of the amplifier $Z_{Eq} = V_1/I_1$ which results in parallel to C_P and to the interrogation coil presents the following expression [89]:

$$Z_{Eq} = \frac{V_1}{I_1} = \frac{V_1}{j2\pi f C_A (V_1 - AV_1)} = -\frac{R_G}{j2\pi f C_A R_F} = \frac{1}{j2\pi(-C_C)}, \tag{3.54}$$

where $-C_C = -C_A \cdot R_F/R_G$ becomes an effective negative capacitance. As can be noted from the Equation (3.54), if the gain A is made adjustable, i.e. making R_F variable, $-C_C$ can be tuned. By an appropriate tuning process it is therefore possible compensate and eventually fully cancel C_P.

The illustrated compensation circuit is applicable to both the frequency-domain and time-domain techniques described in Sections 3.2.3 and 3.2.4 respectively.

In Figure 3.22 is illustrated the integration of the compensation circuit presented in [51], within the impedance measurement circuit where the interrogation coil is connected to an impedance analyser. The total parasitic capacitance C_P encompasses the contributions given by the parasitic capacitances of the interrogation coil (C_1), the connections (C_L) and the equivalent capacitance of the input of the impedance analyser (C_I). In the compensated condition, i.e. when $C_C = C_P$, k-independent measurements of the resonant frequency and quality factor can be obtained from the real part of the measured impedance [51].

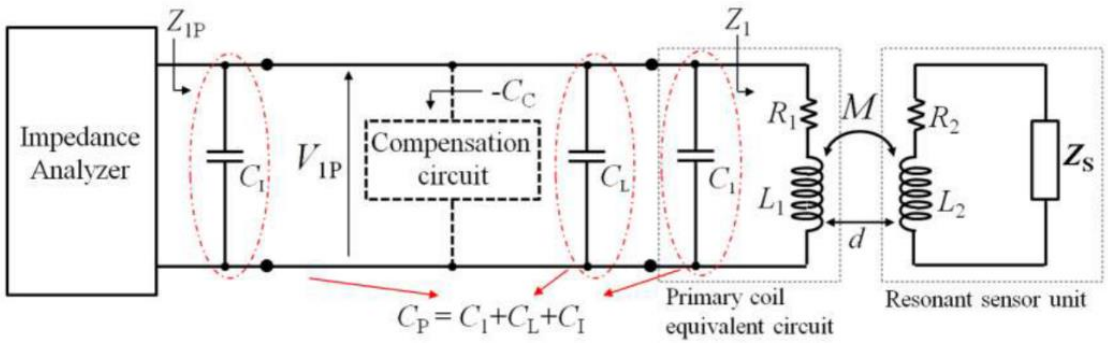

Figure 3.22 – Block diagram of the interrogation system based on impedance measurement technique with parasitic capacitance compensation circuit [B].

Figure 3.23 shows the block diagram of the interrogation system based on of time-gated technique with the compensation circuit, as presented in [51]. The total parasitic capacitance C_P accounts for the contributions of the parasitic capacitances of the primary coil (C_1), the connections (C_L), the analog switch *SW* (C_{SW}), and the equivalent input capacitance of the amplifier AG (C_I).

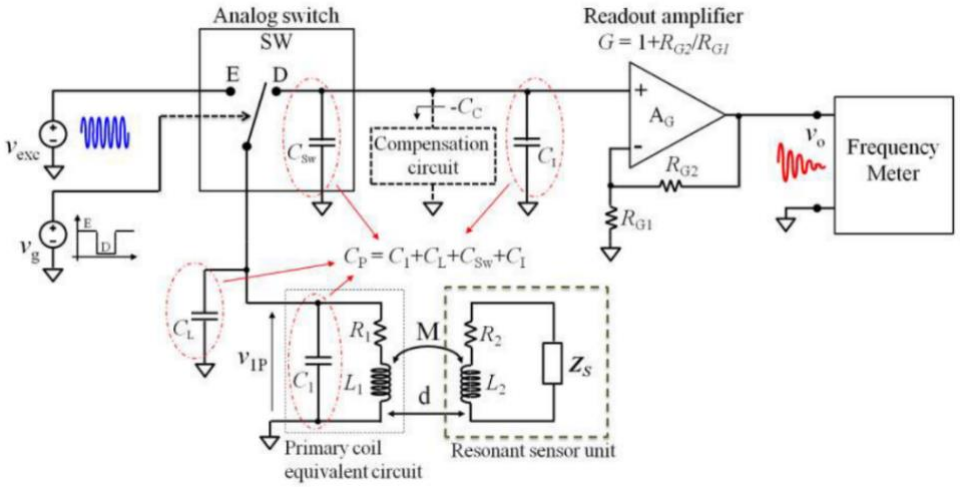

Figure 3.23 – Block diagram of the interrogation system based on of time-gated technique with parasitic capacitance compensation circuit [51].

As for the impedance measurement circuit, the objective of the compensation circuit is to inhibit the effect of the overall parasitic capacitance that arises during the reading phase of the SU (Sensing Unit), a condition achieved by setting $C_C = C_P$. In this condition from the

analysis of the free decay response of the SU it is possible to determine the correspondent resonant frequency and quality factor with independence from the coupling factor *k* and thus from the interrogation distance.

Chapter 4

Noncontact interrogation of piezoelectric MEMS resonators for temperature measurement

In this chapter the development and experimental characterization of an electronic technique and system for noncontact reading of the temperature-dependent resonant frequency of piezoelectric MEMS (Micro-Electro-Mechanical System) resonators is presented. The proposed approach integrates the noncontact interrogation method presented in Chapter 3, applied to an AlN (Aluminum Nitride) TPoS (Thin-film Piezoelectric on Silicon) MEMS resonator, with a post-processing technique based on autocorrelation analysis. Specifically, the resonator response is down-mixed using a tunable local oscillator, and the resulting signal is then processed through autocorrelation techniques to determine the resonant frequency of the resonator. This innovative method has been applied to temperature sensing by exploiting the temperature-dependent characteristics of an AlN TPoS resonator operating in the radial contour-mode configuration. This leverages the temperature coefficient of frequency (TCF) inherent to the resonator.

4.1 Overview of MEMS sensors

Microelectromechanical systems, commonly known as MEMS, are a pivotal technology with broad applications in sectors such as consumer electronics [92], automotive industry [93], biomedical [94], energy harvesting [95], and more [96,97]. This technology is integral to the Industrial Revolution 4.0, which leans heavily on the Internet of Things (IoT) for gathering data to enhance smart living environments [98].

MEMS devices come in a variety of sizes, typically ranging from less than a micrometer to several millimeters [99,100]. These can be simple structures or more complex systems involving several moving elements and integrated microelectronics. A significant aspect of recent advancements in MEMS technology is the focus on enhancing the performance of transducers. This involves not only the development of new MEMS sensors and actuators but also improving resolution and sensitivity through advanced techniques and electronic circuits. This shift towards more sophisticated technology has been driven by the growing demand for devices that can deliver precise measurements and withstand various environmental conditions. This heterogeneous integration extends to merging MEMS with various fields like microelectronics, nanotechnology, and photonics [98].

Micro/nanoelectromechanical systems function by continuously converting energy between mechanical and electrical states [101]. This process uses different transduction methods, with capacitive [102], thermal/piezoresistive [103], and piezoelectric [104] elements being the most widely used. Electrostatic forces, significant at small scales, are used in applications like microsystems, where they provide an attractive force in systems such as parallel plate and comb drive capacitors. Piezoelectric materials, on the other hand, are advantageous in MEMS due to their ability to produce significant actuation at lower drive voltages and with lower power consumption. As MEMS devices scale down in size, piezoelectric forces become more relevant, maintaining high energy density for actuation. For this reason, piezoelectricity is favored in applications like sensors [105], actuators [106], energy harvesters [107].

4.2 AlN TPoS MEMS resonator

As previously introduced, this chapter presents the application of a time-gated electronic technique with autocorrelation analysis, for noncontact reading of resonant passive sensors, to a MEMS resonator used as temperature-sensitive element. The chosen MEMS resonator, shown in Figure 4.1, has been developed in collaboration with the research group of University of Hong Kong coordinated by Joshua E.-Y. Lee and has been recently introduced and utilized in [108]. It is a 400 µm-radius AlN TPoS disk, fabricated using the PiezoMUMPs (Piezo Multi-User MEMS Processes) foundry process offered by MEMSCAP [109]. The manufacturing process commences with a silicon-on-insulator (SOI) wafer, featuring a 10-µm-thick silicon device layer (Si). This device layer is an n-type layer with surface doping, enabling the creation of an ohmic layer during a subsequent metallization stage for defining contact pads and electrodes.

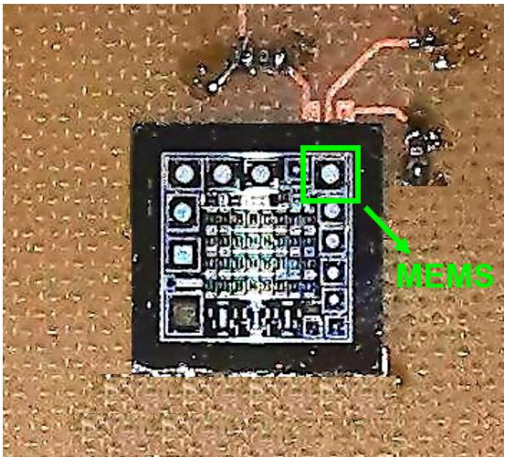

Figure 4.1 – Picture of the silicon substrate containing the adopted AlN TPoS disk MEMS resonator.

Following this, a 200-nm-thick thermal oxide layer is grown and etched using reactive ion etching, serving as an insulation layer on the silicon device layer, as illustrated in Figure 4.2a.

Subsequently, a 500 nm-thick layer of AlN is deposited as the piezoelectric material through reactive sputtering. The AlN layer is then patterned using wet etching. The preference for AlN arises from its potential for chip-level integration and compatibility with CMOS technology, setting it apart from other piezoelectric materials such as PZT and ZnO.

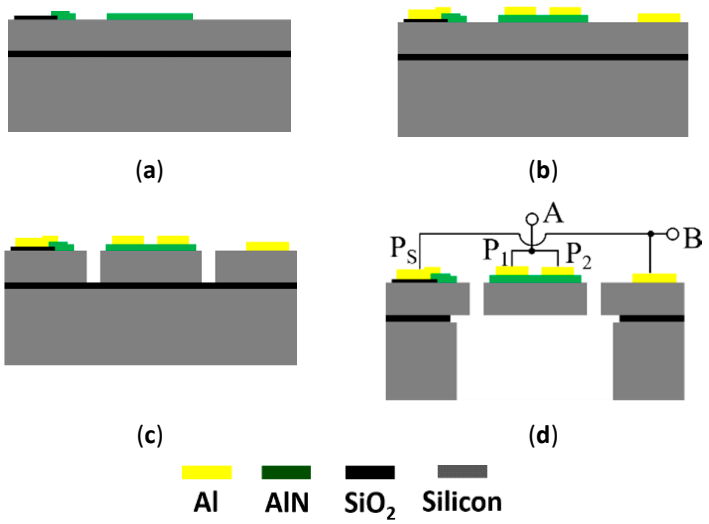

Figure 4.2 – (a) Deposition and patterning of 200 nm thermal oxide followed by deposition and patterning of 500-nm-thick AlN film; (b) deposition and patterning of 20 nm +1 m-thick Cr/Al metal stack; (c) front side DRIE (deep reactive ion etching) of 10-m-thick silicon device layer; (d) back side DRIE of silicon substrate followed by buffered HF (hydrogen fluoride) etch of the buried oxide layer to release the device [108].

The next step involves the patterning and deposition of a metal stack composed of 20-nm-thick Cr and 1-µm-thick Al using a lift-off process. This defines the contact pads and top electrodes of the resonator, as depicted in Figure 4.2b. The silicon device layer then undergoes lithographic patterning and deep reactive ion etching (DRIE) to define the features of the resonator, as shown in Figure 4.2c. This process includes creating T-shaped tethers on all four sides of the disk resonator to provide structural support. In this case, lateral support is necessary for the resonator, as central clamping is unfeasible due to the release method.

Releasing the structure from the substrate involves initially applying a protective polymer coat to the top side of the wafer. The back of the SOI wafer is lithographically patterned to establish the cavity opening, and the handling layer of the wafer is etched using DRIE, followed by the removal of the buried oxide layer through wet oxide etching. Subsequently, the protective coat on the front side is removed to release the device, as shown in Figure 4.2d, and then the dicing process is performed. In this instance, the back cavity takes on a circular form, which can be observed in Figure 4.3 as the dark ring surrounding the TPoS

disk. The inclusion of a 10-µm-thick silicon layer enhances energy storage in the resonator, consequently elevating quality factors when compared to structures composed only of AlN. The two Al top electrodes, P1 and P2, in conjunction with the bottom ground electrode, PS, enable the device to operate either as a two-port resonator or, by shorting P1 and P2, as a one-port resonator between connections A and B, as illustrated in Figure 4.2d.

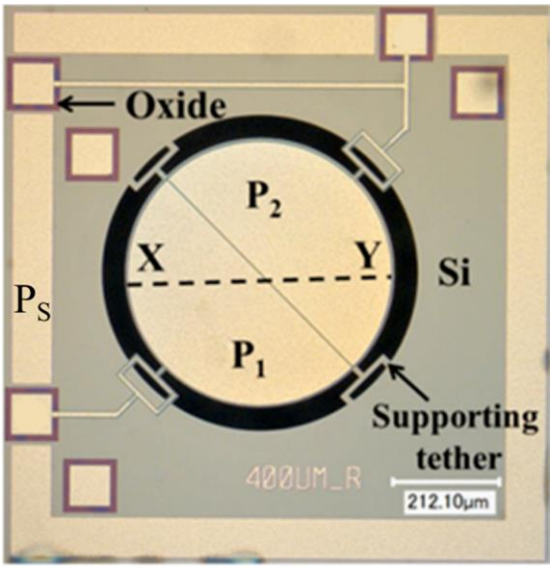

Figure 4.3 – Optical micrograph of the adopted AlN (aluminium nitride) TPoS (thin-film piezoelectric on-silicon) MEMS (micro-electromechanical system) resonator [108].

By comparing the top view of the device shown in Figure 4.3 with the side view schematic in Figure 4.2d, it becomes evident that the contact pads of P1 and P2 are isolated from the silicon device layer by a 200-nm thermal oxide layer, while the wide frame tracks surrounding the resonator serve as grounding pads, making contact with the silicon device layer (PS).

4.3 Noncontact interrogation of MEMS resonator temperature sensor

The idea of noncontact sensing for physical quantities holds substantial appeal in situations where wired connections pose significant challenges or are altogether impractical. This

particularly comes into play when conducting measurements within enclosed or hermetic environments, where the installation of cabling is both obtrusive and infeasible. Noncontact sensing typically requires the deployment of an interrogation unit capable of communicating with a sensor unit in close proximity [110]. Moreover, in field applications, it is crucial that the readout signal obtained by the interrogation unit remains independent of the distance from the sensor unit. This necessitates an approach inherently robust against potential external interferences caused by proximate devices or environmental disturbances. In this context, the use of resonant sensors proves highly advantageous. These sensors convey measurement information through variations in their resonant frequency, which remains unaffected by shifts in the readout signal amplitude. Furthermore, resonant sensors, characterized by their passive nature, are capable of operation in environments that are hostile to active electronics, offering a clear advantage.

Effective noncontact interrogation relies on the near-field electromagnetic coupling between an interrogation unit and a sensor unit. Within this framework, various methods have emerged, encompassing both frequency-domain and time-domain techniques for noncontact interrogation, suitable for capacitive sensors or piezoelectric resonators as presented in Chapter 3.

Frequency-domain methods involve the simultaneous excitation and sensing of the resonator, allowing for the measurement of impedance and specific transfer functions [53,66,67]. In contrast, time-domain techniques employ temporal separation between excitation and detection phases. They take advantage of the resonator transient response, which primarily relies on its mechanical characteristics and tends to remain unaffected by the distance between the interrogation and sensor units [111].

Traditionally, readout frequencies are determined using conventional bench instruments like frequency counters. Alternatively, signal processing techniques offer a valuable avenue, as evidenced by the demonstrated effectiveness of autocorrelation techniques, which can be applied to this purpose [68]. The choice between traditional instrumentation and signal processing hinges on the specific needs and objectives of the interrogation process.

In this Chapter, the temperature sensitivity of an AlN TPoS MEMS resonator has been leveraged as a novel sensing technique integrated with the noncontact interrogation method presented in Chapter 3, and with a post-processing technique based on autocorrelation analysis.

Figure 4.4 illustrates the schematic diagram of the proposed system designed for the noncontact interrogation of AlN TPoS MEMS resonators. The proposed system comprises an interrogation unit (IU) that is magnetically coupled to the sensor unit (SU) via the mutual inductance *M* established between the interrogation coil (L_1) and the sensor coil (L_2), which are separated by a distance *d*. The sensor coil is connected to the piezoelectric resonator. Around the resonant frequency f_s the piezoelectric resonator can be modelled by the equivalent Butterworth-Van Dyke (BVD) circuit. The IU generates the required signals using three Direct Digital Synthesizer (DDS) devices, denoted as channels CH0, CH1, and CH2, respectively.

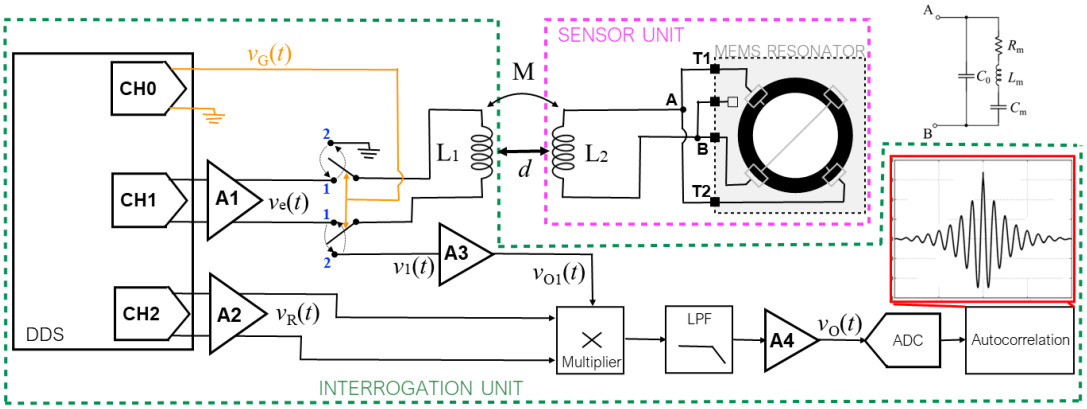

Figure 4.4 – Block diagram of the proposed noncontact interrogation system and BVD model of the MEMS resonator around its resonant frequency.

The employed DDSs (AD9834) are programmable devices, equipped with 28-bit frequency registers and a 75 MHz clock rate, enabling to generate sinusoidal signals with a frequency resolution of approximately 0.28 Hz. These devices feature a 3-wire serial interface that is compatible with standards such as SPI, QSPI, MICROWIRE, DSP interface, and microcontroller interfaces [112]. The utilization of DDS devices facilitates the development

of a more compact system for noncontact interrogation, and system calibration becomes more convenient, especially to configure the operating frequency of the resonant sensors. Furthermore, DDS devices are equipped with a power-down pin, enabling the activation of an external power-down mode to minimize overall power consumption. In the block diagram of Figure 4.4, CH0, CH1, and CH2 DDSs are deployed to generate gating, excitation, and reference signals, respectively. The system clock for these DDS devices is derived from an external 75 MHz crystal oscillator.

The gating signal $v_G(t)$, generated by CH0 with a period T_G, has been utilized to alternate between the excitation and detection phases. The switching of the electrical connections is achieved using an analog switch. The selected analog switch (MAX303), is a high-speed and high-precision single-pole double-through switch with two normally open (NO) and two normally closed (NC) poles. All the three parts of the switch offer a low on-resistance, measuring less than 35 Ω. Additionally, it boasts a low leakage current of approximately 250 pA and rapid switching characteristics, with turn-on time less than 150 ns and turn-off times less than 10 ns. Remarkably, this switch operates with a minimal power consumption of about 35 µW [113].

In the excitation phase, CH1 and the fully differential amplifier A_1 (AD8139), generate a sinusoidal signal $v_e(t)$ at an angular frequency ω_e in close proximity to the natural frequency $\omega_s = 2\pi f_s$ of the resonator, which acts as the driving signal for L_1. Consequently, due to the magnetic coupling between L_1 and L_2 a current is induced in the sensor coil, which puts the resonator into vibration given by the piezoelectric effect.

In the subsequent detection phase, the excitation signal $v_e(t)$ is deactivated, and the analog switch connects L_1 to the detection segment of the circuit. At this point, the resonator undergoes free decaying oscillations at an angular frequency ω_{dm}. Leveraging the piezoelectric effect, current is induced in coil L_2, leading to the development of a voltage signal $v_1(t)$. This voltage signal is then sensed across L_1 and amplified with gain G_3 by the amplifier A_3, giving the voltage $v_{O1}(t)$.

The amplifier A3 (OPA657), is a voltage-feedback operational amplifier. It stands out for its low-voltage noise JFET-input stage, ensuring a highly substantial dynamic range and elevated input impedance [114]. This characteristic guarantees that the current flowing through L_1 during the detection phase remains negligible.

In the condition where $\omega_s L_2 << 1/(\omega_s C_0)$, with C_0 the electrical static capacitance of the resonator, and considering an infinite input impedance for A_3 , the voltage $v_{O1}(t)$ can be approximated by the following expression:

$$v_{O1}(t) \approx G_3 M A_m e^{-t/\tau_m} cos(\omega_{dm} t + \theta_m), \tag{4.1}$$

where A_m and ϑ_m are the amplitude and phase parameters related to the electrical and mechanical parameters of the inductor L_1, L_2 and of the MEMS resonator as well as the initial conditions at the instant in which the excitation phase ends.

As explained in Chapter 3, the decay time τ_m of the exponential component of $v_{O1}(t)$ can be associated to the quality factor Q of the sensor resonator with the following expression:

$$\tau_m = \frac{2Q}{\omega_s}, \tag{4.2}$$

where ω_s is related to ω_{dm} with the following expression:

$$\omega_{dm} = \omega_s \sqrt{1 - \frac{1}{4Q^2}}, \tag{4.3}$$

In the condition with Q >> 1, ω_s can be directly approximated with ω_{dm}. For example, with $Q \approx 10^3$ the approximation $\omega_{dm} \approx \omega_s$ give relative deviation $(\omega_s - \omega_{dm})/\omega_s \approx 10^{-7}$.

The voltage $v_{O1}(t)$ undergoes multiplication through the use of the analog multiplier M1 (AD835) with the reference signal $v_R(t)=V_R cos(\omega_R t)$ which is generated by CH2 and amplified by A2 (AD8139).

Subsequently, the resulting signal is subjected to low-pass filtering and amplified with gain G_4 by A4 (AD820R) giving a signal with the following expression:

$$v_O(t) = G_4 M A_O e^{-t/\tau_m} cos(\omega_O t + \theta_m), \tag{4.4}$$

where the frequency of the demodulated signal $\omega_O = |\omega_{dm}-\omega_R|$ and the coefficient A_O take in accounts the amplitude of v_{O1}, v_R and the gain G_3 of A3. As explained in Section 3.2, and as evident from Equations (3.1) and (3.2), the mutual inductance M between coils L_1 and L_2, which is associated with the interrogation distance d, only acts as a scaling factor and has no impact on either the frequency or the decay time of the readout signal. For this reason, it is expected that ω_{dm} and consequently ω_O can be fundamentally read with independence of the interrogation distance. The signal $v_O(t)$ is then digitized by the multifunction instrument Digilent Analog Discovery 2, controlled by a LabView program which also manages, through an Arduino UNO board, the three DDSs. The LabView program also perform the signal digital elaboration to extract the SU resonant frequency. For this purpose the $v_O(t)$ autocorrelation function $R_{xx}(\tau)$ is computed. The theoretical expression of $R_{xx}(\tau)$ is the following:

$$R_{xx}(\tau) = \frac{1}{4}(MA_O)^2 e^{-|\tau|/\tau_m}\left[\tau_m cos(\omega_O \tau) + \frac{cos(\omega_O \tau + 2\theta_m + arctan(\omega_O \tau_m)}{\sqrt{1/\tau_m^2 + \omega_O^2}}\right]. \tag{4.5}$$

The characteristic behavior described by Equation (4.5) is illustrated in Figure 4.5.

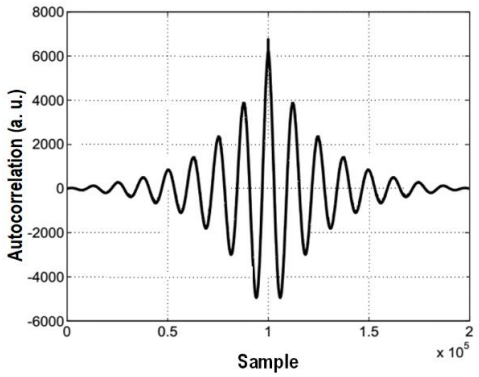

Figure 4.5 – Characteristic behaviour of the autocorrelation function R_{xx}.

It is evident from the representation of $R_{xx}(\tau)$ that it exhibits symmetrical properties with respect to τ, featuring two sinusoidal tails that decay exponentially with frequency ω_O and a decay time τ_m. As a result, a specialized peak detection algorithm can be employed to determine the periodicity of $R_{xx}(\tau)$ and accurately determine the value of ω_O. Furthermore, given the precise knowledge of the reference frequency ω_R, it becomes possible to derive $\omega_{dm} = \omega_R \pm \omega_O$ from this information. Additionally, assuming that the frequency variation $\Delta\omega_R$ of ω_R resulting from environmental factors, such as temperature, is significantly smaller compared to the frequency variation $\Delta\omega_O$ of ω_O, any observed changes in the frequency $\Delta\omega_{dm}$ of ω_{dm} can be attributed to the behavior of the resonator when it serves as the sensing element.

The time span over which the damped signal persists is roughly 5 times the decay time τ_m. Consequently, within this time window, the number of periods of $v_O(t)$ can be approximated as $N = 5\tau_m\omega_O/2\pi$. It is important to note that the value of N plays a pivotal role in the precise computation of $R_{xx}(\tau)$ for subsequent post-processing, and it also influences the selection of ω_R and consequently establishes the minimum required sampling frequency for $v_O(t)$.

The AlN TPoS MEMS resonator, as described in Section 4.2, has been configured for operation in the single-port mode at its radial contour mode. This configuration was achieved by connecting points A and B, with A formed by electrically shorting T1 and T2 as reported in Figure 4.6.

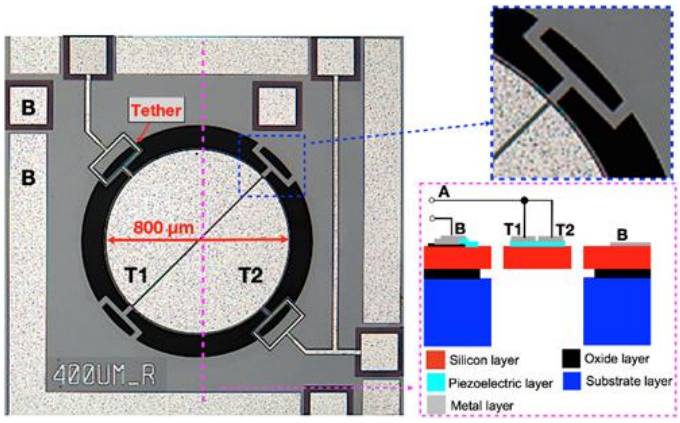

Figure 4.6 – Optical micrograph of the TPoS resonator with a detail of the tethers and the cross-sectional view of the process stack.

Through finite element analysis, the frequency of the resonating mode for this specific device has been predicted to be approximately 6.32 MHz. This resonant frequency was subsequently verified through electrical characterization, measuring the series resonant frequency where the electrical conductance G reaches its maximum, yielding f_s = 6.322 MHz. Around f_s, the parameters of the BVD circuit shown in Figure 4.4 has been derived from the fitting of G, and results R_m = 56.2 Ω, C_m = 365 fF, L_m = 1.79 mH, C_0 = 782 pF. The quality factor Q has been determined to be approximately 1200.

4.4 Experimental results

4.4.1 Experimental setup

To experimentally validate the proposed system and investigate the performance of the MEMS resonator under varying temperature conditions, we established a dedicated experimental setup, as shown in Figure 4.7a. This setup comprise a chamber with internal dimensions of 80×80×40 mm³, realized from a plastic box enclosed by polystyrene foam, ensuring efficient thermal insulation.

To control the temperature inside the chamber, a Peltier thermoelectric element (Kryotherm TGM 254-1.0-1.3) has been employed for both heating and cooling. The thermoelectric element has been placed at the base of the chamber, integrated with a heatsink and a fan assembly to dissipate heat in the external side of the chamber. In the internal side of the chamber another heatsinks has been placed to the thermoelectric surface to spread heat and cold. Controlled temperature regulation within the chamber has been achieved by driving the thermoelectric element with a programmable power supply (Agilent E3632A). To monitor the temperature with precision, a Pt1000 thermoresistor has been connected to a multimeter (Fluke 8840) and used as a reference temperature sensor.

The top side of the chamber, which features a removable lid, has been used to accommodate the interrogation coil, denoted as L_1, which is constituted by a 80 mm x 80 mm Flame Resistant 4 (FR4) substrate with 6-turn copper traces realizing a planar coil, as shown in the inset of Figure 4.7a. This coil electrical properties, measured with an

impedance analyzer (HP4194A) at a frequency of 6 MHz, give a series resistance R_1 = 5.5 Ω and a series inductance L_1 = 8.5 µH.

The resonator, which is connected to the sensor coil L_2, is positioned on the inner top side of the chamber, resulting in an interrogation distance of d = 7 mm from the interrogation coil. In Figure 4.7b it is shown the top side of the sensor unit with the sensor coil L_2 placed inside the temperature chamber. The sensor coil is milled from an FR4 substrate and has dimensions of 35 mm×35 mm. Its electrical resistance R_2 and inductance L_2, measured at 6 MHz, are 5 Ω and 8.2 µH, respectively. The TPoS MEMS shown in Figure 4.7c is instead placed on the opposite side of the FR4 substrate.

The Interrogation Unit (IU), consisting of a microcontroller, a dedicated printed circuit board, and the acquisition board, is shown in Figure 4.7d. Contactless operation advantageously allows locating the IU outside the chamber at nearly constant room temperature. Consequently, thermal effects on the interrogation circuitry, and in particular on the reference clock, are minimized.

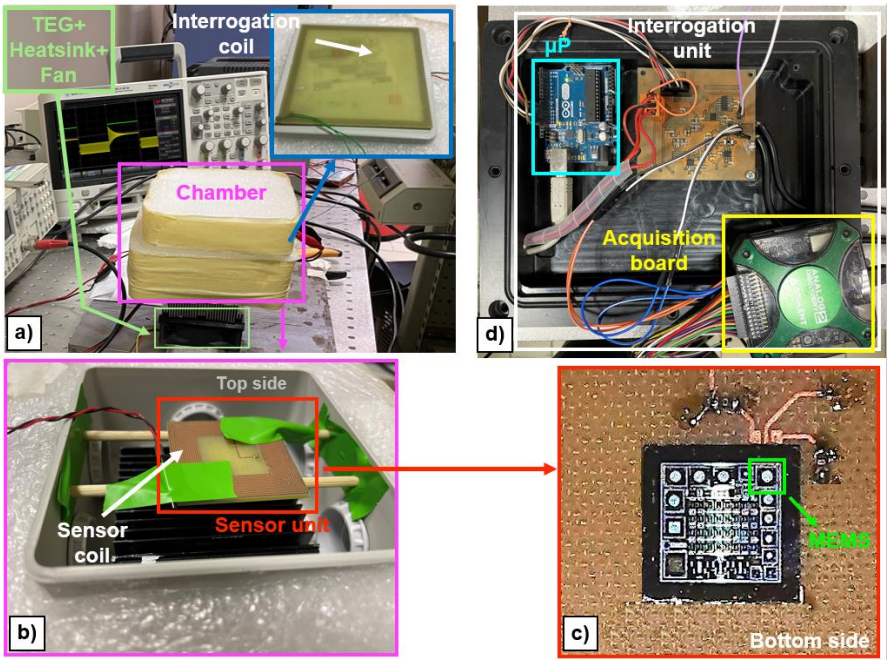

Figure 4.7 – Experimental setup employed to test the proposed system: (a) chamber and interrogation coil; (b) top and (c) bottom side views of the sensor unit; (d) interrogation unit.

In Figure 4.8, the acquired gating signal $v_G(t)$ and the damped free response of the resonator $v_{O1}(t)$ are reported with blue and orange curves, respectively. As introduced, $v_G(t)$ exhibits a low value during the excitation phase, while it rises to a higher level during the detection phase when the damped response of the resonator is detected. The realized chamber has been employed for conducting temperature measurements characterization of the TPoS MEMS resonator.

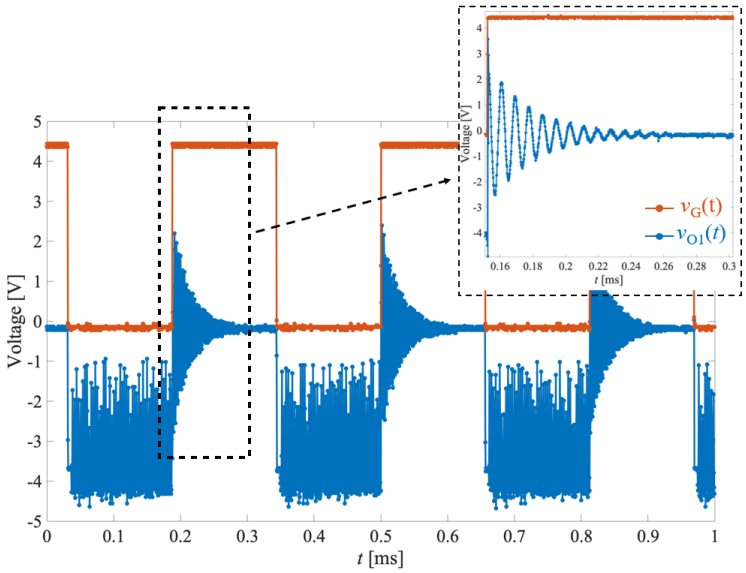

Figure 4.8 – Acquired gating signal $v_G(t)$ (orange curve) and the damped response of the resonator $v_{O1}(t)$ (blue curve) as a function of time.

4.4.2 Temperature characterization of AlN TPoS MEMS

To obtain a reference dataset to be used for the contactless interrogation techniques verification, the characterization of the dependence between the series resonant frequency f_s of the MEMS resonator and temperature has been performed establishing a wire-connection between the resonator and an impedance analyzer (HP4194A). The cabled MEMS resonator has been placed inside the developed temperature chamber used to systematically adjusted the temperature within the range of 20°C to 52°C, implementing increments of ΔT = 3°C.

The outcomes, presented in Figure 4.9, illustrate the acquired f_s values as a function of temperature T. The relationship between frequency and temperature exhibited a prevailing linearity, as evidenced by the best-fit line featuring a slope of 295.8 Hz/°C.

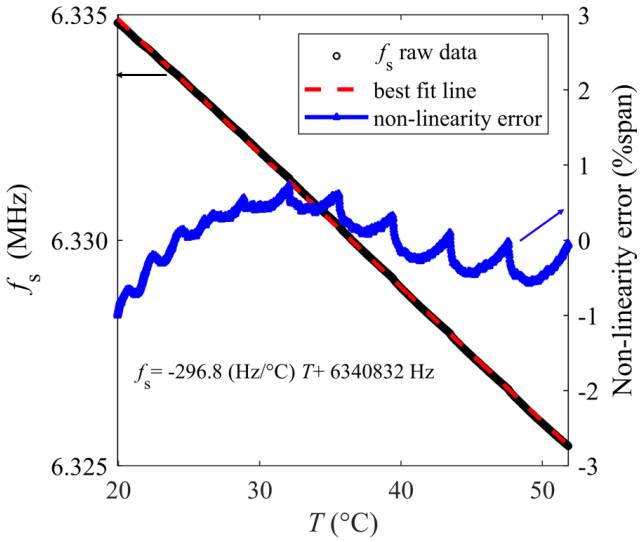

Figure 4.9 – Reference measurement of f_s (black dots) and non-linearity error (blue curve) as a function of temperature with respect to the fitting line (dotted line).

The observed non-linearity error remains confined within a range of +/-1% of the span of approximately 9.4 kHz across the considered temperature range. Has to be noted that the observed fluctuations in non-linearity error can be attributed to the specific temperature profile employed in the experimentation.

The Temperature Coefficient of Frequency (TCF) for the resonator can be expressed as TCF = $(1/f_{s0})(df_s/dT)$. In this equation, TCF represents the slope of the best-fit line, normalized to the frequency f_{s0} at the reference temperature T_0. By setting T_0 to 25°C, corresponding to f_{s0} = 6332475 Hz, we can derive an estimated TCF of -46.7 ppm/°C.

Regrettably, the available literature does not offer specific insights regarding the Temperature Coefficient of Frequency (TCF) for AlN-on-Si disk resonators operating in the radial contour mode. Therefore, a direct comparison with the measured value presented in this study is not feasible.

The TCF value of AlN-on-Si resonators is related to a multitude of factors. These include the distinctive properties of the electrode and piezoelectric film [115], the type of dopants and their concentration within the silicon device layer [116], the chosen vibration mode, and the intricate interplay of geometry and support structures. For contextual reference, a disk resonator produced through a similar fabrication process but transduced in the wine glass mode exhibited a TCF of -40 ppm/°C [117]. This value, though slightly lower than the one reported in our study, serves as an informative benchmark. It is noteworthy that the resonator under investigation is clamped at four specific points along the disk periphery, precisely corresponding to the anti-nodes of the radial contour mode. This clamping mechanism introduces stress at these specific points during temperature fluctuations, which is anticipated to result in a slight elevation in the TCF compared to structures that remain stress-free at the nodal regions.

4.4.3 Noncontact temperature reading of AlN TPoS MEMS

The noncontact reading of the temperature sensed by the AlN TPoS MEMS resonator has been tested to verify the proposed technique. For this purpose, the experimental setup described in Section 4.4.1 with the circuit described in Section 4.3 has been adopted.

Considering the parameter of the adopted MEMS resonator, the interrogation system has been set up with $f_e = \omega_e/2\pi = 6.322$ MHz and $f_R = \omega_R/2\pi = 6.433$ MHz. This configuration has been chosen to yield an expected f_O of approximately 111 kHz at the reference temperature of 20°C, given the condition $f_{dm} \approx f_e$. The adopted technique, involving resonator excitation and the subsequent measurement of its decaying response, does not rigidly demand that f_e exactly matches f_s. However, it should be considered that a good matching can enhance the signal-to-noise ratio (SNR) during the detection phase.

Expecting a decrease in the readout frequency with increasing temperature, as obtained in the characterization of Section 4.4.2, f_e has been set lower than f_s to maintain a consistent SNR throughout the entire temperature range under examination. The frequency f_O has been digitalized for the successive elaboration with at a sample rate of 1 MS/s.

The obtained f_{dm} values, obtained through the autocorrelation analysis in a temperature range of 20 - 60 °C, are plotted against temperature in Figure 4.10.

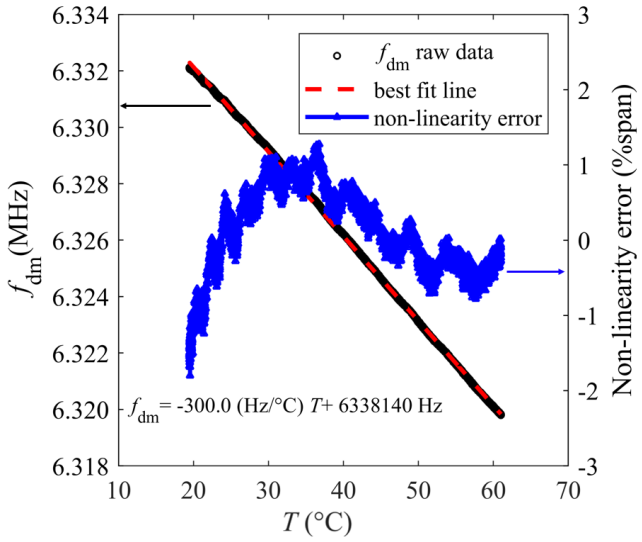

Figure 4.10 – Noncontact measurement of f_{dm} (black dots) and estimated non-linearity error (blue curve) as a function of temperature with respect to the fitting line (dotted line).

A linear relationship between f_{dm} data points and temperature has been obtained, characterized by a best-fit line slope of -300 Hz/°C. Normalizing this slope to f_{s0} allows the estimation of the TCF resulting 47.4 ppm/°C and thus showing excellent conformity with the reference value reported in Section 4.4.2. The non-linearity error results within a range of +/-2% of the span, which is approximately 12.3 kHz. In agreement with the characterization of Section 4.4.2, residual oscillations resulting from the applied temperature profile are visible in the data.

To investigate the impact of the interrogation distance, the distance d of the interrogation coil relative to the chamber top cover has been varied extending it up to d = 15 mm from the sensor coil. For comparative purposes, the value of f_{dm} has been determined using both the autocorrelation technique and by directly connecting the non-demodulated detected signal v_{O1} to a frequency counter (Philips PM6680).

For an appropriate frequency counter measurements, the counter has been set with a gate time of 20 µs and a 10 µs delay from the onset of the detection phase to mitigate ringing

effects, and then averaged the results over 100 samples. We aligned the setting of the proposed autocorrelation system to a similar configuration for consistency in the comparison.

Figure 4.11 displays the results obtained as a function of the varying distance *d* for both the autocorrelation and counter measurements, in addition to the ambient room temperature that has been measured during the characterization. The error bars within the graph represent measurement uncertainties, calculated at one standard deviation based on experimental data. It can be observed that the standard deviation of data acquired through the frequency counter measurements exhibits significant variability, with values increasing up to 700 Hz as the distance *d* extends. In contrast, the standard deviation remains relatively consistent, around 118 Hz, for the autocorrelation measurements. This behavior can be attributed to the fixed gate time and the increasing distance, which adversely affect the signal-to-noise ratio (SNR) of the decaying $v_{O1}(t)$ and consequently impact the reliability of the frequency counter measurements. Conversely, the proposed approach, built on autocorrelation analysis and its associated post-processing, effectively compensates for the declining SNR, resulting in superior performance for f_{dm} measurement.

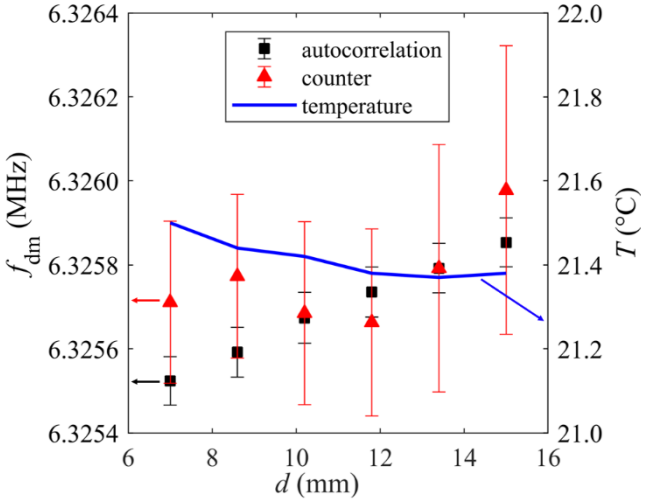

Figure 4.11 – Temperature (blue curve) and noncontact measurement of f_{dm} by means of counter (triangles) and autocorrelation technique (squares) as a function of imposed distance.

The frequencies reported in Figure 4.11 have been adjusted to account for temperature variations, employing the TCF as determined earlier. Over the range of distances considered, the most significant frequency variation is approximately 300 Hz, representing less than 60 ppm with respect to the frequency recorded at d = 7 mm. These results align with previously reported findings [108], confirming the expected insensitivity of the readout frequency to alterations in the interrogation distance. The remaining linear correlation with distance d can be attributed to the influence of parasitic capacitance originating from the circuit board and electronic components connected in parallel to interrogation coil L_1. Electronic techniques and circuits have been proposed to address and compensate this effect as explained in Section 3.2 [51].

Chapter 5

Noncontact interrogation of a flexible passive sensor patch with capacitive sensing element for human body temperature measurement

In this chapter a novel approach for human skin temperature measurement based on a passive flexible patch combining contact sensing with contactless interrogation is presented. Specifically, the proposed approach extends the contactless interrogation technique described in Chapter 3 to a flexible sensor patch attached onto a curved surface and achieves contactless interrogation independently of the curvature radius of the flexible patch. The sensor patch is based on a RLC resonant circuit, featuring an inductive copper coil for magnetic coupling, a ceramic capacitor serving as the temperature sensing element, and an additional series inductor. The temperature-induced variations in the sensor capacitance influence the resonant frequency of the RLC circuit. Notably, the introduction of an additional inductor mitigates the dependency of the resonant frequency on the patch bending. With a curvature radius of up to 73 mm, the maximum relative resonant frequency variation has been significantly reduced, decreasing from 812 ppm to merely 7.5 ppm. For contactless interrogation, the sensor has been interrogated using a time-gated technique involving an external readout coil electromagnetically coupled to the patch coil. Experimental testing has been conducted within the temperature range of 32 - 46 °C. The system exhibited a remarkable sensitivity of 619.8 Hz/°C and an impressive resolution of 0.06 °C. This innovative approach holds promise for accurate and non-invasive human skin temperature measurements, offering enhanced precision and reliability in various practical applications.

5.1 Flexible passive sensor patch for human body temperature measurement

Monitoring body temperature is an essential practice in the realm of healthcare, playing a pivotal role in the early detection and diagnosis of various health conditions and diseases [118]. It serves as a valuable indicator of an individual physiological health and can signal deviations from the norm that might otherwise go unnoticed. In the context of monitoring body temperature, two primary approaches are widely employed: contact and noncontact methods.

Contact-based temperature measurement methods are renowned for their precision and reliability. They involve direct skin contact with the measuring device, which can be a thermometer or a sensor. However, these methods often require meticulous disinfection procedures to prevent cross-contamination and may be time-consuming, which can be impractical in certain scenarios [119].

In contrast, noncontact approaches offer the advantage of rapid temperature measurements without direct skin contact. Devices using noncontact methods, such as infrared thermometers, have become popular, particularly in clinical environments. Nevertheless, these methods can be less reliable due to factors such as the transmission coefficient of the interface medium and the distance of the sensor from the skin, making them less suitable for continuous monitoring applications [119,120].

Continuous monitoring of body temperature is especially valuable in scenarios like home and hospitals, where regular temperature assessments are required for patient care and health management. In such cases, there is a growing demand for lightweight, unobtrusive, and battery-less contact sensors. These sensors are designed to be comfortable for extended wear and provide real-time temperature data.

To meet this demand, the use of flexible wearable sensors has gained traction as an effective approach to monitor human body temperature. These sensors can conform to the contours of the body, ensuring a snug and comfortable fit. Moreover, NFC (Near Field Communication) based temperature sensors have emerged as a promising solution for

biomedical applications, enabling the development of battery-less skin patches that are both convenient and user-friendly [121]. These sensors are equipped with active electronic integrated circuits, typically including a microcontroller and one or more connected sensors. However, these components rely on external reader devices for energization and data transmission through digital communication protocols.

As an alternative, solutions based on passive resonant sensors that can be suitably employed with flexible wearable sensors have been demonstrated [77,122]. These sensors can enhance the possibility to obtain low-cost or disposable device ensuring anyway accurate and consistent temperature measurements.

The proposed sensor patch is designed to adhere comfortably to the skin, typically the arm of an individual, and be covered by clothing, owing to its utilization through a noncontact interrogation method by a nearby interrogation unit.

Nonetheless, it is important to note that a common challenge associated with flexible sensors is their susceptibility to performance variations resulting from the bending of the substrate housing the sensing element [123,124]. This bending can introduce inaccuracies in temperature readings and necessitates the application of specific techniques and dedicated solutions to mitigate or eliminate this undesirable phenomenon [125].

Noncontact measurement techniques have emerged as practical solutions in scenarios where wired or battery-powered alternatives are either unfeasible or invasive [53,126,127]. In particular, passive resonant sensors and electromagnetic interrogation techniques have been effectively validated for various sensor types, including quartz crystal resonators (QCR) [51], resonant piezo layer (RPL) sensors [62], MEMS resonators [63], and LC resonant sensors [65,126]. These sensors can be interrogated using both frequency-domain and time-domain approaches [51].

Frequency-domain techniques involve the measurement of parameters such as impedance, reflection coefficients, or specific transfer functions. These kind of measurements simultaneously excite and sense the resonator [49,66,67]. On the other hand, time-domain techniques, as proposed in the study of this chapter, make use of the transient free response

of the resonator by separating the excitation and detection phases in time [68]. The distinct advantage of time-domain techniques is the possibility to implements the measurement without the use of complex bench instrumentation.

As reported in Chapter 3, with appropriate precautions, both frequency-domain and time-domain techniques have demonstrated the ability to maintain consistent sensing accuracy independently of the reading distance. This attribute underscores the reliability and robustness of these methods, further solidifying their potential applications in sensor technology and biomedical applications.

5.2 Developed sensor patch and system description

The sensor patch contactless interrogation proposed in this chapter exploits a contactless interrogation technique based on magnetic coupling between a passive sensor unit (SU) and an electronic interrogation unit (IU) extending the techniques explained in Chapter 3. The SU incorporates an RLC resonant circuit and features a flexible patch equipped with an inductive copper coil for magnetic coupling. Furthermore, it includes a ceramic capacitor as the temperature sensing element and an additional inductor to maintain the resonant frequency of the SU regardless of the inevitable bending caused by the body conformation and movements. The proposed sensor is instead expected to be positioned on body parts, e.g. arm, neck or temple, with a curvature radius typically in the order of 70 mm.

The IU is equipped with a primary coil and front-end electronics, designed for time-gated contactless excitation and read-out. This method not only guarantees high-accuracy results but also opens to the implementation of a fully integrated and compact system. Significantly, it eliminates the need for sophisticated bench instrumentation to read the resonant frequency, streamlining the system and enhancing its applicability across various filed [70,128].

Figure 5.1a illustrates a typical application scenario for the proposed flexible patch, while Figure 5.1b shows an example of application of the patch on the arm skin of a human subject.

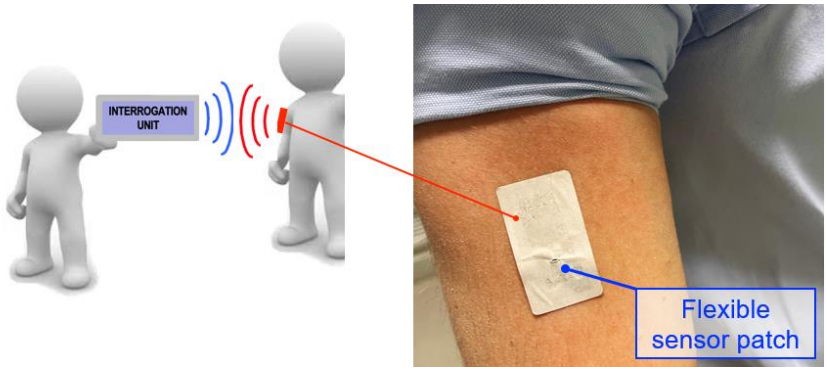

(**a**) (**b**)

Figure 5.1 – (a) Typical application scenario for the temperature sensor patch; (b) example of the sensor patch stuck on the arm skin of a human subject.

5.2.1 Sensor unit

Figure 5.2a shows the bottom view of the developed proof-of-concept prototype patch. This patch consists of an adhesive paper substrate measuring 43 mm × 23 mm, featuring a planar sensor coil pattern of 10 turns of traces etched onto a copper foil adhered to the paper substrate. The planar coil, characterized by its electrical resistance R_2 and inductance L_2, is in series with an inductor characterized by parameters R_3 and L_3. Additionally, the patch incorporates a ceramic capacitor, denoted as C_s, which is chosen as the temperature sensing element due to its temperature coefficient of capacitance (TCC). The resulting equivalent RLC circuit is shown in Figure 5.2b.

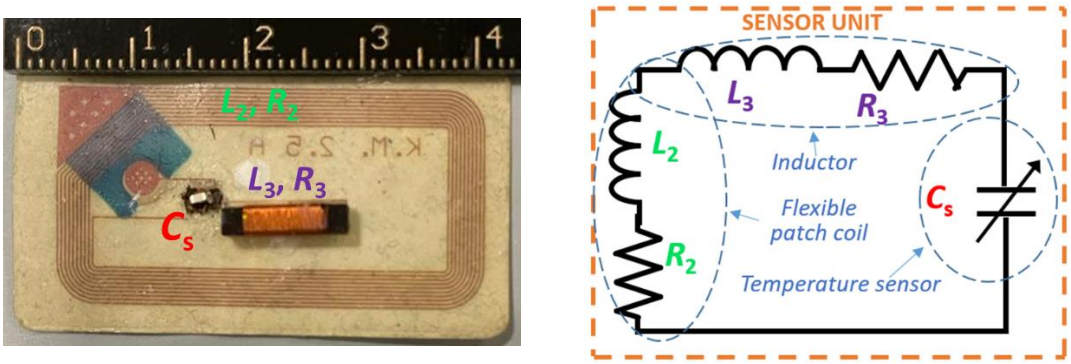

(**a**) (**b**)

Figure 5.2 – (a) Bottom view of the developed sensor patch; (b) SU equivalent RLC circuit.

Both L_3 and C_s are readily available lightweight components with dimensions on the millimeter scale, thoughtfully selected to preserve the patch flexibility. To optimize performance and comfort, the size, shape, and positioning of these components can be adjust with regard to the expected primary bending direction of the patch. The capacitor C_s is encapsulated in epoxy resin, which effectively shields it from humidity-induced capacitance fluctuations. To enable temperature measurements through skin contact, additional passivation of the soldering joints is needed to prevent any degradation of sensing performance due to sweat or moisture.

The complete patch implements the sensor unit (SU) of the proposed contactless interrogation system. The primary coil L_1 of the IU establishes magnetic coupling with the SU coil L_2 through mutual inductance M, which depends on the separation distance d between the coils.

5.2.2 Interrogation unit

The developed IU, which block diagram is shown in Figure 5.3, generate the sinusoidal signals to excite the SU, and demodulate the signal received back from the SU. The proposed approach require three separated signal to perform the excitation and detection which are generated by means of a DDS (Direct Digital Synthesis) chip with three independent channels, namely CH1, CH2 and CH3.

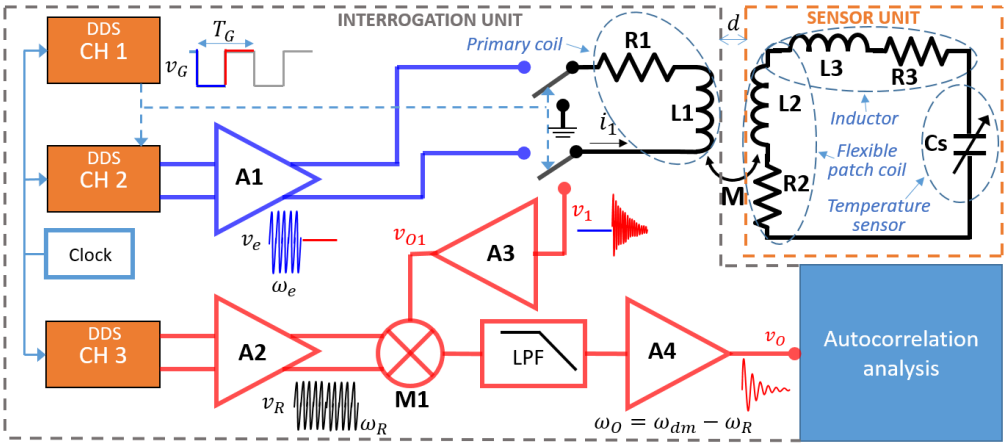

Figure 5.3 – Block diagram of the proposed contactless interrogation system.

The timing of the excitation and detection phases is synchronized by the gating signal $v_G(t)$, which is produced by CH1 and has a period of T_G. During the excitation phase, a sinusoidal signal $v_e(t)$ at angular frequency ω_e is generated by CH2 and then amplified by A1.

By selecting an angular frequency ω_e close to $\omega_s = 2\pi f_s$, the current induced in coil L_2 through the magnetic coupling with L_1 drives by $v_e(t)$, causes the RLC circuit to resonate at its natural resonant frequency:

$$f_s = \frac{1}{2\pi\sqrt{(L_2 + L_3)C_s}}, \tag{5.1}$$

This resonance is characterized by a quality factor Q, which can be determined as follows:

$$Q = \frac{1}{R_2 + R_3}\sqrt{\frac{L_2 + L_3}{C_s}}. \tag{5.2}$$

Considering the components utilized in the proposed proof-of-concept prototype, the planar coil is the element most affected by the bending or deformation of the patch. Nevertheless, under the assumption that $L_3 >> L_2$ and $R_3 >> R_2$, both the f_s and Q are not significantly influenced by the electrical characteristics of the planar coil, and can be approximately calculated as:

$$f_s \approx \frac{1}{2\pi\sqrt{L_3 C_s}}, \tag{5.3}$$

$$Q = \frac{1}{R_3}\sqrt{\frac{L_3}{C_s}}. \tag{5.4}$$

This means that the bending of the patch has no significant impact on these parameters.

Ended the excitation phase, the excitation signal $v_e(t)$ is switched off and starts the detection phase. During this phase, the resonator undergoes free decaying oscillations at angular

frequency ω_{dm}, which is related to the RLC circuit natural resonant frequency ω_s with the following expression:

$$\omega_{\mathrm{dm}} = \omega_s \sqrt{1 - \frac{1}{4Q^2}}. \tag{5.5}$$

It should be noted that for Q ≈ 100, a relative deviation of $(\omega_s\text{-}\omega_{dm})/\omega_s \approx 10^{-5}$ is observed, which allows considering $\omega_{dm} \approx \omega_s$. During the free decaying oscillations, a current flows through L_2, and as a result of magnetic coupling, induces the voltage $v_1(t)$ across L_1. This signal, is then amplified by A3, yielding the voltage $v_{O1}(t)$. Subsequently, $v_{O1}(t)$ is subjected to down-mixing using the analog multiplier M1, where it is combined with the reference signal $v_R(t) = V_R cos(\omega_R t)$, generated by CH3 and amplified by A2.

The obtained signal is low-pass filtered and subsequently amplified by A4, resulting in the generation of a sinusoidal damped signal, $v_O(t)$, characterized by an angular frequency $\omega_O = |\omega_{dm}\text{-}\omega_R|$, and a decay time $\tau_m = 2Q/\omega_s$. As confirmed in previous studies [68], both ω_O and τ_m are not influenced by variations in the interrogation distance *d*.

To calculate ω_O, the signal $v_O(t)$ undergoes digitization, and through a LabView software its autocorrelation function $R_{xx}(\tau)$ is computed. The expression for $R_{xx}(\tau)$ results:

$$R_{\mathrm{xx}}(\tau) = \frac{1}{4}(MA_{\mathrm{O}})^2 e^{-|\tau|/\tau_{\mathrm{m}}} \left[\tau_{\mathrm{m}} cos(\omega_{\mathrm{o}}\tau) + \frac{cos(\omega_{\mathrm{o}}\tau + 2\theta_{\mathrm{m}} + \arctan(\omega_{\mathrm{o}}\tau_{\mathrm{m}}))}{\sqrt{1/\tau_{\mathrm{m}}^2 + \omega_{\mathrm{o}}^2}}\right]. \tag{5.6}$$

As explained in Section 4.3, $R_{xx}(\tau)$ exhibits symmetrical properties with respect to τ, featuring two sinusoidal tails that decay exponentially with frequency ω_O and a decay time τ_m. Given the precise knowledge of the reference frequency ω_R, it is thus possible to determine $\omega_{dm} = \omega_R \pm \omega_O$. Additionally, assuming that the reference frequency ω_R is constant and stable the variation $\Delta\omega_{dm}$ of ω_{dm} can be attributed to the frequency variation of the SU resonant RLC circuit.

The fabricated SU has been experimentally characterized using an impedance analyzer (HP4194A). At room temperature, the resonant frequency f_s was determined to be 1.634 MHz. At this frequency, SU coil presents initial values of R_2 = 5.53 Ω and L_2 = 5.07 µH when not subjected to bending. The additional series inductor with dimensions of 10 mm × 2.5 mm, has R_3 = 196.85 Ω and L_3 = 545.25 µH, measured at f_s. The capacitive temperature sensing element is a ceramic capacitor with a capacitance C_s of 17.02 pF measured at 20 °C.

The adopted IU coil, shown in Figure 5.4, consist of a 6-turn planar coil obtained from an 80 mm × 80 mm standard FR4 (flame retardant) substrate. It is characterized by R_1 = 7.18 Ω and L_1 = 8.94 µH.

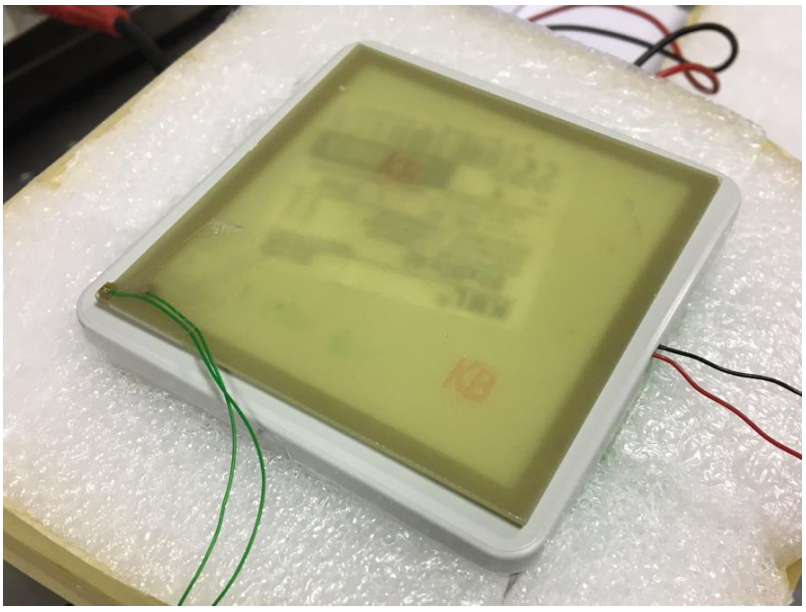

Figure 5.4 – Adopted IU coil obtained from an 80 mm × 80 mm standard FR4 substrate.

5.3 Experimental results

5.3.1 Patch bending effects analysis

The effects of various bending conditions on the sensor coil within the patch have been investigated. The analysis involved measuring the corresponding changes in the coil inductance L_2 and resistance R_2. Figure 5.5a displays the dedicated setup purposely employed for the controlled bending of the patch. The patch has been appropriately secured to a flexible FR4 support. To enable precise control over the bending process, a C-shaped fixture with an aperture C = 86 mm has been mounted on a micrometric position controller, allowing the flexible support to be grasped near its outer edges.

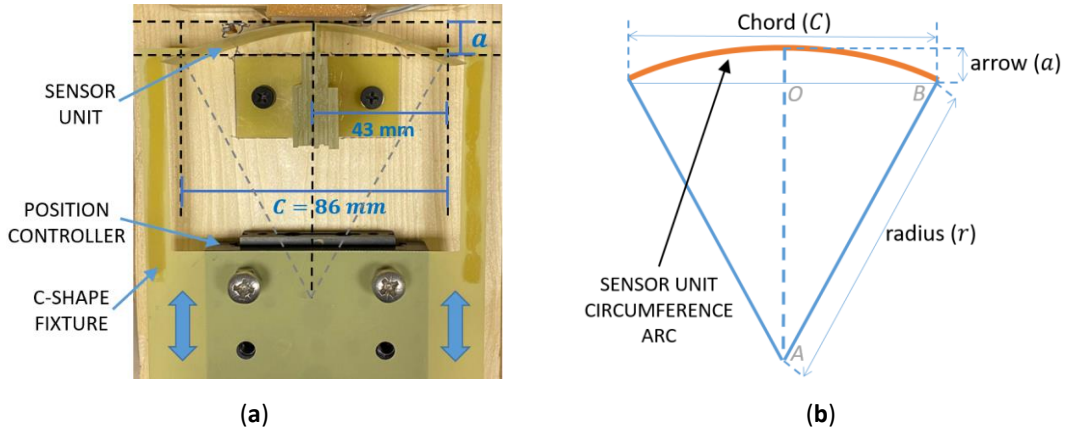

Figure 5.5 – (a) Developed setup composed of a position controller with micrometric resolution that allows to bend the flexible support for the SU patch to test the effect on the resonant frequency; (b) schematic representation of the flexible support circumference arc.

The micrometric position controller forces a displacement a of the outer edges, thus a bending of the patch. Referring to Figure 5.5b, under the assumption that the deformation can be approximated as an arc of a circumference, the curvature radius r can be calculated by applying the Pythagorean theorem to triangle AOB:

$$r = \frac{C^2}{8a} + \frac{a}{2}. \tag{5.7}$$

Figure 5.6 presents the changes in L_2 and R_2 with respect to the curvature radius r from 73 to 925 mm. These measurements has been conducted at the SU resonant frequency f_s = 1.634 MHz. As expected, the inductance of the patch monotonically rises for increasing values of curvature radius [123–125]. According to Equation (5.1), variations in L_2 correspondingly influence f_s.

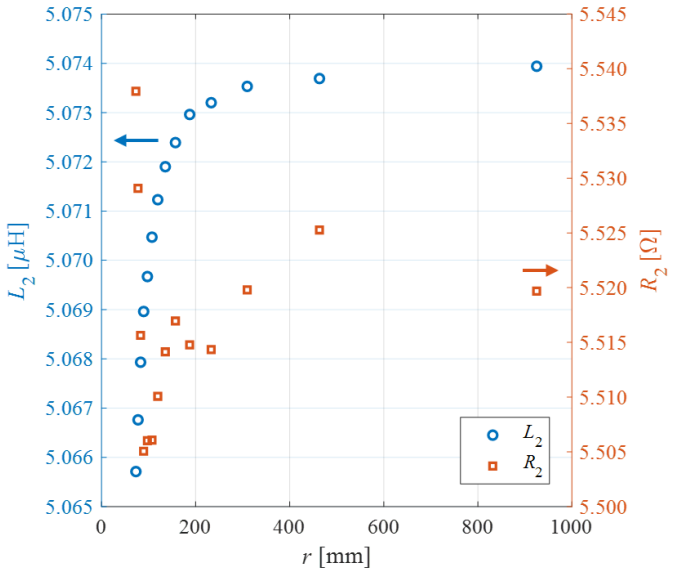

Figure 5.6 – Measurement results of the inductance L_2 and resistance R_2 of the SU coil as function of the curvature radius r.

Considering the case without the added inductor, i.e. L_3 = 0, the maximum relative variation in f_s due to bending, in comparison to f_{s0} when $a = 0$, results $\Delta f_s/f_{s0}$ = 812 ppm. Conversely, when L_3 is integrated in the sensor unit in series with L_2, the maximum relative change in f_s significantly decreases to $\Delta f_s/f_{s0}$ = 7.5 ppm. In summary, the inclusion of the supplementary inductance drastically diminishes the relative frequency variation caused by bending, achieving a reduction of two orders of magnitude.

According to Equation (4.1), and assuming a = 0, the theoretical values of f_s and Q, with the added inductor L_3, results f_{s0} = 1.644 MHz and Q_0 = 28.

5.3.2 Temperature characterization

In order to evaluate the sensor temperature detection capability, a customized experimental setup has been devised, as shown in Figure 5.7a. An enclosed chamber with internal dimensions of (80 × 80 × 40) mm^3 has been assembled using a plastic container enveloped by polystyrene foam to ensure thermal insulation. To control the temperature T within the chamber, a Peltier thermoelectric element has been positioned at the bottom of the chamber and used to electrically regulate the temperature of the inner volume.

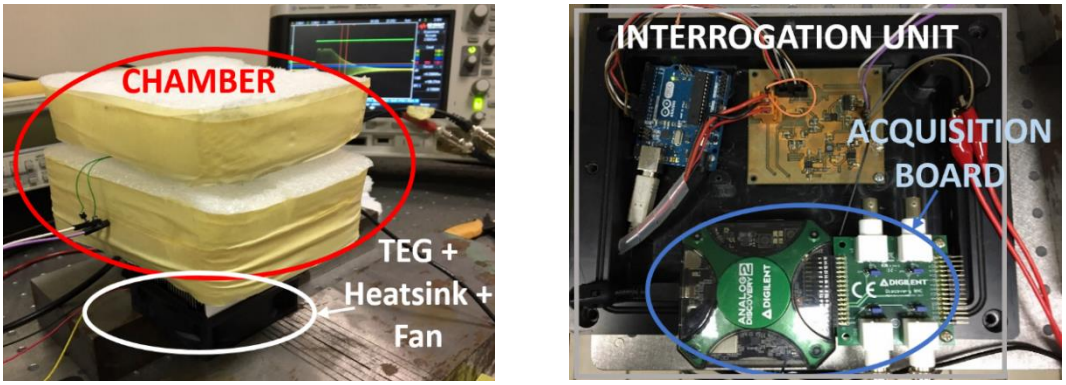

(**a**) (**b**)

Figure 5.7 – (a) Plastic box test chamber surrounded by polystyrene foam for thermal insulation equipped with a Peltier thermoelectric element at the bottom to set the temperature of the inner volume; (b) interrogation unit and acquisition board used to test the proposed system.

The sensor patch has been placed on the top of the chamber in adherence to the cover. Additionally, a Pt1000 temperature sensor, monitored by a multimeter (Fluke 8840), has been placed in thermal contact with the SU, serving as the reference temperature sensor. The primary coil L_1 of the IU was located external to the chamber cover, at a fixed distance d = 2 mm from the SU patch.

The contactless reading of the patch sensor has been tested over a temperature range spanning from 32 °C to 46 °C. The IU constituted by an acquisition board (Digilent Analog Discovery 2), a dedicated electronic circuit ad an Arduino Uno board, as shown in Figure 5.7a, has been configured to excite the resonator close to f_s with $f_e = \omega_e/2\pi$ = 1.634 MHz and with $f_R = \omega_R/2\pi$ = 1.734 MHz. Figure 5.8 shows the measured gating signal $v_G(t)$ and the output signal $v_O(t)$ sampled at 2 MS/s.

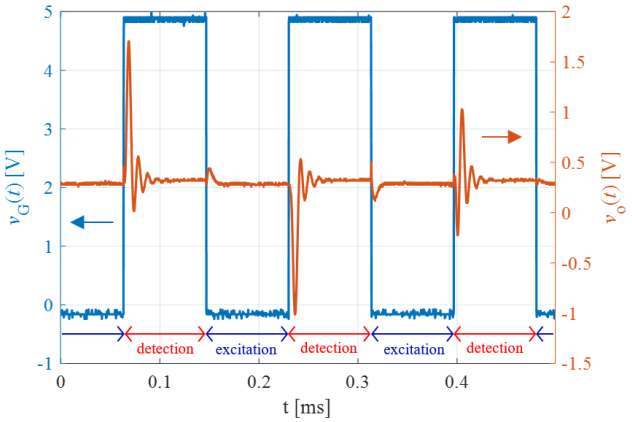

Figure 5.8 – Acquired gating signal $v_G(t)$ (blue curve) and demodulated free decaying response $v_O(t)$ of the resonator (orange curve) as a function of time.

As explained in Section 5.2.2, the frequency $f_{dm} = \omega_{dm}/2\pi$ is derived via the autocorrelation function through a dedicated LabView software that also control the signal generation and the data acquisition.

In Figure 5.9 are shown the recorded values of f_{dm} measured as a function of temperature T inside the chamber. The experimental data has been fitted with a best-fit line, revealing a temperature sensitivity S of -619.8 Hz/°C. The non-linearity error results within ±1.48 % of the span of about 8.3 kHz for the explored temperature range.

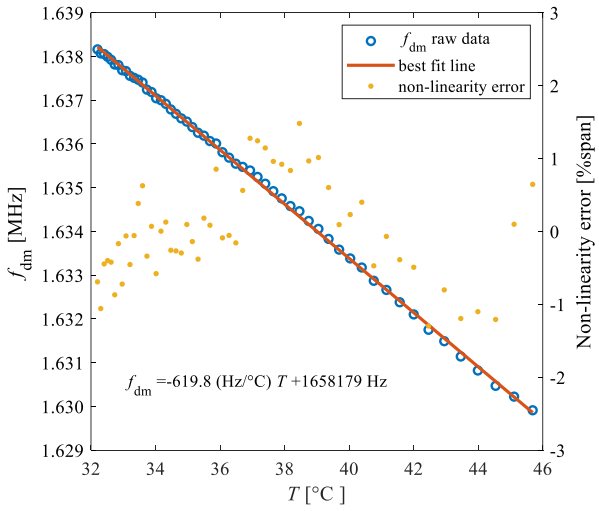

Figure 5.9 – Contactless measurement results of the SU frequency f_{dm} (blue circles), best fit line (orange line) and non-linearity error (yellow dots) as a function of temperature.

At the constant temperature of 28 °C, 150 repeated measurements of the frequency f_{dm} have been performed obtaining the results reported in Figure 5.10a. The distribution histogram shown in Figure 5.10b leads to a standard deviation for f_{dm} of σ_{fdm} = 37 Hz. Considering the obtained sensitivity S, the consequent standard deviation for the temperature can be calculated as $\sigma_T = \sigma_{fdm}/|S|$ and results equal to 0.06°C. This value can be considered the equivalent temperature resolution at one standard deviation. Notably, this level of precision aligns with the requirements for body temperature measurement applications [119,129,130]

Taking in account the maximum variation Δf_s induced by changes in L_2 caused by the patch bending, for a minimum curvature radius of 73 mm, the corresponding maximum error in temperature reading can be calculated as $\Delta f_s/S$ = 0.019 °C. This error results lower than the achieved resolution.

Considering that the frequency f_s is mainly influenced by L_3, and as L_3 remains unaffected by bending, temperature measurements obtained at different curvature radii yield comparable results.

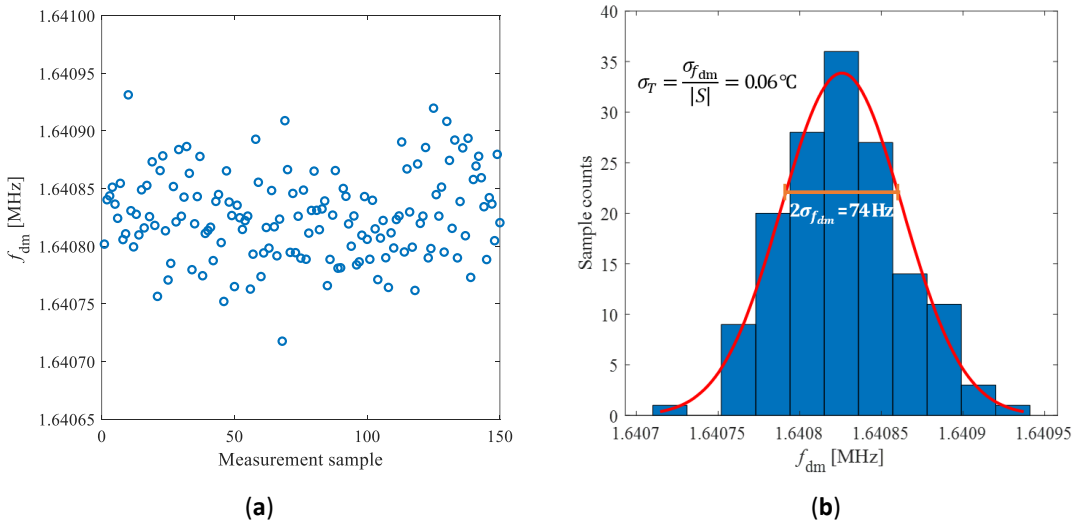

Figure 5.10 – (a) Results of 150 repeated measurements of f_{dm} at a constant temperature of 28 °C; (b) distribution histogram of the 150 measurement results with bins of 214 Hz.

The system stability over time has been verified by placing the sensor patch inside the testing chamber shown in Figure 5.7a, maintaining a constant temperature of approximately 36 °C. During this period, the reference temperature was monitored using a Pt1000 sensor, and the patch resonant frequency has been recorded every minute for a total duration of 4 hours.

In Figure 5.11a are presented the reference temperature T and the measured f_{dm} as a function of time, while Figure 5.11b shows the values of f_{dm} as a function of T.

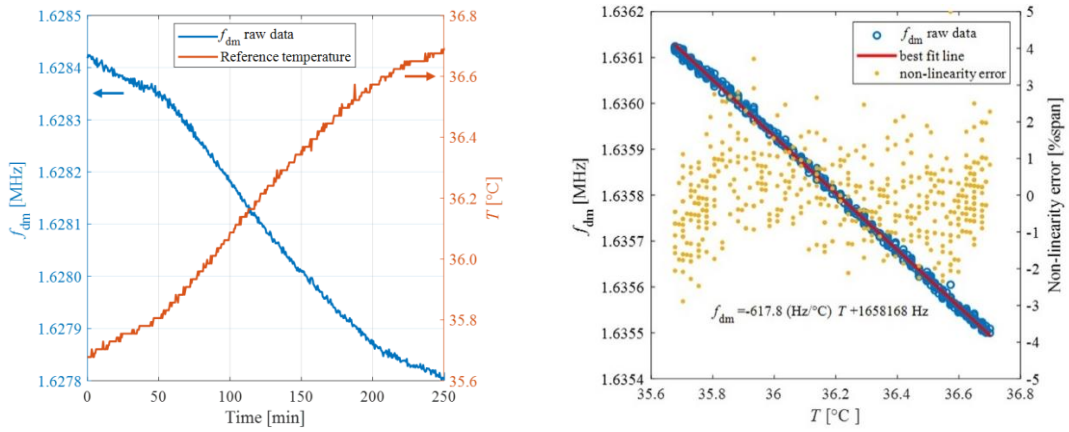

(**a**) (**b**)

Figure 5.11 – (a) Reference temperature *T* measured with a Pt1000 sensor (orange curve) and f_{dm} (blue curve) as a function of time; (b) f_{dm} (blue circles), best fit line (red line) and non-linearity error (yellow dots) as a function of *T* measured versus time.

The obtained experimental data has been analyzed to determine the temperature sensitivity S, which result from the best-fit line equal to 617.8 Hz/°C. This value aligns closely with the sensitivity established during the characterization in the temperature range from 32 °C to 46 °C. This confirmed relationship between the resonant frequency and temperature proof the absence of any notable drift in the sensor output over an extended time frame spanning of several hours.

Chapter 6

Noncontact interrogation of inductive sensors for conductive target detection

In the scenario of proximate sensing, in this chapter the contactless interrogation of an inductive sensor for conductive target detection is presented. The considered inductive sensor comprises a solenoidal coil of copper wire wrapped around a plastic pipe and connected to a series capacitor to form a LC circuit resonating at a specific resonant frequency. A conductive target placed at different positions inside the pipe modifies the inductance of the coil and in turn the resonant frequency. An external interrogation coil electromagnetically coupled to the inductive sensor allows reading the resonant frequency through a contactless interrogation technique. The proposed approach has been tested by varying both the position of a lead sphere adopted as the target and the interrogation distance between the inductive sensor and the interrogation coil. The obtained results shown the capacity of the proposed technique to detect the adopted target with a minimal residual dependency on interrogation distance, validating the potential of contactless interrogation in inductive sensors for enhanced conductive target detection.

6.1 Inductive sensors

Inductive sensors are a fundamental technology in the field of sensor engineering, leveraging the principles of electromagnetism to detect and measure various objects. These sensors are characterized by their ability to interact with their environment through electromagnetic fields, without requiring physical contact. Central to their design is a coil, typically energized with alternating current, which generates a magnetic field. The field behaviour and interaction with nearby objects form the basis of the sensor operation [131].

The key to these sensors lies in their behaviour due to the presence of conductive or magnetic materials. When such materials are presents in the sensor magnetic field, they induce changes in the field dynamics, leading to measurable alterations in the sensor impedance. This capability enables inductive sensors to detect the presence, absence, or position of objects, making them highly valuable in a range of applications, from industrial automation to safety systems [132,133].

These sensors are designed with various geometries and specifications to suit different applications, making them versatile tools in modern technology. The balance between their design and operational environment determines their effectiveness, sensitivity, and range, highlighting their adaptability to diverse needs.

6.1.1 Inductive sensors for conductive targets detection

Inductive sensors are often used in the specialized field of detecting conductive target. These sensors function based on their ability to discern changes in magnetic fields when a conductive or magnetic material enters their influence zone inducing alterations in the magnetic field, and consequently altering the sensors impedance [134]. In the case of non-magnetic materials, these phenomena manifest predominantly as eddy currents. These currents, induced by the primary magnetic field, create their own magnetic field that opposes and diminishes the induction field, as shown in Figure 6.1.

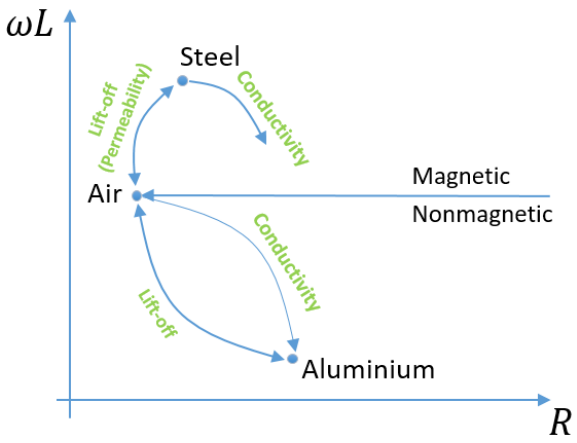

Figure 6.1 – Inductive sensor impedance $Z = R + j\omega L$ response to the presence of magnetic and nonmagnetic material in the generated magnetic field.

Eddy currents are fundamental in inductive sensor technology, serving as the primary mechanism for detecting and controlling the presence of conductive targets [135].

In scenarios involving highly conductive materials at high operating frequencies, inductive sensors functions as eddy current sensors. In this case, the field penetration into the material is minimal, and the associated losses are negligible. The more complex cases involve materials that are both electrically conductive and magnetic. Here, the physical basis of detection do not solely depend on the geometrical path of the magnetic field lines or the sensor design. Instead, it involves a detailed understanding of how eddy currents distribute within the material. This distribution, and consequently, the sensor impedance, are influenced by several factors: the sensor geometry, the distance between the sensor and the specimen (referred to as lift-off), operating frequency, and the specimen electrical conductivity, magnetic permeability, shape, and any inherent discontinuities or heterogeneity [131].

6.1.2 Inductive sensors for particle detection

Moving beyond the detection of large conductive targets, inductive sensors also find their application in the field of particle detection. This application showcases the sensor versatility in detecting not just the presence of large objects but also the more subtle

presence of particles [136]. The principle remains rooted in electromagnetic induction, but the focus shifts to the detection of changes in the electromagnetic field caused by particles [132,134].

In industrial settings, this capability is particularly valuable for monitoring the wear and tear of machinery. Metallic particles in lubricants or other fluids, for instance, can be indicative of machinery components undergoing degradation. By detecting these particles, inductive sensors play a crucial role in predictive maintenance, allowing for timely intervention before more significant damage occurs [133].

Moreover, in environments where contamination control is critical, such as in pharmaceuticals or food processing, the ability of inductive sensors to detect small metallic particles ensures the integrity of products. This detection is essential for adhering to stringent quality and safety standards.

The sensitivity of the sensor to different particle sizes, compositions, and the environment in which it operates are governed by the sensor geometry, the frequency of the electromagnetic field, and the nature of the particles themselves.

6.2 Developed inductive sensor with contactless interrogation

As introduced, inductive sensors (IS) are widely used to detect conductive targets, such as for example wear debris in lubrication oil [136]. The detection relies on the variation of the IS inductance due to the interaction between the magnetic field produced by the sensor and the conductive target [132]. Conventional techniques exploit cabled solutions with the drawback of being unfeasible in enclosed or hermetic environments where cabling could be an obtrusive option [89]. This chapter investigates the possibility of applying a contactless interrogation technique to an IS for conductive target detection by exploiting an external interrogation coil (IC). The proposed approach has been validated adopting a millimeter-size lead sphere as the conductive target.

6.2.1 System description

Figure 6.2 shows the block diagram of the proposed readout system, where R_1 and L_1 model the IC, R_2 and L_2 the IS coil, and M is the mutual inductance dependent on the interrogation distance d between the coils.

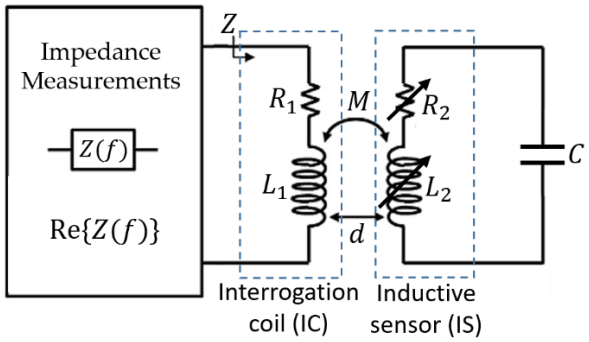

Figure 6.2 – Block diagram of the readout system based on impedance measurement. R_1 = 15.2 Ω, L_1 = 36.4 µH, R_2 = 72 Ω, L_2 = 144 µH without the sphere.

The IS coil is connected in series with the capacitor C to form the LC circuit with resonant frequency $f_r = ½\pi(L_2C)^{1/2}$. As shown in Figure 6.3, the IS coil and the IC are made by 100 and 20 turns of copper wire wrapped around a plastic pipe (8 mm diameter) and a FR4 support (32 mm diameter), respectively.

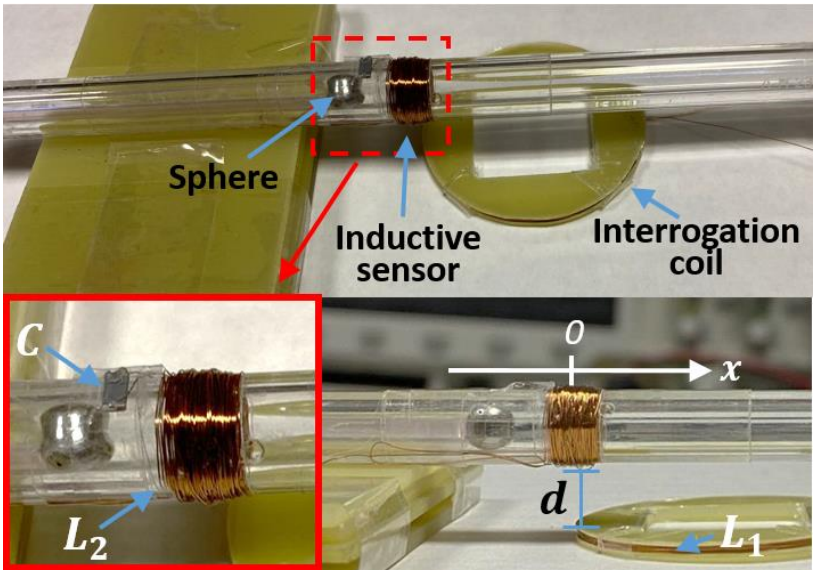

Figure 6.3 – Developed setup used to test the proposed IS for conductive particle detection.

The pipe is used to confine a lead sphere (3 mm diameter) which is moved along the *x* direction by a controlled positioning stage. The sphere induces variations of L_2 and R_2 according to its position *x* thus modifying f_r. By measuring the IC impedance $Z(f) = R(f) + jX(f)$, f_r can be obtained as the frequency *f* where *R(f)* reaches its maximum value [89].

6.3 Experimental results

The IC has been connected to an impedance analyser (HP4194A) to acquire the real part $R(f)$ of $Z(f)$. Without the sphere f_{r0} = 2.51 MHz has been measured. Figure 6.4 shows $R(f)$ for two selected sphere positions (x_1 = -0.5 mm and x_2 = -7.5 mm) while varying *d,* showing that *d* acts only as a scaling factor.

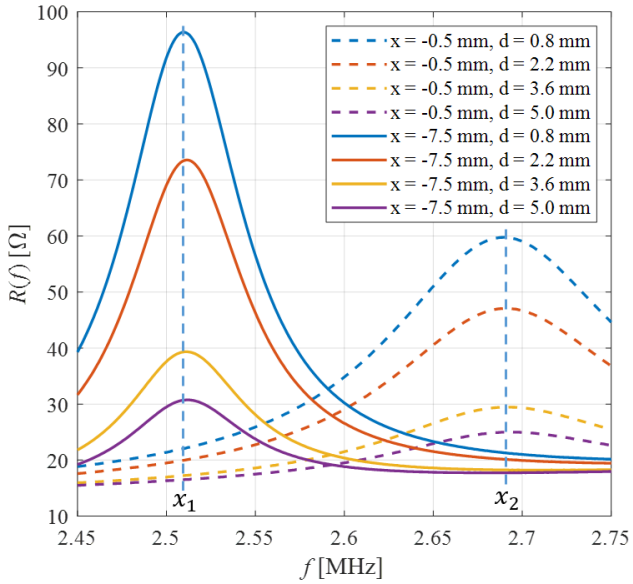

Figure 6.4 – Measured *R(f)* with the conductive sphere placed at x_1 = -0.5 mm and x_2 = -7.5 mm for different values of *d*.

Figure 6.5 shows f_r as a function of *x* for different values of *d*. The sphere has been detected up to $|x| < 7.5$ mm while, at $x = 0$, a maximum frequency variation of $\Delta f_r = f_r - f_{r0}$ = 180 kHz has been measured in the explored range.

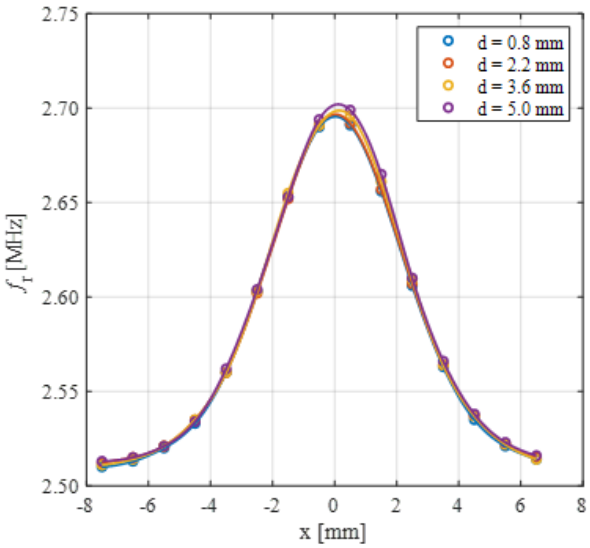

Figure 6.5 – Measured f_r as a function of x for different values of d.

The reported results show minimal residual dependences of f_r on d, which can be eventually reduced by adopting established compensation techniques [89]. The results validate the possibility of the contactless interrogation of an IS for conductive target detection. Ongoing tests are exploring the capability to detect downscaled target size such as conductive particles in nonconductive fluids.

Chapter 7

Noncontact interrogation of passive resistive sensors

In this chapter, a contactless interrogation technique for passive resistive sensors is presented. Traditional techniques, such as impedance amplitude measurement at fixed frequency, are influenced by the relative positioning of the coils, which affects the electromagnetic coupling and, consequently, the accuracy of sensor readings. The novel approach outlined in this chapter exploits the resonant frequency stability and the high quality factor of a Quartz Crystal Resonator (QCR), used as a resonant element, with a series-connected resistor acting as the sensing element. The proposed method focuses on determining the quality factor of the sensor composed of the QCR, the resistive sensing element and the coil necessary for the inductive coupling with an interrogation unit. This approach is basically independent from the interrogation distance, offering a significant advantage over existing techniques. The principle of operations demonstrated through simulations, showing its reliability across various resistive sensing element values and coupling factors. Furthermore, experimental validation is provided through a custom experimental setup, which assesses the performance of the technique under different conditions, including varying distances between the coils. The experimental results has been compared with the simulation results, highlighting the technique effectiveness.

7.1 Resistive sensors

Resistive sensors are a pivotal technology in modern instrumentation and control systems. These sensors operate on the principle that its resistance changes in response to some external stimuli, such as temperature, pressure, force, or the presence of certain chemicals. This simple yet versatile principle allows for a wide array of applications. Owing to the ease of interfacing these sensors with basic electronics, resistive sensors over the years have become a common choice in many fields.

One of the primary applications of resistive sensors is in temperature measurement [137]. Thermistors, a type of resistive sensor, are widely used for their accuracy and sensitivity to temperature changes. Another common application is in force or pressure sensing, where resistive sensors can provide precise measurements in environments ranging from automotive brakes to wearable sensors [138]. Other typical kind of resistive sensor are photoresistors [139], strain gauges [140], potentiometers [141] and magnetoresistors [142]. Resistive sensors play a pivotal role also in chemichal and gas sensing representing a field that is still undergoing significant development in various application from monitoring air quality to detect specific gases or chemical solutions [143].

The development and integration of inkjet printing technology in the fabrication of resistive sensors is a notable advancement to create resistive sensors with unique properties and capabilities. Inkjet printing technology is continuously evolving, enabling the production of resistive sensors that are thinner, more flexible, and more adaptable to different environments and applications [138–140]. This technology has opened up new possibilities for resistive sensors, especially in areas like wearable technology, where the flexibility and lightweight nature of printed sensors can be fully utilized [138,144].

Compared to other sensing technologies like capacitive, inductive, or piezoelectric sensors, resistive sensors often stand out for their simplicity, reliability, and cost-effectiveness. They are typically easier to design and implement, making them a go-to choice for many basic sensing requirements. Indeed, their popularity over other sensor technologies is largely

attributed to their straightforward design, reliability, and affordability, making them a fundamental component in numerous industrial and consumer applications.

7.2 Noncontact interrogation techniques applied to resistive sensors

Contactless interrogation techniques have been proposed for passive resistive sensors in various applications [145]. These techniques primarily rely on measuring the impedance amplitude at a fixed frequency exploiting the electromagnetic coupling between two coils [146]. However, the relative positioning of the two coupled coils impacts the coupling factor between the coils and, subsequently, the measured impedance amplitude used for sensor resistance determination. Indeed, as explained in Chapter 3 the coupling factor acts as a scaling factor in the measured reflected impedance used in the contactless interrogation techniques. Moreover, other techniques, such as phase measurements of impedance, are also contingent on the mutual position of the sensor unit and the interrogation unit [147].

Consequently, changes in relative position or distance between the coils result in inaccuracies or inconsistencies in the sensor reading, making essential to maintain a stable configuration of the coils to ensure reliable and accurate sensor data acquisition.

In this chapter an innovative technique that allows to contactless interrogate a passive sensor with resistive sensing element independent from the interrogation distance is presented. The proposed approach employs a QCR, adopted as the resonant element for contactless interrogation, connected in series to a resistive sensor, which is function of the physical quantity that has to be measured. The proposed contactless interrogation approach is based on the determination of the quality factor of the sensor composed by the QCR and the resistive sensing element.

7.2.1 Quartz crystal resonator

Quartz crystal resonators are electronic components whose operation is based on the piezoelectric properties of quartz, a crystalline form of silicon dioxide. These resonators

exploit the ability of quartz to deform in response to an electric field and conversely, to generate an electric field when mechanically stressed. This bidirectional piezoelectric effect enables the quartz crystal to maintain an oscillation at a highly stable frequency when subjected to an alternating voltage.

When an appropriate voltage is applied across a quartz crystal, it induces a mechanical vibration due to the piezoelectric effect. The physical dimensions and the cut of the crystal determine the natural resonant frequency of these vibrations.

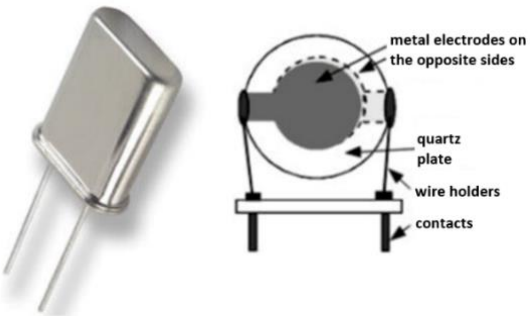

Figure 7.1 – Construction of a typical Quartz Crystal Resonator.

The resonant frequency of an individual quartz crystal resonator is intrinsically linked to its angular orientation in relation to its optical axis. Predominantly, the AT-cut quartz crystal resonator is employed, characterized by its angular displacement of 35°15’ from the Z-axis, or the optical axis of the crystal, as depicted in Figure 7.2.

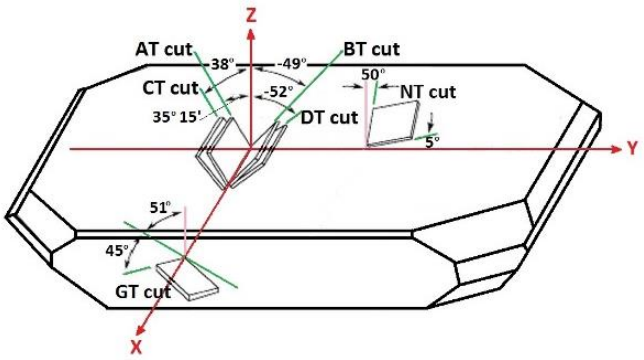

Figure 7.2 – Schematic representation of AT-cut, BT-cut, CT-cut, DT-cut. NT-cut and GT-cut of quartz crystal [148].

The selection of the AT-cut orientation is strategically made to ensure that the temperature coefficient of the resonant frequency is minimized, achieving near-zero variation at a standard temperature of 25 degrees Celsius. In Figure 7.3 is represented the typical relationship between the resonant frequency of an AT-cut quartz crystal and temperature fluctuations, showing the frequency variation as a function of diverse angular orientations relative to the standard AT-cut.

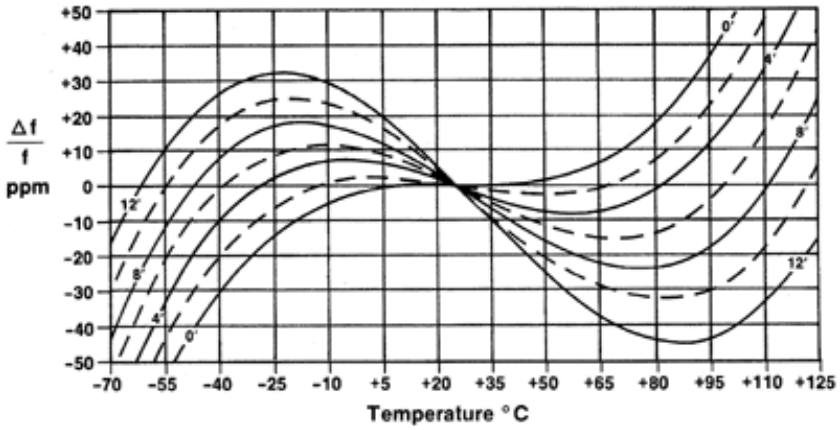

Figure 7.3 – Frequency variation in an AT-cut quartz crystal relative to temperature changes, illustrated as a function of diverse angular orientations compared to the standard AT-cut [149].

An AT-cut QCR sensor functions in the thickness shear mode upon the application of an alternating voltage across the crystal. This application of voltage induces shear deformation within the crystal structure, a phenomenon attributable to the converse piezoelectric effect. Resonance is achieved within this system when there is a periodic exchange of internal energy, oscillating between kinetic and potential forms. This resonant process epitomizes the efficient transfer of energy within the crystal, characterizing its operational dynamics.

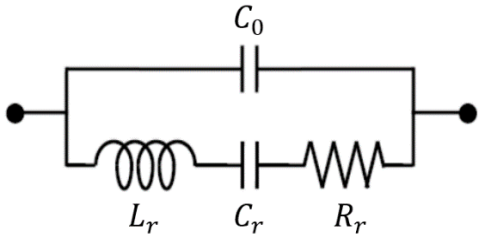

Figure 7.4 – Butterworth-Van Dyke lumped-element model of piezoelectric resonator.

In proximity to its resonant frequency, the Quartz Crystal Resonator can be effectively represented using the Butterworth-Van Dyke (BVD) lumped equivalent electrical model shown in Figure 7.4. This model is structured with two parallel arms: the motional arm and the electrical arm. The motional arm is comprised of series motional parameters: inductance L_r, capacitance C_r, and resistance R_r. Concurrently, the electrical arm embodies a single capacitance C_0, which is indicative of the dielectric properties inherent to the material of the resonator. This dual-arm model facilitates a comprehensive understanding of the QCR electrical behavior in relation to its resonant frequency.

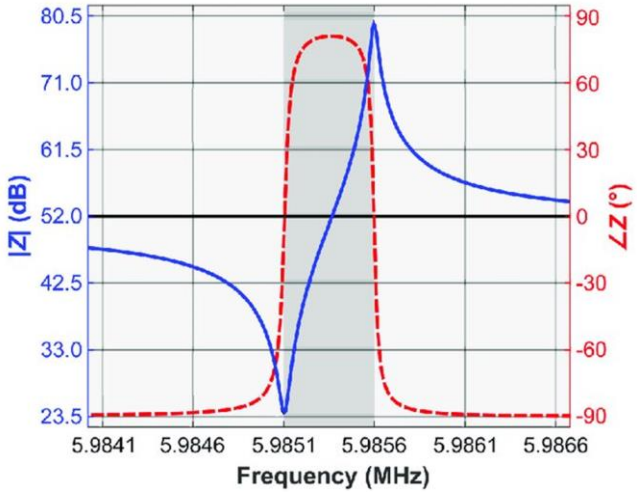

Figure 7.5 – Impedance *Z* response near the resonant frequency of a 6 MHz crystal resonator [150].

From the BVD model of Figure 7.4 it is possible to determine the equivalent impedance of the piezoelectric resonator, which results:

$$Z = \frac{\left(R_r + j2\pi f L_r + \frac{1}{j2\pi f C_r}\right)\frac{1}{j2\pi f C_0}}{R_r + j2\pi f L_r + \frac{1}{j2\pi f C_r} + \frac{1}{j2\pi f C_0}} = \frac{(4\pi^2 f^2 C_r L_r - 1) - j(2\pi f C_r R_r)}{(4\pi f^2 C_r C_0 R_r) + j[8\pi^3 f^3 C_r C_0 L_r - 2\pi f(C_r + C_0)]}. \quad (7.1)$$

From Equation (7.1) can be derived two resonant frequency of the resonator named series-resonance (f_S) and parallel-resonance (f_P):

$$f_S = \frac{1}{2\pi\sqrt{L_r C_r}} \tag{7.2}$$

$$f_P = \frac{1}{2\pi\sqrt{L_r\left(\frac{C_0 C_r}{C_0 + C_r}\right)}}. \tag{7.3}$$

7.2.2 Principle of operation

Figure 7.6 shows the block diagram of the proposed interrogation technique based on impedance measurement. The sensor unit SU is composed of a QCR connected in series with a resistive sensing element R_S and a coil represented by its series inductance and resistance, named L_2 and R_2 respectively. The coil allows the coupling with the interrogation coil IC of the interrogation unit IU through the mutual inductance $M = k(L_1L_2)^{½}$, where k represent the coupling factor which is related to the relative position between the two coils.

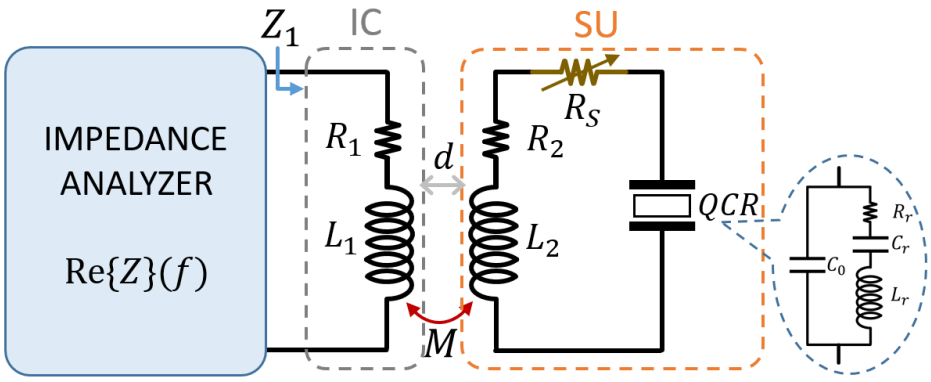

Figure 7.6 – Block diagram of the readout system based on impedance measurement.

According with the BVD lumped equivalent electrical model of the QCR, reported in Figure 7.6, where the motional arm of the resonator is represented by R_r, C_r and L_r, while the electrical arm in represented by C_0, the impedance Z_{QCR} results:

$$Z_{QCR} = \frac{1}{j2\pi f C_0} \parallel \left(R_r + j2\pi f L_r + \frac{1}{j2\pi f C_r} \right). \tag{7.4}$$

With reference to the SU and IU equivalent circuit of Figure 7.6, the impedance Z_1 measured at the interrogation coil can be expressed as:

$$Z_1 = R_1 + j2\pi f L_1 + \frac{4\pi^2 f^2 k^2 L_1 L_2}{R_2 + j2\pi f L_2 + R_S + Z_{QCR}}. \tag{7.5}$$

Close to the QCR series resonant frequency $f_{QCR}=½\pi(L_rC_r)^{1/2}$, the impedance of its motional arm $Z_r = R_r + j2\pi f L_r + 1/(j2\pi f C_r)$ has a magnitude typically much smaller than that of the impedance of C_0, i.e., $|Z_r| << 1/2\pi f_{QCR}\ C_0$. Then, the presence of C_0 can be neglected, resulting in the simplified equivalent circuit of Figure 7.7. With this assumption, the QCR impedance can be approximated as:

$$Z_{QCR} \approx Z_r = R_r + j2\pi f L_r + \frac{1}{j2\pi f C_r}. \tag{7.6}$$

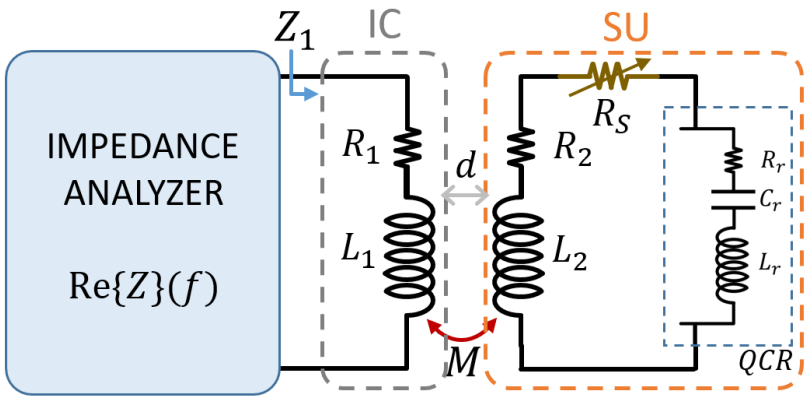

Figure 7.7 – Block diagram of the readout system with BVD equivalent circuit of the QCR neglecting C_0.

It can be seen from Equation (7.5) that the effect of the coupling with the SU results in a reflected impedance Z_{QCR} in series with the primary coil that makes the total impedance Z_1 dependent on the coupling factor k. Nevertheless, the resonant frequency f_{SU} and the quality factor Q_{SU} of the SU can be obtained from the real part of Z_1 [66], given by:

$$\begin{aligned}\mathrm{Re}\{Z_1\} &= R_1 + 4\pi^2 f^2 k^2 L_1 L_2 \frac{R_r + R_2 + R_S}{(R_r + R_2 + R_S)^2 + \left[2\pi f(L_r + L_2) - \frac{1}{2\pi f C_r}\right]^2} \\ &= R_1 + 2\pi f \frac{L_1 L_2}{L_2 + L_r} k^2 Q_{SU} \frac{\frac{f}{f_{SU}}}{1 + Q_{SU}^2 \left(\frac{f}{f_{SU}} - \frac{f_{SU}}{f}\right)^2}.\end{aligned} \tag{7.7}$$

Where:

$$Q_{SU} = \frac{1}{R_2 + R_S + R_r}\sqrt{\frac{L_2 + L_r}{C_r}} \tag{7.8}$$

$$f_{SU} = \frac{1}{2\pi\sqrt{(L_r + L_2)C_r}}. \tag{7.9}$$

The real part of the impedance Z_1 exhibits a maximum at the frequency f_{max_r}:

$$f_{\max_r} = \frac{2Q_{SU}}{\sqrt{4Q_{SU}^2 - 2}} f_{SU} \tag{7.10}$$

From Equation (7.10) can be noted that for large value of Q_{SU}, the SU resonant frequency f_{SU} can be approximated with the frequency f_{max_r}, with a deviation $|f_{max\_r} - f_{SU}|/f_{SU} < 100$ ppm for $Q_{SU} > 50$ [51].

The motional arm Z_r of QCR is characterized by an elevated inductance L_r at the series resonance frequency, generally in the order of milli Henry. Such value is typically greater than the inductance value of the coupled inductor L_2. Consequently, in the condition where

L_r >> L_2, Equations (7.8) and (7.9) can be approximated with Equations (7.11) and (7.12), respectively:

$$Q_{SU} = \frac{1}{R_2 + R_S + R_r}\sqrt{\frac{L_r}{C_r}} \tag{7.11}$$

$$f_{SU} = \frac{1}{2\pi\sqrt{L_r C_r}}. \tag{7.12}$$

The maximum amplitude of Re{Z_1} at $f = f_{max\_r}$ is given by:

$$Z_{R1,max} = \mathrm{Re}\{Z_1\}|_{f=f_{\mathrm{max}\_r}} = R_1 + \frac{8\pi f_2 \frac{L_1 L_2}{(L_2 + L_r)} k^2 Q_{SU}^3}{4Q_{SU}^2 - 1}. \tag{7.13}$$

Considering the condition with Q_{SU} » 1, $Z_{R1,max}$ can be simplified as following:

$$Z_{R1,max} \approx R_1 + 2\pi f_2 \frac{L_1 L_2}{L_2 + L_r} k^2 Q_{SU}. \tag{7.14}$$

The quality factor Q_{SU} can be determined from the full width at half maximum (FWHM) bandwidth of Re{Z_1} [66]. The limiting frequencies of the FWHM bandwidth $f_{FWHM1,2}$ can be determined from the following equation:

$$\frac{\mathrm{Re}\{Z_1\}|_{f=f_{FWHM1,2}} - R_1}{Z_{R1,max} - R_1} = \frac{1}{2}. \tag{7.15}$$

As shown in Figure 7.8 FWHM bandwidth BW_{f_FWHM} can be calculated as the absolute difference between f_{FWHM1} and f_{FWHM2}:

$$BW_{f_{FWHM}} = |f_{FWHM2} - f_{FWHM1}| \tag{7.16}$$

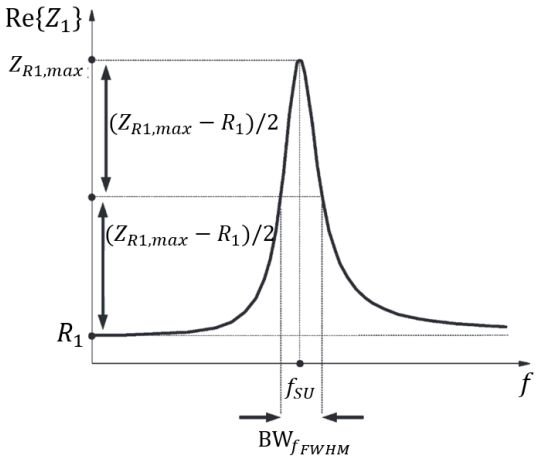

Figure 7.8 – Representation of the real part of the impedance Z_1 measured at the interrogation coil.

Considering Q_{SU} » 1, the FWHM bandwidth and knowing f_{SU}, Q_{SU} can be determined as:

$$Q_{SU} \approx \frac{f_{SU}}{\mathrm{BW}_{f_{FWHM}}}. \tag{7.17}$$

By knowing the QCR motional arm equivalent parameters R_r, C_r, L_r and the coils parameters R_1 and R_2, in the condition where L_r >> L_2, the resistive sensing element value R_S can be determined from the Equation (7.11) of Q_{SU} and results:

$$R_{SQ} = \frac{\sqrt{\frac{L_r}{C_r}}}{Q_{SU}} - R_2 - R_r. \tag{7.18}$$

By knowing R_r, C_r, L_r, R_1, L_2 and f_{SU}, Q_{SU}, it is also possible determine the coupling factor k_Q [66]:

$$k_Q \approx \sqrt{\frac{Z_{R1,max} - R_1}{2\pi f_{SU} \frac{L_1 L_2}{L_2 + L_r} Q_{SU}}}. \tag{7.19}$$

7.3 SPICE simulation

The proposed approach for contactless interrogation of coil-coupled passive resistive sensing element has undergone testing through spice simulation using the LTSpice software and the equivalent circuit presented in Figure 7.9, to verify the applicability of the technique.

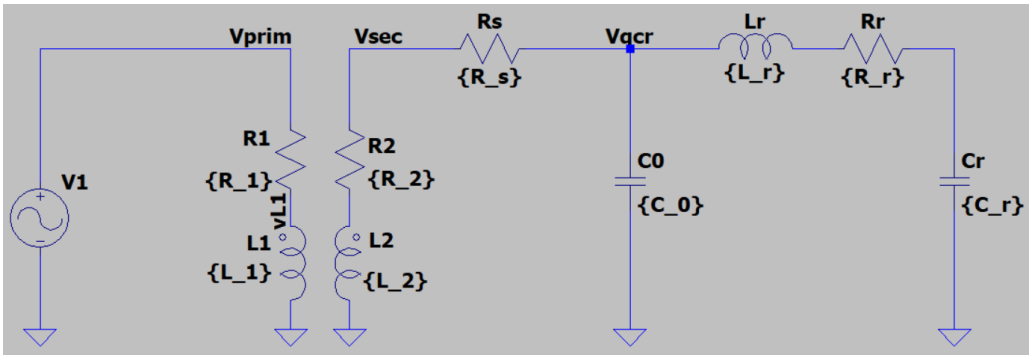

Figure 7.9 – LTSpice circuit configuration employed for simulation purposes.

To perform the simulation typical parameter values have been considered for the components in the equivalent circuit of Figure 7.9. A QCR characterized by C_0 = 10.07 pF, L_r = 131.95 mH, C_r = 10.95 fF, R_r = 19.84 Ω, and f_r = 4.1926 MHz has been considered. Two coupled inductor with inductances L_1 ,L_2 = 8.8 µH and resistances R_1, R_2 = 12 Ω have been included to emulate the coupling coils.

The first simulation has been carried out considering a constant coupling factor k between the coils of 0.2 and a resistive sensing element R_S with variable resistance ranging from 10 Ω to 100 Ω. A step parametric simulation has been conducted with AC analysis in the frequency range from 4.1915 MHz to 4.1935 MHz, i.e. around the resonant frequency.

Figure 7.10 displays the obtained Re{Z_1} for the considered values of R_S with constant k around the resonant frequency. A reduction in the amplitude of Re{Z_1} peak occurs while increasing R_S. As observable in Equation (7.15) the amplitude of Re{Z_1} peak directly impacts the FWHM bandwidth.

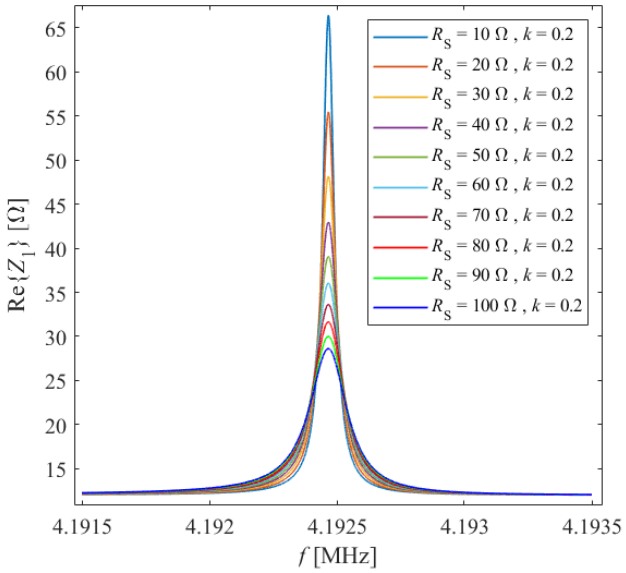

Figure 7.10 – Simulation results of Re{Z_1} as function of f close to the resonant frequency, for different values of R_S between 10 Ω to 100 Ω at constant k = 0.2.

Figure 7.11a shows that within the explored range of R_S a shift of 124 Hz in the FWHM bandwidth has been observed with a corresponding shift in the quality factor of $5.39 \cdot 10^4$, as shown in Figure 7.11b. In the worst cases, i.e. for R_S = 100 Ω, a quality factor of $2.36 \cdot 10^4$ has been obtained, ensuring that the conditions outlined in Section 7.2.2 to apply Equation (7.14) have been met.

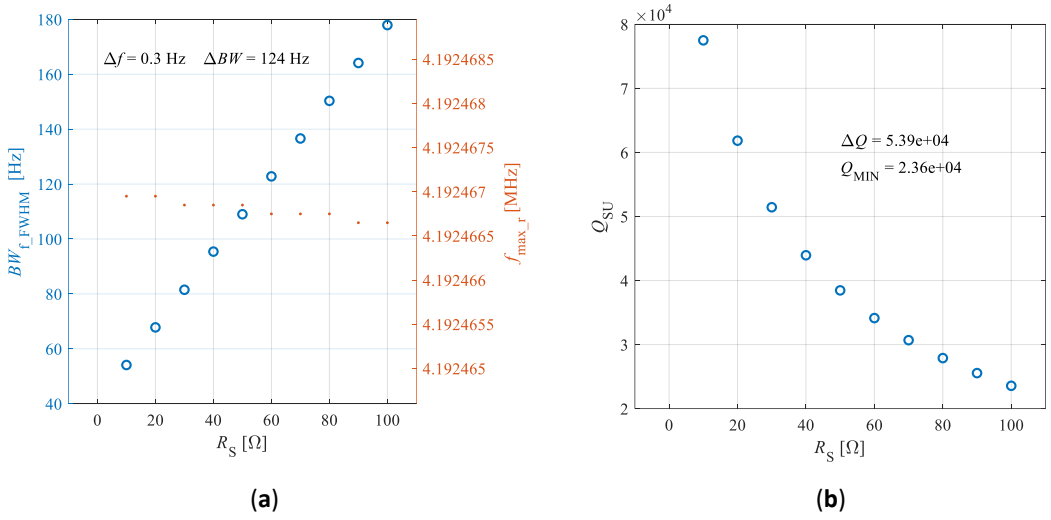

Figure 7.11 – Simulation results of (a) BW_{f_FWHM}, f_{max_r} and (b) Q_{SU} for different values of R_S between 10 Ω to 100 Ω at a constant k = 0.2.

Consistent with the expectations derived from Equation (7.11) of Q_{SU}, Figure 7.11 shows a linear relationship between the inverse of the quality factor and R_S, with a maximum linearity error of 0.0676 % of the span.

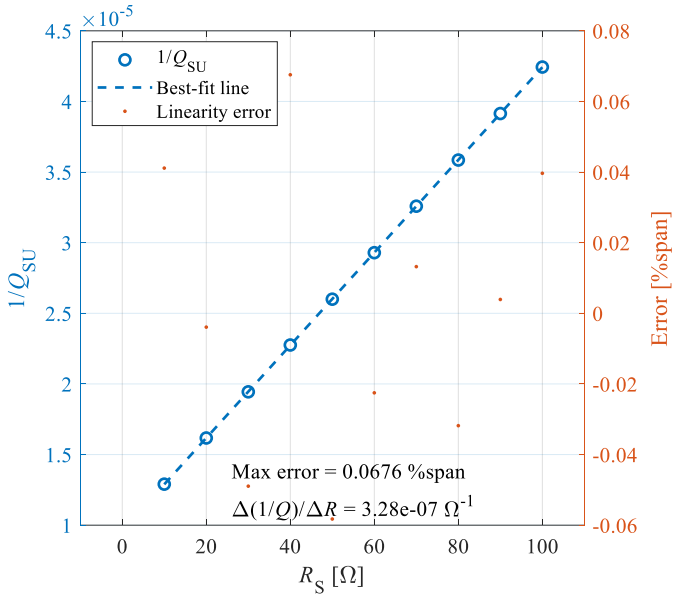

Figure 7.12 – Derived $1/Q_{SU}$ values obtained with the proposed technique and corresponding linearity error as a function of R_S.

By applying the theoretical formula presented in (7.18) to retrieve R_S from the Q_{SU} values determined using the proposed method, the R_{SQ} values shown in Figure 7.13 are obtained. It can be observed that there is no exact correspondence between the values of R_S and the corresponding determined R_{SQ} values. This discrepancy arises due to the presence of C_0 in the equivalent model of the QCR used in the simulation, which is not considered in the theoretical formulation provided in Section 7.2.2. Conducting the same simulation without considering the capacitance C_0 results in a perfect match between the reference values of R_S and the R_{SQ} values determined using the proposed technique.

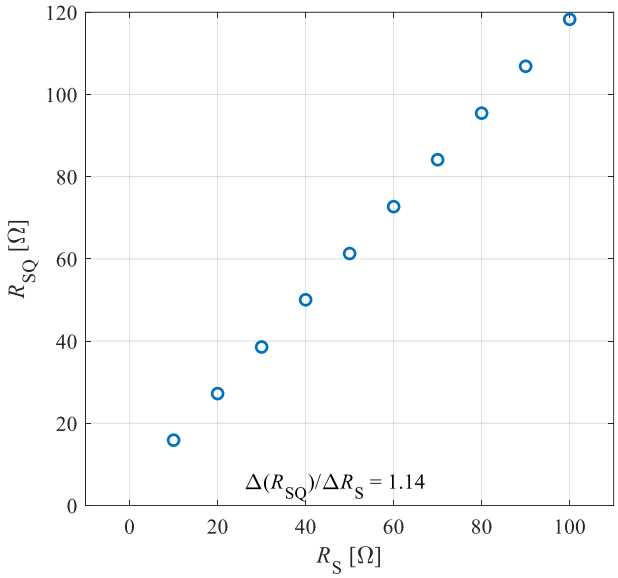

Figure 7.13 – R_{SQ} values determined from quality factor with the proposed technique as function of R_S.

Two additional simulations has been executed using different ranges of R_S. Figure 7.14a shows the obtained Re{Z_1} around the resonant frequency for R_S values ranging from 100 Ω to 200 Ω, while Figure 7.14b show the corresponding quality factor values.

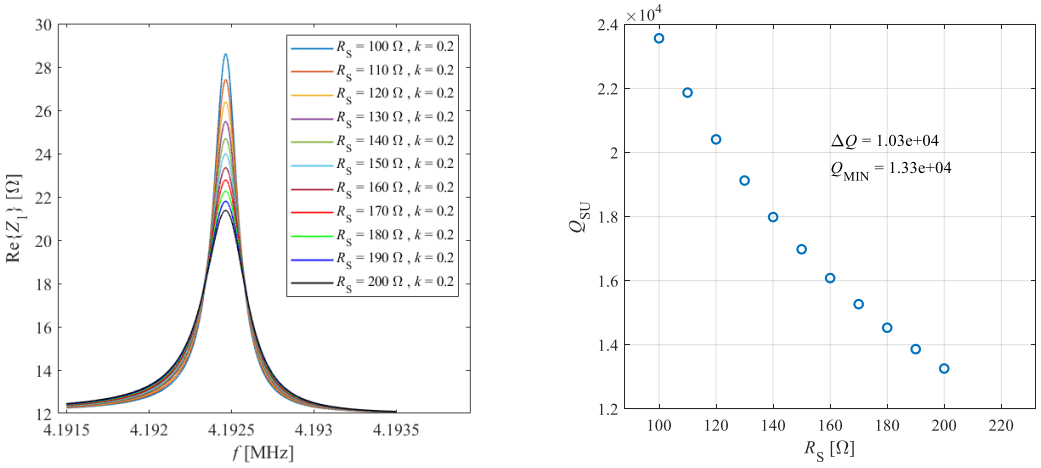

Figure 7.14 – (a) Simulation results of Re{Z_1} as function of f close to the resonant frequency, for different values of R_S between 100 Ω to 200 Ω at a constant k = 0.2; (b) corresponding Q_{SU} values as a function of R_S.

Figure 7.15a shows the obtained Re{Z_1} around the resonant frequency for R_S values spanning from 1000 Ω to 1100 Ω, and Figure 7.15b show the corresponding quality factor.

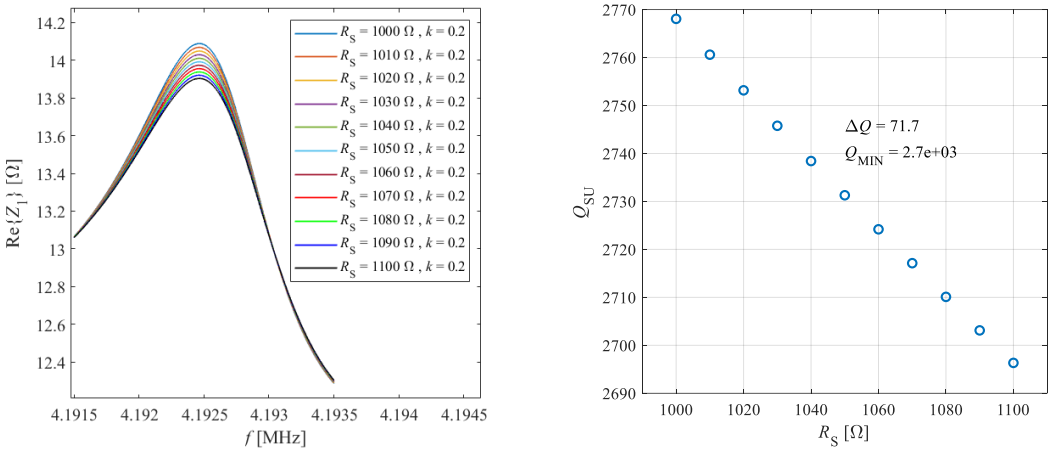

(**a**) (**b**)

Figure 7.15 – (a) Simulation results of Re{Z_1} as function of f close to the resonant frequency, for different values of R_S between 1000 Ω to 1100 Ω at a constant k = 0.2; (b) corresponding Q_{SU} values as a function of R_S.

In both R_S ranges, the condition Q_{SU} » 1 to apply Equation (7.14) results satisfied.

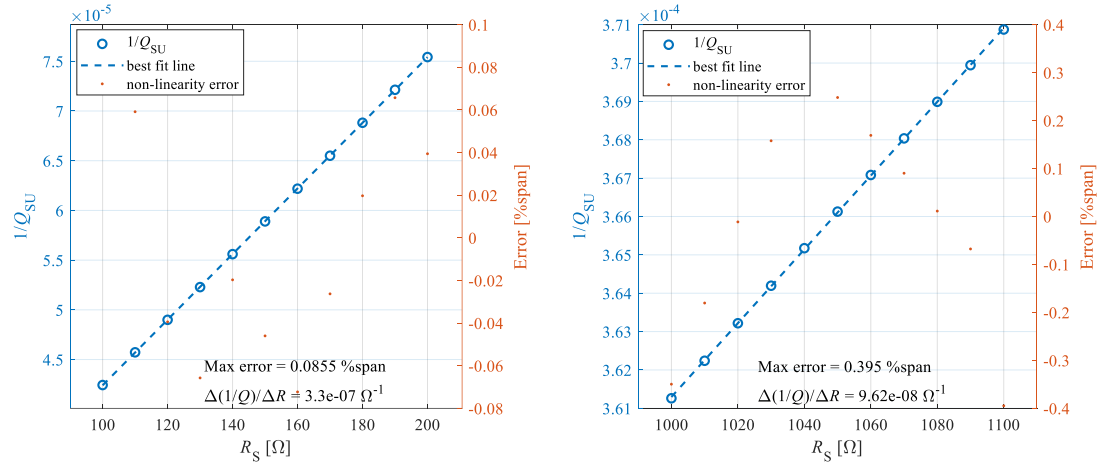

(**a**) (**b**)

Figure 7.16 – (a) Derived 1/Q_{SU} values obtained with the proposed technique and corresponding linearity error as a function of R_S between 100 Ω and 200 Ω; (b) derived 1/Q_{SU} values obtained with the proposed technique and corresponding linearity error as a function of R_S between 1000 Ω and 1100 Ω.

As observable in Figure 7.16a and Figure 7.16b, a linear relationship between the inverse of the quality factor and R_S has been obtained for both ranges. For R_S values between [100 Ω 200 Ω] and between [1000 Ω 1100 Ω], a linearity error of 0.0855 % and 0.395 % of span has been obtained respectively.

	k = 0.2 R_S = 10 – 100 Ω	k = 0.2 R_S = 100 – 200 Ω	k = 0.2 R_S = 1000 – 1100 Ω
$\Delta BW_{f_{FWHM}}$ [Hz]	124	138	40.3
$\Delta f_{\max_r}$ [Hz]	0.3	0.3	0.3
ΔQ_{SU}	$5.39 \cdot 10^{4}$	$1.03 \cdot 10^{4}$	71.7
Q_{MIN}	$2.36 \cdot 10^{4}$	$1.33 \cdot 10^{4}$	$2.7 \cdot 10^{3}$
Nonlinearity error of $1/Q_{SU}$ [%$span$]	0.0676	0.0855	0.395
$\frac{\Delta(1/Q_{SU})}{\Delta R_S}$ [Ω^{-1}]	$3.28 \cdot 10^{-7}$	$3.30 \cdot 10^{-7}$	$9.62 \cdot 10^{-8}$
$\frac{\Delta R_{SQ}}{\Delta R_S}$	1.14	1.14	0.33

Table 7.1 – Simulation results with constant *k* and different ranges of R_S.

As can be noted from Table 7.1,the linearity error increases as R_S values rise, a phenomenon that may be attributed to the behaviour due to the presence of C_0.

A second simulation has been conducted to assess the performance of the applied techniques as a function of the interrogation distance and, consequently, the coupling factor. In this analysis, a fixed value of R_S = 100 Ω has been considered, and a step parametric simulation was carried out with k ranging from 0.1 to 0.4. Figure 7.17a shows the real part of impedance Z_1 around the resonant frequency for the tested values of k while maintaining R_S constant. It can be observed that, as expected, the sensor resonant frequency remains constant as the coupling factor k varies. Notably, there is an observable increase in the peak amplitude of Re{Z_1} with increasing k, as predicted by the Equation (7.7) where k only acts as an amplitude scaling factor. The quality factor does not change as the coupling factor k varies within the explored range, as shown in Figure 7.17b.

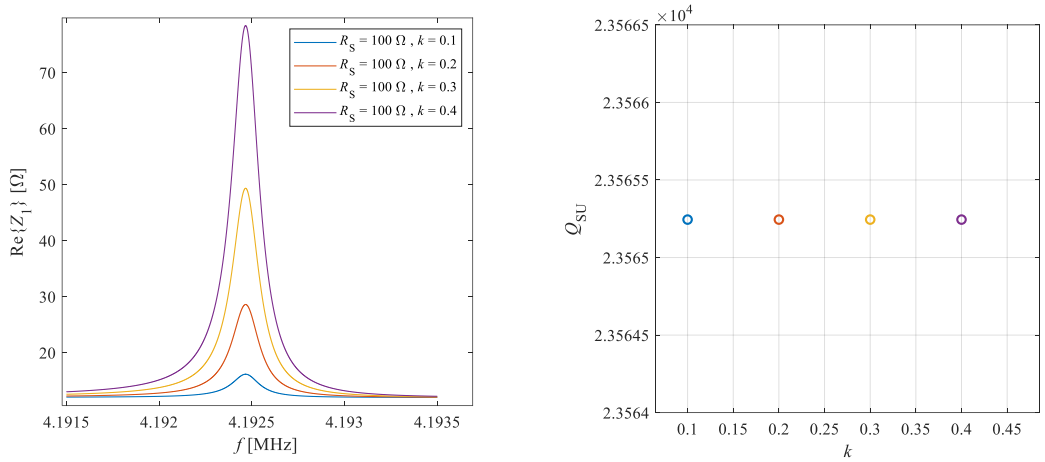

(**a**) (**b**)

Figure 7.17 – (a) Real part of impedance Z_1 obtained with a fixed value of R_S for different k values; (b) corresponding Q_{SU} as a function of k.

Simulations have been repeated for different R_S values ranging from 100 Ω to 200 Ω. Figure 7.18a shows the obtained values of 1/Q for all the tested R_S values as a function of k, while Figure 7.18b shows the obtained values of 1/Q for all the tested k values as a function of R_S. As expected, it can be observed that, for each R_S value, the quality factor remains constant within the considered range of k.

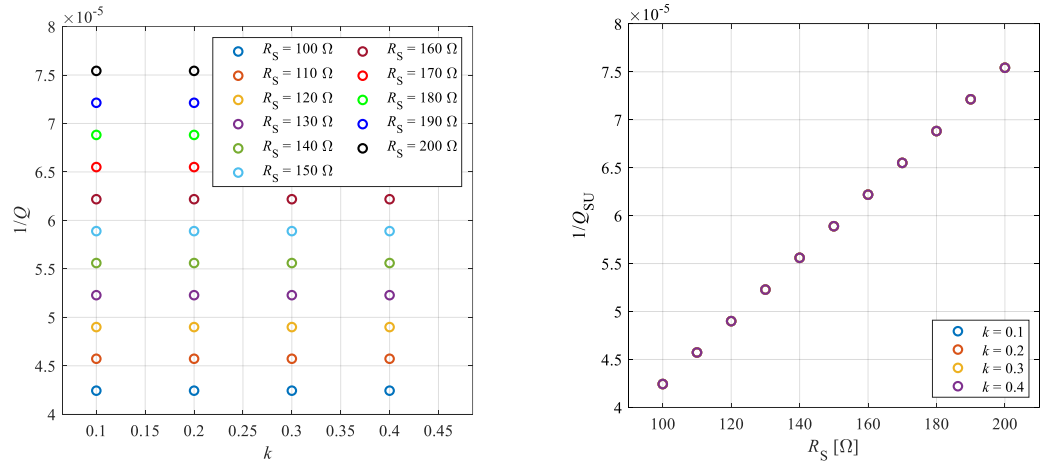

(**a**) (**b**)

Figure 7.18 – Derived 1/Q_{SU} values obtained with the proposed technique as a function of (a) k between 0.1 and 0.4 and (b) R_S between 100 Ω and 200 Ω.

7.3.1 Effect of parasitic capacitance in parallel to interrogation coil

As discussed in Chapter 3, the presence of a parasitic capacitance in parallel with the interrogation coil introduces a dependency of the measured resonant frequency on the coupling factor, and subsequently, on the interrogation distance. To investigate this effect, the proposed approach has been tested considering a capacitance C_p of 10 pF added in parallel to the primary coil, constituted by inductance L_1 and resistance R_1, as illustrated in Figure 7.19.

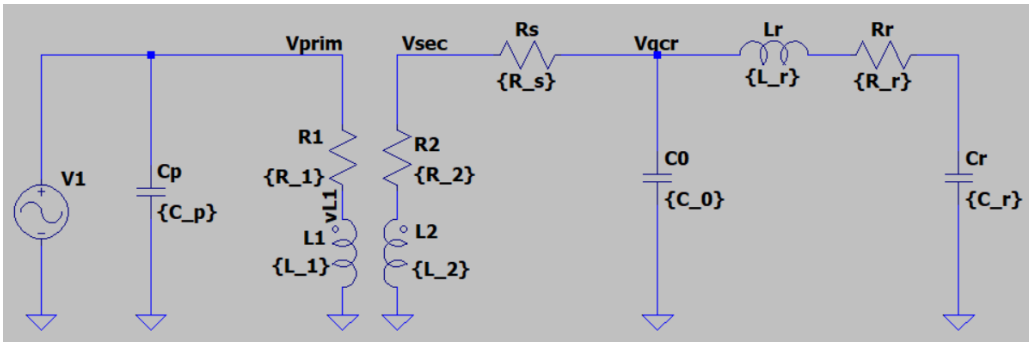

Figure 7.19 – LTSpice circuit configuration with parasitic capacitance C_p, employed for simulation purposes.

A step parametric AC simulation in the frequency range from 4.1915 MHz to 4.1935 MHz, i.e. centred around the resonant frequency, has been conducted.

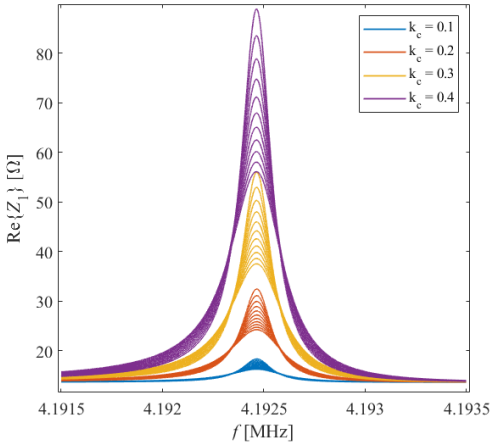

Figure 7.20 – Real part of impedance Z_1 obtained from simulation with parasitic capacitance C_p for different values of R_s between 100 Ω and 200 Ω and for different k values between 0.1 and 0.4.

Variable values of k, ranging from 0.2 to 0.4 and variable values of R_S ranging from 100 Ω to 200 Ω has been considered. Figure 7.20 shows Re{Z_1} around the resonant frequency for different k values across all tested R_S values.

The estimated inverse of the quality factor $1/Q$ does not remain constant with the coupling factor k, and, consequently, with the interrogation distance, as shown in Figure 7.21a. As a result, Figure 7.21b shows how the relationship between $1/Q$ and R_S exhibits varying sensitivities for different values of k. This variation highlights that the sensor resistance cannot be directly determined from the quality factor of the sensor unit, as assumed without the parasitic capacitance.

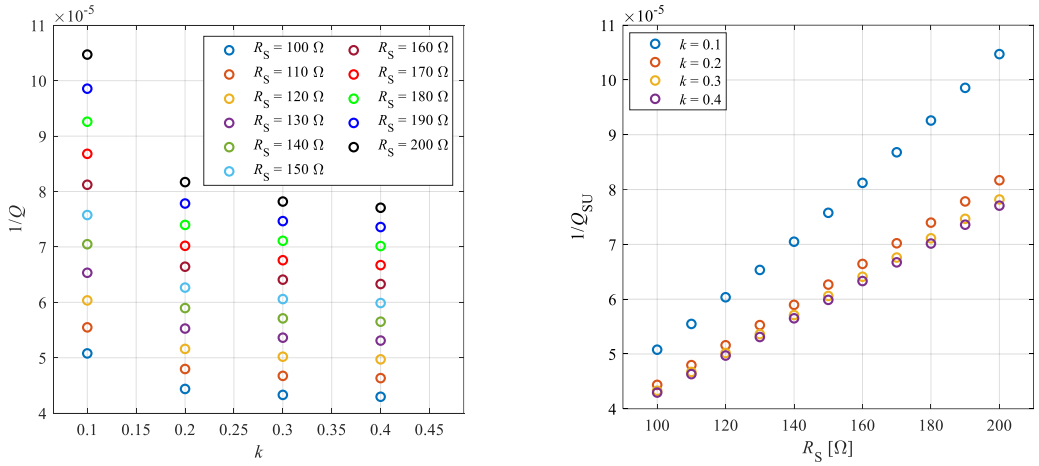

Figure 7.21 – Derived $1/Q_{SU}$ values obtained with the proposed technique, with presence of parasitic capacitance C_p, (a) as a function of k between 0.1 and 0.4 for different R_S values, and (b) as a function of R_S between 100 Ω and 200 Ω for different k values.

As detailed in Chapter 3, the presence of the parasitic capacitance in parallel with the interrogation coil can be effectively mitigated through the application of compensation techniques. This enables the implementation of the proposed interrogation approach, ensuring its independence from the interrogation distance.

7.4 Experimental results

Following the simulations, the proposed approach has been experimentally validate for contactless interrogation of resistive sensing element.

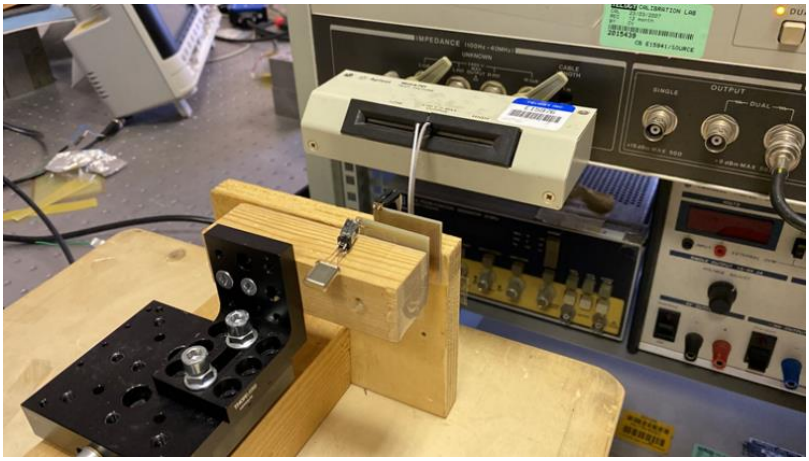

Figure 7.22 – Experimental setup employed to test the proposed technique.

To assess the proposed technique, a customized experimental setup has been devised, as shown in Figure 7.22. The interrogation coil (IC), milled from a flame-resistant substrate (FR4) with dimensions of 35 mm × 35 mm, has been fixed to the structure and connected to an impedance analyser (HP4194A). The sensor unit (SU) coil, with the same IC characteristics, has been fixed to a precision-controlled positioning stage, facilitating the adjustment of the distance between the two coils, which are maintained in parallel alignment. The SU coil has been connected, in accordance with the schematic presented in Figure 7.6, in a series configuration with a commercial QCR and with the reference resistor. The QCR has been characterized through the impedance measurement near its resonant frequency. By fitting the BVD model with the measured conductance (G) and susceptance (B), as illustrated in Figure 7.23a and Figure 7.23b respectively, a capacitance C_0 = 10.07 pF, and L_r = 131.6 mH, C_r = 10.95 fF, R_r = 19.84 Ω have been determined.

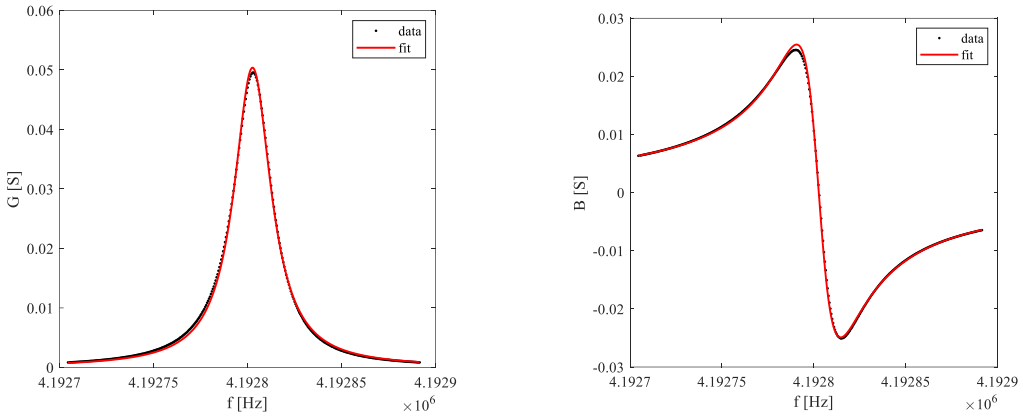

Figure 7.23 – Measured and fitted values of the conductance (a) and susceptance (b) of the adopted QCR around the resonant frequency.

Surface-Mount Device (SMD) commercial resistors, with a tolerance of 1%, has been used as reference resistors for R_S. To facilitate the interchangeability of the reference resistors within the SU, the selected SMD resistor was soldered onto a compact commercial connector, as shown in Figure 7.24.

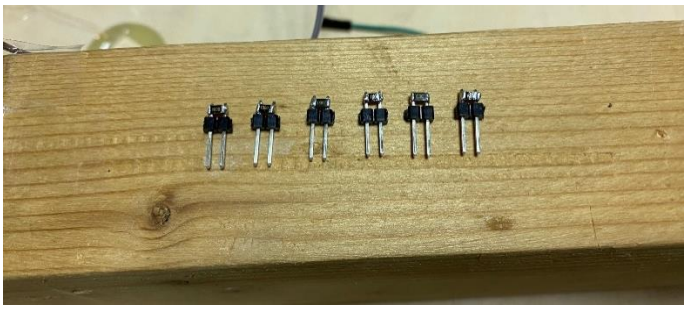

Figure 7.24 – Surface-Mount Device (SMD) commercial resistors soldered onto a compact commercial connector used as reference resistors for R_S.

The first experimental characterization has been carried out with a constant distance d between the coils of 1 mm and a resistive sensing element R_S with variable resistance ranging from 100 Ω to 200 Ω. For the data collection, the impedance analyser has been set with a frequency span of 400 Hz and 401 data points per sweep frequency measurement from 4.1924 MHz to 4.1298 MHz.

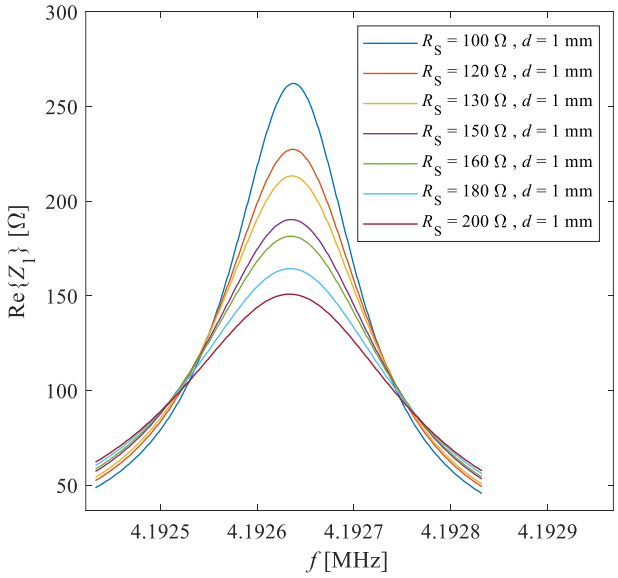

Figure 7.25 – Measured Re{Z_1} as function of f close to the resonant frequency, for different R_S values between 100 Ω to 200 Ω at a constant d = 1 mm.

Figure 7.25 shows the obtained Re{Z_1} for the considered values of R_S. As expected, an observable reduction in the amplitude of Re{Z_1} peak is noted with increasing the value of R_S. Figure 7.26a shows that within the explored range of R_S, a shift of 127 Hz in the FWHM bandwidth has been observed with a corresponding shift in the quality factor of $1.16 \cdot 10^4$, as shown in Figure 7.26b.

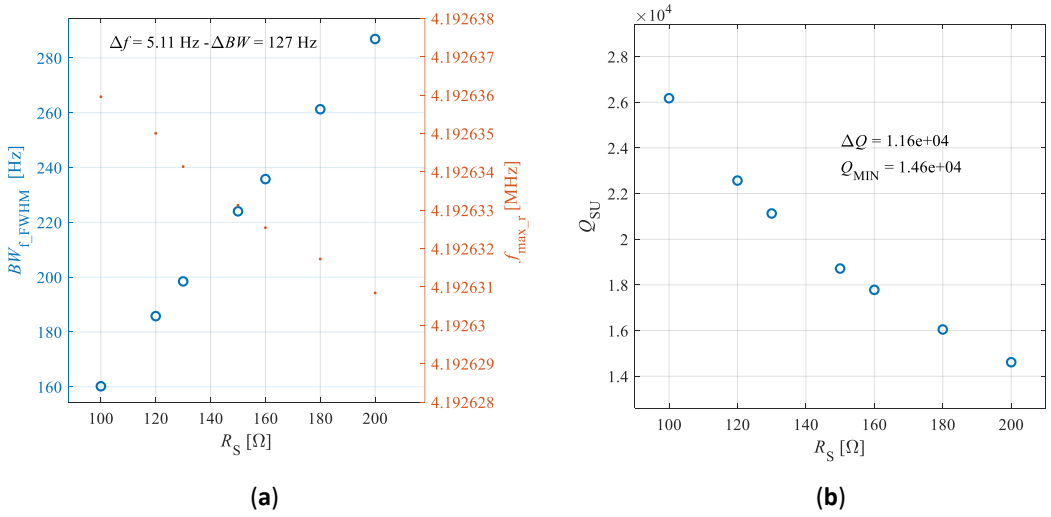

Figure 7.26 – Experimental results of (a) BW_{f_FWHM}, f_{max_r} and (b) Q_{SU} for different R_S values between 100 Ω to 200 Ω at a constant d = 1 mm.

In the worst case, i.e. for R_S = 100 Ω, a quality factor of $1.46 \cdot 10^4$ has been obtained, ensuring that the conditions outlined in Section 7.2.2 to apply Equation (7.14) has been satisfied.

Consistent with the expectations derived from Equation (7.11) of Q_{SU} and the result of the simulation in Section 7.3, Figure 7.27 shows a linear relationship between the inverse of the quality factor and R_S, with a maximum linearity error of 0.352 % of the span.

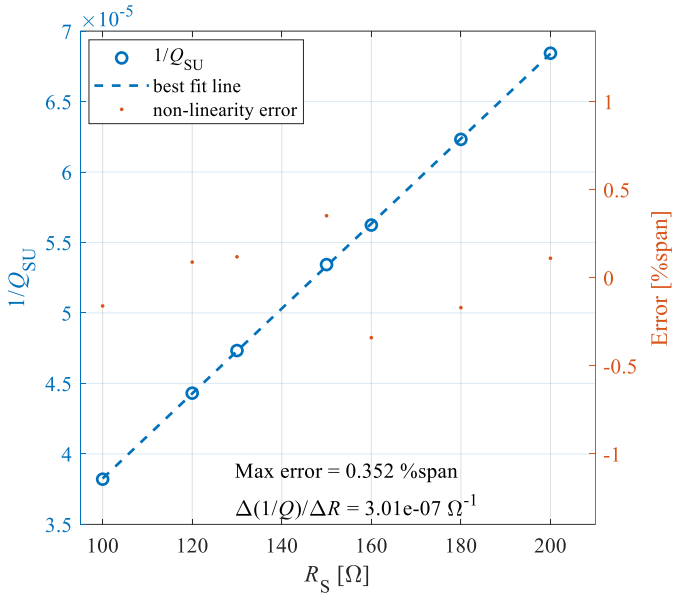

Figure 7.27 – Experimental results of $1/Q_{SU}$ values obtained with the proposed technique and corresponding linearity error as a function of R_S.

By applying the theoretical formula to retrieve R_S from the Q_{SU} values, as presented in Equation (7.18), the R_{SQ} values shown in Figure 7.28 have been obtained. These experimental results are in alignment with the outcomes of the simulations performed with the presence of C_0. However, as expected, they do not perfectly align with the theoretical predictions, which do not take into account C_0 or the parasitic capacitance C_p. By knowing the value of C_0 and applying the compensation techniques for C_p, as illustrated in Chapter 3, it become possible to accurately determine the value of R_S.

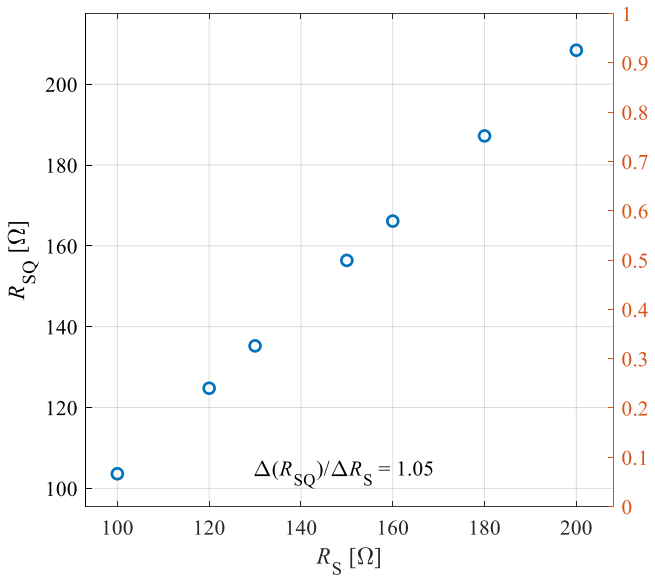

Figure 7.28 – R_{SQ} values determined through quality factor estimation from experimental result using the proposed technique, as a function of R_S with fixed d = 1 mm.

A secondary experimental characterization to evaluate the efficacy of the employed techniques in relation to the interrogation distance has been performed. In this tests, a fixed reference resistor R_S = 100 Ω has been considered, and the same acquisition has been carried out with d ranging from 1 to 10 mm. Figure 7.29a shows the real part of impedance Z_1 around the resonant frequency for the tested distances while maintaining a constant R_S.

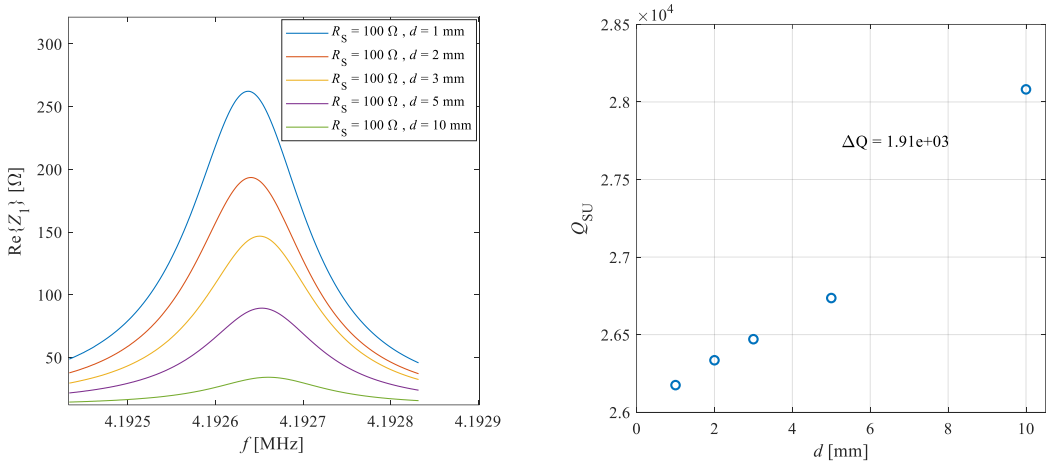

(**a**) (**b**)

Figure 7.29 – (a) Measured real part of impedance Z_1 obtained with fixed R_S = 100 Ω for different d between 1 mm and 10 mm; (b) corresponding Q_{SU} as a function of d.

Notably, there is an observable decrease in the peak amplitude of Re{Z_1} with increasing d, aligning with Equation (7.7) considering that the coupling factor k decrease with increasing the distance between the coils, and a shift in the frequency corresponding to the peak of Re{Z_1} can also be observed. The calculated quality factor increase as the distance d increase, with a variation of $1.91 \cdot 10^3$ in the explored range, as shown in Figure 7.29b.

The same characterization has been repeated for different values of R_S ranging from 100 Ω to 200 Ω, as shown in Figure 7.30a. Figure 7.21b shows the relationship between $1/Q$ and R_S, demonstrating, according with simulation expectations, variable sensitivities across different values of d.

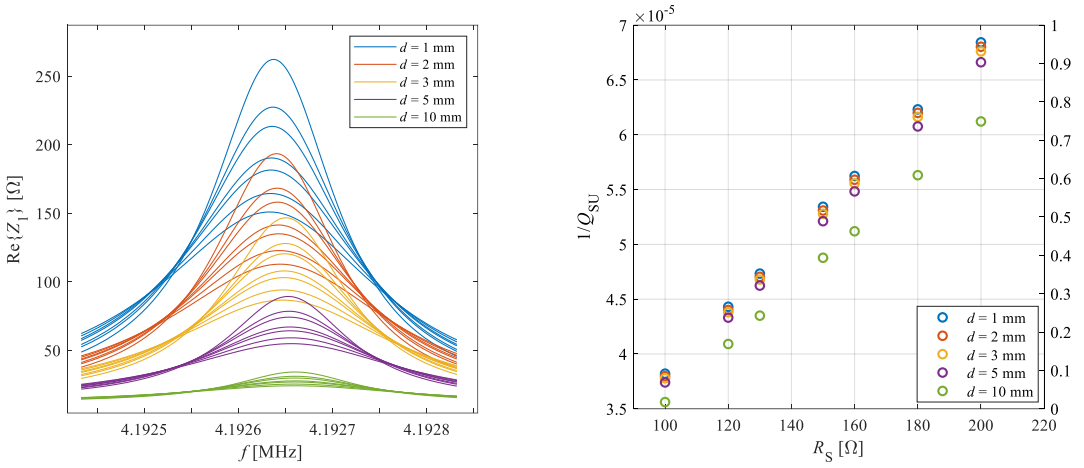

Figure 7.30 – (a) Measured real part of impedance Z_1 for different values of R_S between 100 Ω and 200 Ω, for different d values between 1 mm and 10 mm; (b) correspondent $1/Q_{SU}$ values obtained with the proposed technique as a function of R_S between 100 Ω and 200 Ω for different d values.

In Table 7.2 is reported a summary and a comparison of the results obtained with simulations and measurements with constant k and d.

	SIMULATION k **= 0.2** R_S **= 100 – 200 Ω NO** C_P	**SIMULATION** k **= 0.2** R_S **= 100 – 200 Ω** $C_P = 10$ **pF**	**MEASUREMENTS** d **= 1 mm** R_S **= 100 – 200 Ω**
ΔBW [Hz]	138	157	127
$\Delta f_{\max_r}$ [Hz]	0.3	0.6	5.11
ΔQ_{SU}	$1.03 \cdot 10^4$	$1.03 \cdot 10^4$	$1.16 \cdot 10^4$
Q_{MIN}	$1.33 \cdot 10^4$	$1.22 \cdot 10^4$	$1.46 \cdot 10^4$
Non-linearity error of $1/Q_{SU}$ [$\%span$]	0.0855	0.593	0.352
$\frac{\Delta(1/Q_{SU})}{\Delta R_S}$ [Ω^{-1}]	$3.3 \cdot 10^{-7}$	$3.73 \cdot 10^{-7}$	$3.01 \cdot 10^{-7}$

Table 7.2 – Comparison between simulation and experimental results achieved with constant coupling factor *k* and interrogation distance *d*.

The results obtained from simulations and measurements are consistent and lead to the same conclusions. Only a notable discrepancy is observed in the variation of f_{max_r} between the simulated and measured obtained values.

	SIMULATION k **= 0.1 – 0.4** R_S **= 100 – 200 Ω NO** C_P	**SIMULATION** k **= 0.1 – 0.4** R_S **= 100 – 200 Ω** $C_P = 10$ **pF**	**MEASUREMENTS** d **= 1 -10 mm** R_S **= 100 – 200 Ω**
ΔBW [Hz]	138	259	138
$\Delta f_{\max_r}$ [Hz]	0.3	2.1	28.7
ΔQ_{SU}	$1.03 \cdot 10^4$	$1.37 \cdot 10^4$	$1.35 \cdot 10^4$

Table 7.3 – Comparison between simulation and experimental results achieved for different values of coupling factor *k* and interrogation distance *d*.

The results obtained for different values of coupling factor and interrogation distance, reported in Table 7.3, also result consistent between simulations and experimental characterization. As well in this case a notable discrepancy is observed in the variation of f_{max_r} between the simulated and measured values and the variation in the in the FWHM bandwidth obtained with the measurements results is more consistent with the simulation performed without the parasitic capacitance C_p.

The resolution of the proposed technique has been verified performing 100 repeated measurements with a measurement every 6.57 seconds with a frequency span of 200 Hz and 401 data points per sweep frequency measurement from 4.1925 MHz to 4.1927 MHz. Figure 7.31a shows the obtained Re{Z_1} for the repeated measurements. The corresponding obtained values of $1/Q$ plotted in Figure 7.31b lead to a standard deviation of $\sigma_{1/Q} = 2.74 \cdot 10^{-9}$. Considering the sensitivity $S = \Delta(1/Q)/\Delta R$ obtained from Figure 7.27, the corresponding standard deviation for the resistance $\sigma_R = \sigma_{1/Q}/|S|$ results equal to 9.1 mΩ, which can be considered the equivalent resistance resolution at one σ.

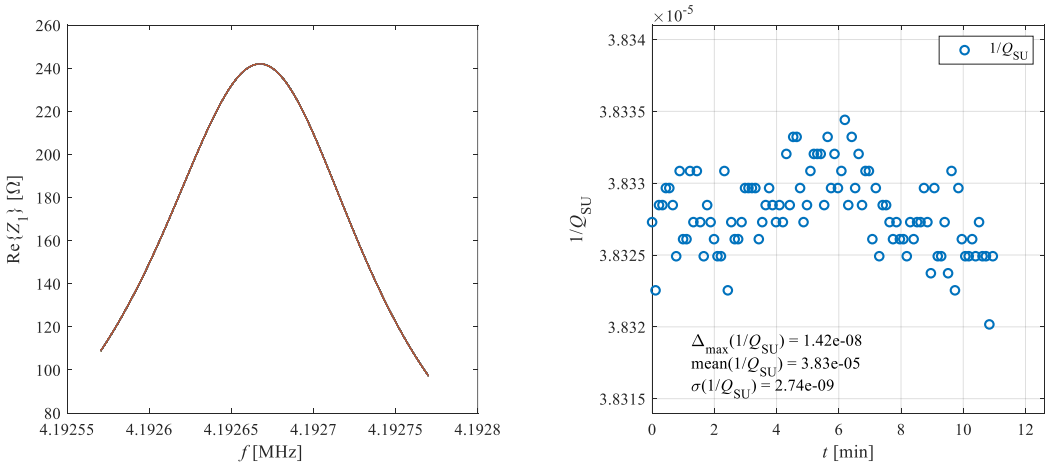

(**a**) (**b**)

Figure 7.31 – (a) Results of 100 repeated measurements of Re{Z_1} obtained with fixed R_S = 100 Ω and fixed d = 1 mm with a measurement every 6.57 seconds with a frequency span of 200 Hz and 401 data points per sweep frequency measurement; (b) corresponding $1/Q_{SU}$ values as a function of t.

The stability of the proposed system over time has been validated by performing consecutive measurements taken at 5-minute intervals over a 12-hour duration, employing a frequency span of 200 Hz and 401 data points per sweep frequency measurement ranging from 4.1925 MHz to 4.1927 MHz. In this timeframe, the room temperature T has been monitored using a PT1000 sensor. Figure 7.32a shows the obtained FWHM bandwidth BW as function of time t along with the room temperature, while Figure 7.32b reports BW as function of the measured room temperature.

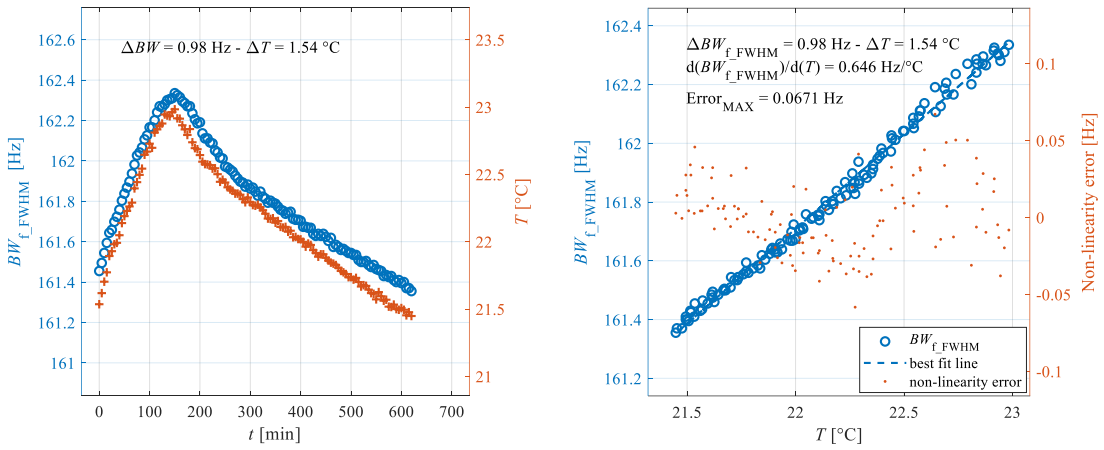

Figure 7.32 – Results of repeated measurements taken at 5-minute intervals over a 12-hour duration: (a) BW_{f_FWHM} and T as a function of t; (b) BW_{f_FWHM} and corresponding non-linearity error as a function of T.

It results a linear dependence of BW from T with a sensibility of 0.646 Hz/°C in the considered range of temperature. Figure 7.33a shows the measured frequency f_{max_r} related to the maximum of Re{Z_1}, which differently to BW do not assume a linear behaviour as function of T.

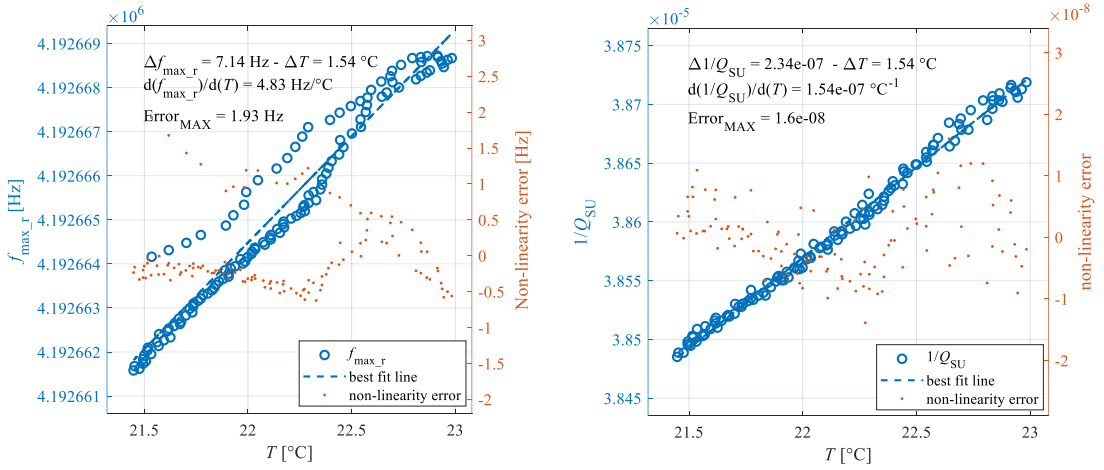

Figure 7.33 – Results of repeated measurements taken at 5-minute intervals over a 12-hour duration: (a) f_{max_r} and corresponding non-linearity error as a function of T; (b) $1/Q_{SU}$ and corresponding non-linearity error as a function of T.

Figure 7.33b shows the corresponding $1/Q$ as function of T, which present a linear behaviour with a resulting sensibility of $1.54 \cdot 10^{-7}$ Ω^{-1}. It therefore appears that $1/Q$ maintain the linearity observed with BW without being significantly affected by f_{max_r} while still appearing in the equation to determine Q. The resulting variation $\Delta f_{max\_r} = 7.14$ Hz of f_{max_r} is equivalent to a relative change with respect to f_{max_r} of 1.7 ppm while the variation $\Delta BW = 0.98$ Hz of BW correspond to a relative change with respect to BW of 6000 ppm, and therefore dominant compared to the variations obtained on f_{max_r}.

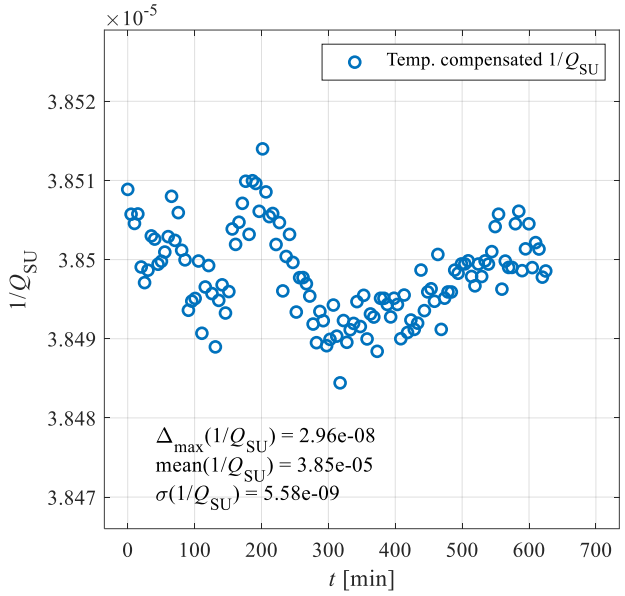

Figure 7.34 – Temperature compensated $1/Q_{SU}$ as function of t resulting from repeated measurements taken at 5-minute intervals over a 12-hour duration.

By compensating the temperature effects, whose results are reported in Figure 7.34, the resulting standard deviation of $1/Q$ is $\sigma_{1/Q} = 5.58 \cdot 10^{-9}$. Considering the sensitivity S obtained from data of Figure 7.27, the corresponding standard deviation for the resistance $\sigma_R = \sigma_{1/Q}/|S|$ results equal to 18.5 mΩ.

To verify if the observed variation in $1/Q$, linked to temperature changes, can be attributed to the temperature effect on the reference resistance R_S or to other components of the sensor unit (SU), another characterization has been conducted with only the QCR and the coil L_2 in the SU, i.e., with $R_S = 0$ Ω.

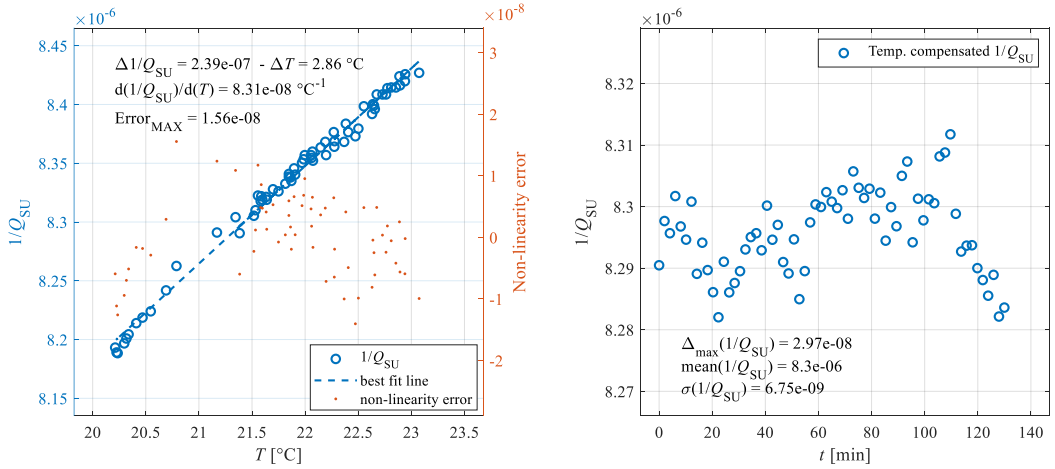

Figure 7.35 – Results of repeated measurements with R_S = 0 Ω taken at 5-minute intervals over a 2-hour duration: (a) $1/Q_{SU}$ and corresponding non-linearity error as function of T; (b) temperature compensated $1/Q_{SU}$ as a function of t.

As shown in Figure 7.35a, in this case as well, the trend exhibited by $1/Q$ is linearly correlated with the ambient temperature variation, with a sensitivity of $8.31 \cdot 10^{-8}$ °C^{-1}. This suggests that the temperature sensitivity shown in Figure 7.33b can be attributed to R_S for approximately half of its extent, while the remaining half can be ascribed to the QCR and coil of the SU. As shown in Figure 7.32b, *BW* presents a linear relationship with temperature, while f_{max_r} does not present relevant specific temperature-dependent variations, as shown in Figure 7.33a. The theoretical expression to calculate the quality factor, reported in Equation (7.8), include the resistive, capacitive and inductive elements of the SU. Indeed, the formula to calculate the SU resonant frequency, reported in Equation (7.9), only includes the capacitive and inductive elements of the SU. This suggest that the SU temperature dependence observed without the sensing element, i.e. with R_S = 0 Ω, can be attributed to the resistance R_2 of the coil or to the resistive component R_r of the motional arm of the QCR.

The temperature compensated $1/Q$ reported in Figure 7.35b, obtained with R_S = 0 Ω, presents a standard deviation $\sigma_{1/Q} = 6.75 \cdot 10^{-9}$. This value aligns with the standard deviation of Figure 7.34, obtained with R_S = 100 Ω. Such consistency indicate that the observed measurement uncertainty is not attributable to R_S but rather to the overall measurement

circuit. Consequently, this standard deviation can be considered as the uncertainty of the setup and of the proposed measurement system.

Chapter 8

Conclusions

8.1 Research activity overview and outcomes

Considering the growing interest in noncontact sensing, in the present thesis innovative techniques, circuits and devices for contactless sensing through wireless coupling have been studied and presented. The research highlights how noncontact sensing systems boost flexibility, broaden the range of monitoring applications, and unlock new opportunities in many scenarios from industrial to healthcare applications.

The thesis distinguishes between distant wireless sensing and proximate noncontact sensing, operating in the electromagnetic far field and near field, respectively. Each domain is characterized by specific technologies, applications, and methodologies that reflect their operational range and underlying principles.

In the scenario of distant noncontact sensing, the thesis examines the use of electromagnetic waves for unobtrusive level monitoring. This technology relies on the interaction of electromagnetic waves with objects to extract information about their properties and position.

In particular, a radar system for unobtrusive level monitoring of granular solids, such as grains, flour, sand, or feed stored in silos, has been presented. The proposed system is based on a commercial 76-81 GHz frequency-modulated continuous-wave (FMCW) radar sensor and a Raspberry Pi board to acquire the data and manage a remote communication through Wi-Fi connection. A tailored algorithm has been devised to process the reflected power measured by the system, thereby improving the signal-to-noise ratio and the accuracy of the material level estimation inside the silo. The developed prototype has been installed

outside the top face of a circular fiberglass silo containing sound-absorbing, granular and dusty material. The system has been tested for 15 consecutive days during which the silo has been loaded and progressively unloaded in the level range between 0.5 and 5.2 m. The effectiveness of the system has been verified comparing the estimated level of the material inside the silo, obtained exploiting the radar, with those from the load cells system. The resolution has been estimated as 0.037 m performing repeated measurements at a fixed level. This application underscores the effectiveness of the distant noncontact sensing in agriculture and industrial applications.

In the domain of noncontact proximate sensing, the thesis provides an in-depth analysis of noncontact interrogation of passive sensors. It analyses the operation of the contactless interrogation of resonant passive sensors, highlighting the principles of inductive coupling and the exploration of the resonant frequency and quality factor as principal readout signals. The thesis studies different typologies of sensor units and interrogation techniques, analysing the challenges of obtaining distance-independent measurements and proposing mitigation strategies to enhance reliability and accuracy. The proposed approach opens up new possibilities for creating low-cost, disposable, and implantable devices, particularly in healthcare and industrial applications, due to their operation without the need for active electronics.

In this scenario, a system for the noncontact measurement of the resonant response of piezoelectric thin-film piezoelectric on silicon aluminium nitride (TPoS AlN) disk MEMS resonators, vibrating at 6.33 MHz in contour mode, has been presented. The proposed technique leverages the magnetic coupling between the interrogation and sensor units, switching between excitation and detection phases. The readout signal is appropriately down-mixed with a local oscillator, and the resonator frequency measurement is accomplished through a sophisticated post-processing approach based on autocorrelation. The proposed approach has been applied for temperature sensing, exploiting the capabilities of the MEMS resonator as a passive temperature sensor with contactless readout. The temperature coefficient of frequency (TCF) of the resonator has been determined, obtaining values of 46.7 ppm/°C and of 47.4 ppm/°C for contact and

noncontact measurements, respectively. The measurements obtained using the proposed technique, in good agreement with the reference measurements, exhibit independence from interrogation distance and robust performance in terms of signal-to-noise ratio (SNR). The presented approach does not require bulky bench instrumentation for resonant frequency readout, thereby allowing the development of compact devices tailored for the noncontact interrogation of piezoelectric resonators. The activity carried out has lead to the development of a versatile platform based on MEMS device that can be further applied for applications in different scenarios.

In the same field of the proximate sensing, a passive flexible patch for body temperature measurements, combining contact sensing with contactless readout by a nearby interrogation unit, has been presented for healthcare applications. The flexible patch, forming the sensor unit, is composed of an inductive copper coil for magnetic coupling, a ceramic capacitor as the temperature-sensing element based on its temperature coefficient of capacitance (TCC) and an additional inductor to make the resonant frequency of the resulting resonant RLC circuit independent from the bending of the patch. The contactless reading exploits magnetic coupling between the interrogation and sensor units and operates exploiting a time-gated technique by switching between excitation and detection phases. The readout signal, at a frequency of 1.63 MHz, is down-mixed with a reference signal and the frequency of the sensor unit related to the measured temperature is obtained by a digital elaboration based on autocorrelation. A proof-of-concept prototype has been developed by employing a paper-based flexible patch and off-the-shelf components. The prototype has been experimentally tested within the temperature range 32 - 46 °C, giving a sensitivity of 619.8 Hz/°C and a resolution of 0.06 °C. Thanks to the additional inductor introduced in the resonant RLC circuit of the patch, the maximum variation of the resonant frequency due to the effect of the patch bending has been reduced to 7.5 ppm for a minimum curvature radius of 73 mm, leading to an equivalent maximum error in temperature reading of 0.019 °C.

As a further exploration of the proximate sensing, the thesis presents the development and testing of a contactless interrogation method for an inductive sensor designed for the

detection of conductive targets. The sensor, comprising a solenoidal coil around a plastic pipe and connected to a capacitor, forms an LC circuit resonating at a frequency of 2.51 MHz. This frequency, used as readout signal, is altered by the presence of a conductive target nearby the inductive sensor. The proposed approach has been tested to detect a conductive lead sphere up to 7.5 mm from the center of the coil, achieving a frequency variation of 180 kHz when the sphere is at the center of the coil. This detection capability is minimally influenced by the interrogation distance between the inductive sensor and the interrogation coil. However, it will be possible to apply techniques already known in the literature to compensate for this dependence, thereby guaranteeing the effectiveness of the proposed contactless interrogation technique. The sensor versatility of the sensor to be adapted to various target sizes and materials highlights its potential for widespread applications in industrial monitoring, machinery maintenance, and contamination control. Further developments could be addressed towards refining the geometry and the technology used to realize the sensor, particularly in enhancing its sensitivity for smaller-scale targets. This innovative approach offers a versatile and reliable solution for a wide array of applications.

As the final topic in the field of noncontact proximate sensing, this thesis presents an advanced technique for the contactless interrogation of passive resistive sensors exploiting QCR (Quartz Crystal Resonators) as resonant element. The novel method for contactless interrogation of a resistive element is based on the quality factor estimation. Exploiting the frequency stability and high quality factor of a QCR, the proposed method enables accurate sensor resistance estimation, independent of the interrogation distance. Experimental validations of the proposed method, have consistently demonstrated its reliability and adaptability, covering a range of resistive sensing element from 10 Ω to 1100 Ω and varying interrogation distances from 1 mm to 10 mm. The equivalent resolution at one sigma, determined through short-term repeated measurements, has been found to be 9.1 mΩ. Upon conducting long-term repeated measurements, the equivalent resolution at one sigma yields a value of 18.5 mΩ. The proposed method provides distance-independent accurate readings addressing key limitations in existing technologies, and representing a significant advancement in the contactless interrogation of passive sensors. This

advancement broadens the scope for using resistive sensing elements within the context of contactless interrogation of passive sensors, thereby enhancing their applicability and versatility across a range of technological domains.

In summary, this thesis underscores the application and technological advancements of noncontact sensing through wireless coupling and demonstrates the versatility of the proposed approaches, both in the fields of distant and proximate noncontact sensing. The integration of innovative sensor technologies, coupled with advanced computational methods, makes noncontact sensing via wireless coupling a pivotal technology for applications ranging from industrial monitoring to healthcare, providing a solid platform for future innovations in these fields.

Bibliography

[1] Kairu, E.N. An Introduction to Remote Sensing. *GeoJournal* **1982**, *6*, 251–260

[2] Air Anti-Submarine Warfare ASW Sensors Available online: https://www.globalsecurity.org/military/systems/aircraft/asw3.htm (accessed on 14 December 2023)

[3] Seitz, P.K.; Karger, C.P.; Bendl, R.; Schwahofer, A. Strategy for Automatic Ultrasound (US) Probe Positioning in Robot-Assisted Ultrasound Guided Radiation Therapy. *Phys. Med. Biol.* **2023**, *68*, 045007, doi:10.1088/1361-6560/acaf46

[4] Erdogmus, E.; Garcia, E.; Amiri, A.S.; Schuller, M. A Novel Structural Health Monitoring Method for Reinforced Concrete Bridge Decks Using Ultrasonic Guided Waves. *Infrastructures* **2020**, *5*, 49, doi:10.3390/infrastructures5060049

[5] Sarvazyan, A.P.; Urban, M.W.; Greenleaf, J.F. Acoustic Waves in Medical Imaging and Diagnostics. *Ultrasound Med. Biol.* **2013**, *39*, 1133–1146, doi:10.1016/j.ultrasmedbio.2013.02.006

[6] Marty, P.; Boehm, C.; Fichtner, A. Shape Optimization for Transcranial Ultrasound Computed Tomography. In Proceedings of the Medical Imaging 2023: Ultrasonic Imaging and Tomography; SPIE, April 10 2023; Vol. 12470, pp. 77–88

[7] Harvey, G.; Gachagan, A.; Mutasa, T. Review of High-Power Ultrasound-Industrial Applications and Measurement Methods. *IEEE Trans. Ultrason. Ferroelectr. Freq. Control* **2014**, *61*, 481–495, doi:10.1109/TUFFC.2014.2932

[8] Prasetyono, A.P.; Adiyasa, I.W.; Yudianto, A.; Agit, S.N.K. Multiple Sensing Method Using Moving Average Filter for Automotive Ultrasonic Sensor. *J. Phys. Conf. Ser.* **2020**, *1700*, 012075, doi:10.1088/1742-6596/1700/1/012075

[9] Khalil, U.; Nasir, A.; Khan, S.M.; Javid, T.; Raza, S.A.; Siddiqui, A. Automatic Road Accident Detection Using Ultrasonic Sensor. In Proceedings of the 2018 IEEE 21st International Multi-Topic Conference (INMIC); November 2018; pp. 206–212

[10] Kohler, P.; Connette, C.; Verl, A. Vehicle Tracking Using Ultrasonic Sensors & Joined Particle Weighting. In Proceedings of the 2013 IEEE International Conference on Robotics and Automation; IEEE: Karlsruhe, Germany, May 2013; pp. 2900–2905

[11] Mehrotra, P.; Chatterjee, B.; Sen, S. EM-Wave Biosensors: A Review of RF, Microwave, Mm-Wave and Optical Sensing. *Sensors* **2019**, *19*, 1013, doi:10.3390/s19051013

[12] Electromagnetic Radiation Sensors. *Sens. Rev.* **2008**, *28*, doi:10.1108/sr.2008.08728caa.002

[13] Wei, X.; Chang, N.-B.; Bai, K.; Gao, W. Satellite Remote Sensing of Aerosol Optical Depth: Advances, Challenges, and Perspectives. *Crit. Rev. Environ. Sci. Technol.* **2020**, *50*, 1640–1725, doi:10.1080/10643389.2019.1665944

[14] Ergün, S.; Sönmez, S. Terahertz Technology For Military Applications. *J. Manag. Inf. Sci.* **2015**, *3*, 13–16, doi:10.17858/jmisci.58124

[15] Frau, I.; Korostynska, O.; Mason, A.; Byrne, P.A. Comparison of Electromagnetic Wave Sensors with Optical and Low-Frequency Spectroscopy Methods for Real-Time Monitoring of Lead Concentrations in Mine Water. *Mine Water Environ.* **2018**, doi:10.1007/s10230-018-0511-7

[16] Altaf, M.A.; Ahn, J.; Khan, D.; Kim, M.Y. Usage of IR Sensors in the HVAC Systems, Vehicle and Manufacturing Industries: A Review. *IEEE Sens. J.* **2022**, *22*, 9164–9176, doi:10.1109/JSEN.2022.3166190

[17] Pauli, M.; Göttel, B.; Scherr, S.; Bhutani, A.; Ayhan, S.; Winkler, W.; Zwick, T. Miniaturized Millimeter-Wave Radar Sensor for High-Accuracy Applications. *IEEE Trans. Microw. Theory Tech.* **2017**, *65*, 1707–1715, doi:10.1109/TMTT.2017.2677910

[18] Hasch, J.; Topak, E.; Schnabel, R.; Zwick, T.; Weigel, R.; Waldschmidt, C. Millimeter-Wave Technology for Automotive Radar Sensors in the 77 GHz Frequency Band. *IEEE Trans. Microw. Theory Tech.* **2012**, *60*, 845–860, doi:10.1109/TMTT.2011.2178427

[19] Vaddi, R.; kumar, M.A.; Boggavarapu, L.N.P. A Survey on Electromagnetic Radiation Based Remote Sensing Applications to Agriculture. In Proceedings of the 2020 3rd International Conference on Intelligent Sustainable Systems (ICISS); December 2020; pp. 1197–1202

[20] Li, C.; Lubecke, V.M.; Boric-Lubecke, O.; Lin, J. A Review on Recent Advances in Doppler Radar Sensors for Noncontact Healthcare Monitoring. *IEEE Trans. Microw. Theory Tech.* **2013**, *61*, 2046–2060, doi:10.1109/TMTT.2013.2256924

[21] Watson-Watt, R. Radar in War and in Peace. *Nature* **1945**, *156*, 319–324, doi:10.1038/156319a0

[22] Chen, X.; Huang, W. Identification of Rain and Low-Backscatter Regions in X-Band Marine Radar Images: An Unsupervised Approach. *IEEE Trans. Geosci. Remote Sens.* **2020**, *58*, 4225–4236, doi:10.1109/TGRS.2019.2961807

[23] Matrosov, S.Y.; Clark, K.A.; Martner, B.E.; Tokay, A. X-Band Polarimetric Radar Measurements of Rainfall. *J. Appl. Meteorol. Climatol.* **2002**, *41*, 941–952, doi:10.1175/1520-0450(2002)041<0941:XBPRMO>2.0.CO;2

[24] Evers, C.; Smith, A.; Lee, D. Application of Radar Multistatic Techniques to Air Traffic Control. In Proceedings of the Record of the IEEE 2000 International Radar Conference [Cat. No. 00CH37037]; May 2000; pp. 763–768

[25] Ahmad, F.; Amin, M.G. Noncoherent Approach to Through-the-Wall Radar Localization. *IEEE Trans. Aerosp. Electron. Syst.* **2006**, *42*, 1405–1419, doi:10.1109/TAES.2006.314581

[26] Li, J.; Zeng, Z.; Sun, J.; Liu, F. Through-Wall Detection of Human Being's Movement by UWB Radar. *IEEE Geosci. Remote Sens. Lett.* **2012**, *9*, 1079–1083, doi:10.1109/LGRS.2012.2190707

[27] What Are Millimeter Waves? - Everything RF Available online: https://www.everythingrf.com/community/what-are-millimeter-waves (accessed on 1 December 2023)

[28] Droitcour, A.D.; Boric-Lubecke, O.; Lubecke, V.M.; Lin, J.; Kovacs, G.T.A. Range Correlation and I/Q Performance Benefits in Single-Chip Silicon Doppler Radars for Noncontact Cardiopulmonary Monitoring. *IEEE Trans. Microw. Theory Tech.* **2004**, *52*, 838–848, doi:10.1109/TMTT.2004.823552

[29] Li, C.; Yu, X.; Lee, C.-M.; Li, D.; Ran, L.; Lin, J. High-Sensitivity Software-Configurable 5.8-GHz Radar Sensor Receiver Chip in 0.13-μ m CMOS for Noncontact Vital Sign Detection. *Microw. Theory Tech. IEEE Trans. On* **2010**, *58*, 1410–1419, doi:10.1109/TMTT.2010.2042856

[30] Zhang, Y.P.; Liu, D. Antenna-on-Chip and Antenna-in-Package Solutions to Highly Integrated Millimeter-Wave Devices for Wireless Communications. *IEEE Trans. Antennas Propag.* **2009**, *57*, 2830–2841, doi:10.1109/TAP.2009.2029295

[31] Peng, Z.; Li, C. Portable Microwave Radar Systems for Short-Range Localization and Life Tracking: A Review. *Sensors* **2019**, *19*, 1136, doi:10.3390/s19051136

[32] Sorrentino, R.; Sbarra, E.; Urbani, L.; Montori, S.; Gatti, R.V.; Marcaccioli, L. Accurate FMCW Radar-Based Indoor Localization System. In Proceedings of the 2012 IEEE International Conference on RFID-Technologies and Applications (RFID-TA); November 2012; pp. 362–368

[33] Gu, C. Short-Range Noncontact Sensors for Healthcare and Other Emerging Applications: A Review. *Sensors* **2016**, *16*, 1169, doi:10.3390/s16081169

[34] Rahman, T.; Adams, A.; Ravichandran, R.; Zhang, M.; Patel, S.; Kientz, J.; Choudhury, T. *DoppleSleep: A Contactless Unobtrusive Sleep Sensing System Using Short-Range Doppler Radar*; 2015;

[35] Li, C.; Peng, Z.; Huang, T.-Y.; Fan, T.; Wang, F.-K.; Horng, T.-S.; Muñoz-Ferreras, J.-M.; Gómez-García, R.; Ran, L.; Lin, J. A Review on Recent Progress of Portable Short-Range Noncontact Microwave Radar Systems. *IEEE Trans. Microw. Theory Tech.* **2017**, *65*, 1692–1706, doi:10.1109/TMTT.2017.2650911

[36] Peng, Z.; Muñoz-Ferreras, J.-M.; Gómez-García, R.; Ran, L.; Li, C. 24-GHz Biomedical Radar on Flexible Substrate for ISAR Imaging. In Proceedings of the 2016 IEEE MTT-S International Wireless Symposium (IWS); March 2016; pp. 1–4

[37] Maaref, N.; Millot, P.; Pichot, Ch.; Picon, O. A Study of UWB FM-CW Radar for the Detection of Human Beings in Motion Inside a Building. *IEEE Trans. Geosci. Remote Sens.* **2009**, *47*, 1297–1300, doi:10.1109/TGRS.2008.2010709

[38] Morgan, A.M. Ultra-Wideband Impulse Scattering Measurements. *IEEE Trans. Antennas Propag.* **1994**, *42*, 840–846, doi:10.1109/8.301704

[39] Droitcour, A.D.; Boric-Lubecke, O.; Lubecke, V.M.; Lin, J. 0.25 /Spl Mu/m CMOS and BiCMOS Single-Chip Direct-Conversion Doppler Radars for Remote Sensing of Vital Signs. In Proceedings of the 2002 IEEE International Solid-State Circuits Conference. Digest of Technical Papers (Cat. No.02CH37315); February 2002; Vol. 1, pp. 348–349 vol.1

[40] Changzhan Gu; Ruijiang Li; Hualiang Zhang; Fung, A.Y.C.; Torres, C.; Jiang, S.B.; Changzhi Li Accurate Respiration Measurement Using DC-Coupled Continuous-Wave Radar Sensor for Motion-Adaptive Cancer Radiotherapy. *IEEE Trans. Biomed. Eng.* **2012**, *59*, 3117–3123, doi:10.1109/TBME.2012.2206591

[41] Al-Hourani, A.; Evans, R.; Farrell, P.; Moran, B.; Martorella, M.; Sithamparanathan, K.; Skafidas, S.; Parampalli, U. Millimeter-Wave Integrated Radar Systems and Techniques. In *Academic Press Library in Signal Processing, Volume 7*; 2017

[42] Parra, Y.G.; Guzmán B, T.; González P, J.T.; Parra, Y.G.; Guzmán B, T.; González P, J.T. Development of a Low-Cost, Short-Range Radar System to Measure Speed and Distance. *Tecciencia* **2017**, *12*, 99–106, doi:10.18180/tecciencia.2017.22.11

[43] Jeong, S.H.; Lee, J.E.; Choi, S.U.; Oh, J.N.; Lee, K.H. Technology Analysis and Low-Cost Design of Automotive Radar for Adaptive Cruise Control System. *Int. J. Automot. Technol.* **2012**, *13*, 1133–1140, doi:10.1007/s12239-012-0116-2

[44] Li, Y.; Peng, Z.; Pal, R.; Li, C. Potential Active Shooter Detection Based on Radar Micro-Doppler and Range-Doppler Analysis Using Artificial Neural Network. *IEEE Sens. J.* **2019**, *19*, 1052–1063, doi:10.1109/JSEN.2018.2879223

[45] Dincer, C.; Bruch, R.; Costa-Rama, E.; Fernández-Abedul, M.T.; Merkoçi, A.; Manz, A.; Urban, G.A.; Güder, F. Disposable Sensors in Diagnostics, Food, and Environmental Monitoring. *Adv. Mater.* **2019**, *31*, 1806739, doi:10.1002/adma.201806739

[46] Olenik, S.; Lee, H.S.; Güder, F. The Future of Near-Field Communication-Based Wireless Sensing. *Nat. Rev. Mater.* **2021**, *6*, 286–288, doi:10.1038/s41578-021-00299-8

[47] Li, C.; Tan, Q.; Jia, P.; Zhang, W.; Liu, J.; Xue, C.; Xiong, J. Review of Research Status and Development Trends of Wireless Passive LC Resonant Sensors for Harsh Environments. *Sensors* **2015**, *15*, 13097–13109, doi:10.3390/s150613097

[48] Lu, D.; Yan, Y.; Avila, R.; Kandela, I.; Stepien, I.; Seo, M.; Bai, W.; Yang, Q.; Li, C.; Haney, C.R.; et al. Bioresorbable, Wireless, Passive Sensors as Temporary Implants for Monitoring Regional Body Temperature. *Adv. Healthc. Mater.* **2020**, *9*, 2000942, doi:10.1002/adhm.202000942

[49] Zhang, G.; Tan, Q.; Lin, B.; Xiong, J. A Novel Temperature and Pressure Measuring Scheme Based on LC Sensor for Ultra-High Temperature Environment. *IEEE Access* **2019**, *7*, 162747–162755, doi:10.1109/ACCESS.2019.2938834

[50] Masud, M.; Vazquez, P.; Rehman, M.R.U.; Elahi, A.; Wijns, W.; Shahzad, A. Measurement Techniques and Challenges of Wireless LC Resonant Sensors: A Review. *IEEE Access* **2023**, *11*, 95235–95252, doi:10.1109/ACCESS.2023.3309300

[51] Demori, M.; Baù, M.; Ferrari, M.; Ferrari, V. Interrogation Techniques and Interface Circuits for Coil-Coupled Passive Sensors. *Micromachines* **2018**, *9*, 449, doi:10.3390/mi9090449

[52] Cao, Z.; Chen, P.; Ma, Z.; Li, S.; Gao, X.; Wu, R.; Pan, L.; Shi, Y. Near-Field Communication Sensors. *Sensors* **2019**, *19*, 3947, doi:10.3390/s19183947

[53] Huang, Q.-A.; Dong, L.; Wang, L.-F. LC Passive Wireless Sensors Toward a Wireless Sensing Platform: Status, Prospects, and Challenges. *J. Microelectromechanical Syst.* **2016**, *25*, 822–841, doi:10.1109/JMEMS.2016.2602298

[54] Kang, M.H.; Lee, G.J.; Yun, J.H.; Song, Y.M. NFC-Based Wearable Optoelectronics Working with Smartphone Application for Untact Healthcare. *Sensors* **2021**, *21*, 878, doi:10.3390/s21030878

[55] Lazaro, A.; Villarino, R.; Lazaro, M.; Canellas, N.; Prieto-Simon, B.; Girbau, D. Recent Advances in Batteryless NFC Sensors for Chemical Sensing and Biosensing. *Biosensors* **2023**, *13*, 775, doi:10.3390/bios13080775

[56] Calpa, E.U.; Pastrana, H.F.; Caro, C.D.; Becerra, D.S.; Segura-Quijano, F.E. NFC-Enabled Passive Sensor for the Quality Control of Ethanol Against SARS-CoV-2. *IEEE Sens. J.* **2021**, *21*, 23608–23613, doi:10.1109/JSEN.2021.3109802

[57] Escobedo, P.; Bhattacharjee, M.; Nikbakhtnasrabadi, F.; Dahiya, R. Smart Bandage With Wireless Strain and Temperature Sensors and Batteryless NFC Tag. *IEEE Internet Things J.* **2021**, *8*, 5093–5100, doi:10.1109/JIOT.2020.3048282

[58] Liu, Z.; Shen, Y.; Zhao, S.; Bai, J.; Ma, R.; Gao, S.; Liu, W.; Zhao, Q. A Novel-Structure LC Resonant Passive Wireless Sensor for NO2 Sensing. *Chemosensors* **2023**, *11*, 359, doi:10.3390/chemosensors11070359

[59] Collins, C.C. Miniature Passive Pressure Transensor for Implanting in the Eye. *IEEE Trans. Biomed. Eng.* **1967**, *BME-14*, 74–83, doi:10.1109/TBME.1967.4502474

[60] Yang, B.; Meng, F.; Dong, Y. A Coil-Coupled Sensor for Electrolyte Solution Conductivity Measurement. In Proceedings of the Proceedings of 2013 2nd

International Conference on Measurement, Information and Control; August 2013; Vol. 01, pp. 57–60

[61] Tommaso, A.; Carli, F.; Ada, F.; Micheletti, F.; Panzardi, E.; Vignoli, V. Telemetric QCM-D Based Sensing System with Adaptive Excitation Frequency. In Proceedings of the 2022 IEEE Sensors Applications Symposium (SAS); August 2022; pp. 1–6

[62] Ferrari, M.; Baù, M.; Tonoli, E.; Ferrari, V. Piezoelectric Resonant Sensors with Contactless Interrogation for Mass-Sensitive and Acoustic-Load Detection. *Sens. Actuators Phys.* **2013**, *202*, 100–105, doi:10.1016/j.sna.2013.04.029

[63] Bau', M.; Zini, M.; Nastro, A.; Ferrari, M.; Ferrari, V.; Lee, J.E.-Y. Electronic Technique and System for Non-Contact Reading of Temperature Sensors Based on Piezoelectric MEMS Resonators. In Proceedings of the 2022 IEEE International Symposium on Circuits and Systems (ISCAS); May 2022; pp. 2409–2413

[64] Andò, B.; Baglio, S.; Savalli, N.; Trigona, C. Cascaded "Triple-Bent-Beam" MEMS Sensor for Contactless Temperature Measurements in Nonaccessible Environments. *IEEE Trans. Instrum. Meas.* **2011**, *60*, 1348–1357, doi:10.1109/TIM.2010.2101310

[65] Baù, M.; Ferrari, M.; Ferrari, V. Flexible Passive Temperature Sensor Label with Contactless Interrogation. In Proceedings of the 2019 IEEE International Conference on Flexible and Printable Sensors and Systems (FLEPS); July 2019; pp. 1–3

[66] Nopper, R.; Has, R.; Reindl, L. A Wireless Sensor Readout System—Circuit Concept, Simulation, and Accuracy. *IEEE Trans. Instrum. Meas.* **2011**, *60*, 2976–2983, doi:10.1109/TIM.2011.2122110

[67] Park, J.-Y.; Choi, J.-W. Review—Electronic Circuit Systems for Piezoelectric Resonance Sensors. *J. Electrochem. Soc.* **2020**, *167*, 037560, doi:10.1149/1945-7111/ab6cf7

[68] Ferrari, M.; Baù, M.; Pagnoni, M.; Ferrari, V. Compact DDS-Based System for Contactless Interrogation of Resonant Sensors Based on Time-Gated Technique. In Proceedings of the 2014 IEEE SENSORS; November 2014; pp. 907–910

[69] Karuppuswami, S.; Mondal, S.; Kumar, D.; Kaur, A.; Chahal, P. Thin-Film Based Passive RFID Sensor Tag for Detection of Packaged Food Volatiles. *Int. Symp. Microelectron.* **2019**, *2019*, 000599–000602, doi:10.4071/2380-4505-2019.1.000599

[70] Roy, S.; Chan, Y.J.; Reuel, N.F.; Neihart, N.M. Low-Cost Portable Readout System Design for Inductively Coupled Resonant Sensors. *IEEE Trans. Instrum. Meas.* **2022**, *71*, 1–13, doi:10.1109/TIM.2022.3173277

[71] Michael Vogt; Gerding, M. Silo and Tank Vision: Applications, Challenges, and Technical Solutions for Radar Measurement of Liquids and Bulk Solids in Tanks and Silos. *IEEE Microw. Mag.* **2017**, *18*, 38–51, doi:10.1109/MMM.2017.2711978

[72] Ryde, J.; Hillier, N. Performance of Laser and Radar Ranging Devices in Adverse Environmental Conditions. *J. Field Robot.* **2009**, *26*, 712–727, doi:10.1002/rob.20310

[73] Panda, K.G.; Agrawal, D.; Nshimiyimana, A.; Hossain, A. Effects of Environment on Accuracy of Ultrasonic Sensor Operates in Millimetre Range. *Perspect. Sci.* **2016**, *8*, 574–576, doi:10.1016/j.pisc.2016.06.024

[74] Lin, J.; Li, C.; Chang, C.-C.; Tsai, T.-H.; Zito, D.; Chang, S.-F. Review —Semiconductor Integrated Radar for Sensing Applications. *ECS J. Solid State Sci. Technol.* **2018**, *7*, Q3126–Q3142, doi:10.1149/2.0181807jss

[75] Edvardsson, O. An FMCW Radar for Accurate Level Measurements. In Proceedings of the 1979 9th European Microwave Conference; September 1979; pp. 712–715

[76] Hsiao, T.-W.; Chang, T.-P.; Chou, H.-T.; Tuan, S.-C. A Novel Moving Average Method of Vehicle Detection in the FMCW Radar Using Antennas with Different Beamwidths at K-Band. In Proceedings of the 2015 IEEE 6th International Symposium on Microwave, Antenna, Propagation, and EMC Technologies (MAPE); October 2015; pp. 136–139

[77] Hallil, H.; Dejous, C.; Hage-Ali, S.; Elmazria, O.; Rossignol, J.; Stuerga, D.; Talbi, A.; Mazzamurro, A.; Joubert, P.-Y.; Lefeuvre, E. Passive Resonant Sensors: Trends and Future Prospects. *IEEE Sens. J.* **2021**, *21*, 12618–12632, doi:10.1109/JSEN.2021.3065734

[78] Stemme, G. Resonant Silicon Sensors. *J. Micromechanics Microengineering* **1991**, *1*, 113, doi:10.1088/0960-1317/1/2/004

[79] Elwenspoek, M.; Blom, F.R.; Bouwstra, S.; Lammerink, T.S.J.; van de Pol, F.C.M.; Tilmans, H.A.C.; Popma, T.J.A.; Fluitman, J.H.J. Transduction Mechanisms and Their Applications in Micromechanical Devices. In Proceedings of the IEEE Micro Electro Mechanical Systems, , Proceedings, “An Investigation of Micro Structures, Sensors, Actuators, Machines and Robots”; February 1989; pp. 126–132

[80] Brand, O. CMOS-Based Resonant Sensors. In Proceedings of the 2005 IEEE SENSORS; October 2005; p. 4 pp.-

[81] Langdon, R.M. Resonator Sensors-a Review. *J. Phys. [E]* **1985**, *18*, 103, doi:10.1088/0022-3735/18/2/002

[82] Ferrari, V.; Gatti, Paolo Luciano Applied Structural and Mechanical Vibrations: Theory, Methods, and Measuring Instrumentation. *Choice Rev. Online* **2000**, *38*, 38-0959-38–0959, doi:10.5860/CHOICE.38-0959

[83] LIGO-Labcit Available online: https://labcit.ligo.caltech.edu/~ajw/ph106/Files_ph106a/ph106a_2019_L7.pdf (accessed on 21 December 2023)

[84] Su, Y.P.; Liu, X.; Hui, S.Y.R. Mutual Inductance Calculation of Movable Planar Coils on Parallel Surfaces. *IEEE Trans. Power Electron.* **2009**, *24*, 1115–1123, doi:10.1109/TPEL.2008.2009757

[85] Chin-Hsiung, L. 1; Hu, Q. 2 1 C. of R. Mutual Inductance Measurement and Analysis of Near-Field Magnetic Coupling. **2019**, doi:10.1088/1757-899X/612/4/042003

[86] Hussain, I.; Woo, D.-K. Simplified Mutual Inductance Calculation of Planar Spiral Coil for Wireless Power Applications. *Sensors* **2022**, *22*, 1537, doi:10.3390/s22041537

[87] Morshed, B.I. Dual Coil for Remote Probing of Signals Using Resistive Wireless Analog Passive Sensors (rWAPS). In Proceedings of the 2016 United States National Committee of URSI National Radio Science Meeting (USNC-URSI NRSM); January 2016; pp. 1–2

[88] Arnau, A.; Ferrari, V.; Soares, D.; Perrot, H. Interface Electronic Systems for AT-Cut QCM Sensors: A Comprehensive Review. In *Piezoelectric Transducers and Applications*; Vives, A.A., Ed.; Springer: Berlin, Heidelberg, 2008; pp. 117–186 ISBN 978-3-540-77508-9

[89] Demori, M.; Baù, M.; Ferrari, M.; Ferrari, V. Electronic Technique and Circuit Topology for Accurate Distance-Independent Contactless Readout of Passive LC Sensors. *AEU - Int. J. Electron. Commun.* **2018**, *92*, 82–85, doi:10.1016/j.aeue.2018.05.019

[90] Ferrari, M.; Baù, M.; Masud, M.; Ferrari, V. A Time-Gated Contactless Interrogation System for Frequency and Quality Factor Tracking in QCR to Investigate on Liquid Solution Microdroplets. *Procedia Eng.* **2016**, *168*, 704–707, doi:10.1016/j.proeng.2016.11.252

[91] Baù, M.; Demori, M.; Ferrari, M.; Ferrari, V. Contactless Readout of Passive LC Sensors with Compensation Circuit for Distance-Independent Measurements. *Proceedings* **2018**, *2*, 842, doi:10.3390/proceedings2130842

[92] Finkbeiner, S. MEMS for Automotive and Consumer Electronics. In Proceedings of the 2013 Proceedings of the ESSCIRC (ESSCIRC); September 2013; pp. 9–14

[93] Chang, S.-C. (Scott) MEMS in Automobiles. In *Microsystems and Nanotechnology*; Zhou, Z., Wang, Z., Lin, L., Eds.; Springer: Berlin, Heidelberg, 2012; pp. 721–757 ISBN 978-3-642-18293-8

[94] Tiwari, S.; Vinchurkar, M.; Rao, V.R.; Garnier, G. Zinc Oxide Nanorods Functionalized Paper for Protein Preconcentration in Biodiagnostics. *Sci. Rep.* **2017**, *7*, 43905, doi:10.1038/srep43905

[95] Fang, H.-B.; Liu, J.-Q.; Xu, Z.-Y.; Dong, L.; Wang, L.; Chen, D.; Cai, B.-C.; Liu, Y. Fabrication and Performance of MEMS-Based Piezoelectric Power Generator for Vibration Energy Harvesting. *Microelectron. J.* **2006**, *37*, 1280–1284, doi:10.1016/j.mejo.2006.07.023

[96] Fraters, A.; Segers, T.; van den Berg, M.; Reinten, H.; Wijshoff, H.; Lohse, D.; Versluis, M. Shortwave Infrared Imaging Setup to Study Entrained Air Bubble Dynamics in a MEMS-Based Piezo-Acoustic Inkjet Printhead. *Exp. Fluids* **2019**, *60*, 123, doi:10.1007/s00348-019-2772-8

[97] Tilmans, H.A.C.; Raedt, W.D.; Beyne, E. MEMS for Wireless Communications: 'From RF-MEMS Components to RF-MEMS-SiP.' *J. Micromechanics Microengineering* **2003**, *13*, S139, doi:10.1088/0960-1317/13/4/323

[98] Pillai, G.; Li, S.-S. Piezoelectric MEMS Resonators: A Review. *IEEE Sens. J.* **2021**, *21*, 12589–12605, doi:10.1109/JSEN.2020.3039052

[99] Li, S.-S. CMOS-MEMS Resonators and Their Applications. In Proceedings of the 2013 Joint European Frequency and Time Forum & International Frequency Control Symposium (EFTF/IFC); July 2013; pp. 915–921

[100] Miandoab, E.; Pishkenari, H.N.; Yousefi-Koma, A.; Tajaddodianfar, F.; Ouakad, H. Size Effect Impact on the Mechanical Behavior of an Electrically Actuated Polysilicon Nanobeam Based NEMS Resonator. *J. Appl. Comput. Mech.* **2017**, *3*, 135–143, doi:10.22055/jacm.2017.21538.1106

[101] Nguyen, C.T.-C. RF MEMS for Wireless Applications. In Proceedings of the 60th DRC. Conference Digest Device Research Conference; June 2002; pp. 9–12

[102] Low-Power MEMS-Based Pierce Oscillator Using a 61-MHz Capacitive-Gap Disk Resonator | IEEE Journals & Magazine | IEEE Xplore Available online: https://ieeexplore.ieee.org/document/8970354 (accessed on 21 December 2023)

[103] Chu, C.-C.; Dey, S.; Liu, T.-Y.; Chen, C.-C.; Li, S.-S. Thermal-Piezoresistive SOI-MEMS Oscillators Based on a Fully Differential Mechanically Coupled Resonator Array for Mass Sensing Applications. *J. Microelectromechanical Syst.* **2018**, *27*, 59–72, doi:10.1109/JMEMS.2017.2778307

[104] Lin, C.-M.; Chen, Y.-Y.; Felmetsger, V.V.; Vigevani, G.; Senesky, D.G.; Pisano, A.P. Micromachined Aluminum Nitride Acoustic Resonators with an Epitaxial Silicon Carbide Layer Utilizing High-Order Lamb Wave Modes. In Proceedings of the 2012 IEEE 25th International Conference on Micro Electro Mechanical Systems (MEMS); January 2012; pp. 733–736

[105] Maita, F.; Maiolo, L.; Minotti, A.; Pecora, A.; Ricci, D.; Metta, G.; Scandurra, G.; Giusi, G.; Ciofi, C.; Fortunato, G. Ultraflexible Tactile Piezoelectric Sensor Based on Low-Temperature Polycrystalline Silicon Thin-Film Transistor Technology. *IEEE Sens. J.* **2015**, *15*, 3819–3826, doi:10.1109/JSEN.2015.2399531

[106] Li, J.; Zhou, X.; Zhao, H.; Shao, M.; Li, N.; Zhang, S.; Du, Y. Development of a Novel Parasitic-Type Piezoelectric Actuator. *IEEEASME Trans. Mechatron.* **2017**, *22*, 541–550, doi:10.1109/TMECH.2016.2604242

[107] Wang, J.; Zhou, S.; Zhang, Z. High-Performance Piezoelectric Wind Energy Harvester with Y-Shaped Attachments. *Energy Convers. Manag.* **2018**, *181*, 645–652, doi:10.1016/j.enconman.2018.12.034

[108] Baù, M.; Ferrari, M.; Begum, H.; Ali, A.; Lee, J.E.-Y.; Ferrari, V. Technique and Circuit for Contactless Readout of Piezoelectric MEMS Resonator Sensors. *Sensors* **2020**, *20*, 3483, doi:10.3390/s20123483

[109] Cowen, A.; Hames, G.; Glukh, K.; Hardy, B. PiezoMUMPs™ Design Handbook.

[110] Lucklum, F.; Jakoby, B. Non-Contact Liquid Level Measurement with Electromagnetic–Acoustic Resonator Sensors. *Meas. Sci. Technol.* **2009**, *20*, 124002, doi:10.1088/0957-0233/20/12/124002

[111] Baù, M.; Ferrari, M.; Ferrari, V. Analysis and Validation of Contactless Time-Gated Interrogation Technique for Quartz Resonator Sensors. *Sensors* **2017**, *17*, 1264, doi:10.3390/s17061264

[112] Analog Devices, Inc. AD9834 Rev. D Available online: https://www.analog.com/media/en/technical-documentation/data-sheets/AD9834.pdf (accessed on 21 December 2023)

[113] Maxim Integrated Products MAX301-MAX305 Precision, Dual, High-Speed Analog Switches Available online: https://www.analog.com/media/en/technical-documentation/data-sheets/MAX301-MAX305.pdf (accessed on 21 December 2023)

[114] Texas Instruments OPA657 1.6-GHz, Low-Noise, FET-Input Operational Amplifier Available online: https://www.ti.com/lit/ds/symlink/opa657.pdf (accessed on 21 December 2023)

[115] Suzuki, M.; Yanagitani, T. Temperature Coefficient of Elastic and GHz Piezoelectric Properties in ScAlN Films.

[116] Ng, E.J.; Hong, V.A.; Yang, Y.; Ahn, C.H.; Everhart, C.L.M.; Kenny, T.W. Temperature Dependence of the Elastic Constants of Doped Silicon. *J. Microelectromechanical Syst.* **2015**, *24*, 730–741, doi:10.1109/JMEMS.2014.2347205

[117] Elsayed, M.Y.; Cicek, P.-V.; Nabki, F.; El-Gamal, M.N. Bulk Mode Disk Resonator With Transverse Piezoelectric Actuation and Electrostatic Tuning. *J. Microelectromechanical Syst.* **2016**, *25*, 252–261, doi:10.1109/JMEMS.2016.2514267

[118] Cheshire, W.P. Thermoregulatory Disorders and Illness Related to Heat and Cold Stress. *Auton. Neurosci. Basic Clin.* **2016**, *196*, 91–104, doi:10.1016/j.autneu.2016.01.001

[119] Dolibog, P.; Pietrzyk, B.; Kierszniok, K.; Pawlicki, K. Comparative Analysis of Human Body Temperatures Measured with Noncontact and Contact Thermometers. *Healthcare* **2022**, *10*, 331, doi:10.3390/healthcare10020331

[120] Švantner, M.; Lang, V.; Skála, J.; Kohlschütter, T.; Honner, M.; Muzika, L.; Kosová, E. Possibilities and Limits of Human Temperature Measurement by Thermographic Methods. In Proceedings of the 2022 IEEE International Workshop on Metrology for Living Environment (MetroLivEn); May 2022; pp. 29–33

[121] Carr, A.R.; Chan, Y.J.; Reuel, N.F. Contact-Free, Passive, Electromagnetic Resonant Sensors for Enclosed Biomedical Applications: A Perspective on Opportunities and Challenges. *ACS Sens.* **2023**, doi:10.1021/acssensors.2c02552

[122] TIDA-00721 Reference Design | TI.Com Available online: https://www.ti.com/tool/TIDA-00721 (accessed on 4 May 2023)

[123] Wang, H.; Totaro, M.; Veerapandian, S.; Ilyas, M.; Kong, M.; Jeong, U.; Beccai, L. Folding and Bending Planar Coils for Highly Precise Soft Angle Sensing. *Adv. Mater. Technol.* **2020**, *5*, 2000659, doi:10.1002/admt.202000659

[124] dos Reis, D.D.; Cardoso Castaldo, F.; Pichorim, S.F. Flexible Circuits for Moisture Measurement in Cylindrical Timber of Wood. In Proceedings of the 2019 IEEE International Conference on Flexible and Printable Sensors and Systems (FLEPS); July 2019; pp. 1–3

[125] Fotheringham, G.; Ohnimus, F.; Ndip, I.; Guttowski, S.; Reichl, H. Parameterization of Bent Coils on Curved Flexible Surface Substrates for RFID Applications. In Proceedings of the 2009 59th Electronic Components and Technology Conference; May 2009; pp. 502–507

[126] Wang, Y.; Jia, Y.; Chen, Q.; Wang, Y. A Passive Wireless Temperature Sensor for Harsh Environment Applications. *Sensors* **2008**, *8*, 7982–7995, doi:10.3390/s8127982

[127] Kou, H.; Yang, L.; Zhang, X.; Shang, Z.; Shi, J.; Wang, X. A Dual LC Resonant Circuit Integrated Wireless Passive Force and Temperature Sensor for Harsh-Environment Applications. *AIP Adv.* **2022**, *12*, 065102, doi:10.1063/5.0089306

[128] Jiang, H.; Chang, Z.; Pertijs, M.A.P. A 30 Ppm Lt; 80 nJ Ring-Down-Based Readout Circuit for Resonant Sensors. *IEEE J. Solid-State Circuits* **2016**, *51*, 187–195, doi:10.1109/JSSC.2015.2470552

[129] Holder, T.; Hooper, F.S.W.; Yates, D.; Tse, Z.; Patil, S.; Moussa, A.; Batten, L.; Radhakrishnan, V.; Allison, M.; Hewitt, C.; et al. Clinical Accuracy of Infrared Temperature Measurement Devices: A Comparison against Non-Invasive Core-Body Temperature. *Clin. Med.* **2023**, *23*, 157–163, doi:10.7861/clinmed.2022-0252

[130] Dell'Isola, G.B.; Cosentini, E.; Canale, L.; Ficco, G.; Dell'Isola, M. Noncontact Body Temperature Measurement: Uncertainty Evaluation and Screening Decision Rule to Prevent the Spread of COVID-19. *Sensors* **2021**, *21*, 346, doi:10.3390/s21020346

[131] Tumanski, S. Induction Coil Sensors—a Review. *Meas. Sci. Technol.* **2007**, *18*, R31, doi:10.1088/0957-0233/18/3/R01

[132] Wang, M.; Shi, H.; Zhang, H.; Huo, D.; Xie, Y.; Su, J. Improving the Detection Ability of Inductive Micro-Sensor for Non-Ferromagnetic Wear Debris. *Micromachines* **2020**, *11*, 1108, doi:10.3390/mi11121108

[133] Study on Online Monitoring Wear Debris Sensor of Wind Turbine Gearbox - Zhang - 2019 - The Journal of Engineering - Wiley Online Library Available online: https://ietresearch.onlinelibrary.wiley.com/doi/full/10.1049/joe.2018.9192 (accessed on 20 December 2023)

[134] Flanagan, I.M.; Jordan, J.R.; Whittington, H.W. An Inductive Method for Estimating the Composition and Size of Metal Particles. *Meas. Sci. Technol.* **1990**, *1*, 381–384, doi:10.1088/0957-0233/1/5/001

[135] Hu, G.; Huang, R.; Lu, M.; Zhou, L.; Yin, W. Measurement of Radius of a Metallic Ball Using Eddy Current Testing Based on Peak Frequency Difference Feature. *Measurement* **2021**, *184*, 109876, doi:10.1016/j.measurement.2021.109876

[136] Liu, Z.; Wu, S.; Raihan, M.K.; Zhu, D.; Yu, K.; Wang, F.; Pan, X. The Optimization of Parallel Resonance Circuit for Wear Debris Detection by Adjusting Capacitance. *Energies* **2022**, *15*, 7318, doi:10.3390/en15197318

[137] Zhang, B.; Chen, X.; Yuan, J.; Zhu, H. Research on Temperature Measurement Technology of Platinum Film Thermistor. *J. Phys. Conf. Ser.* **2021**, *1907*, 012038, doi:10.1088/1742-6596/1907/1/012038

[138] Kim, K.-H.; Hong, S.K.; Jang, N.-S.; Ha, S.-H.; Lee, H.W.; Kim, J.-M. Wearable Resistive Pressure Sensor Based on Highly Flexible Carbon Composite Conductors with Irregular Surface Morphology. *ACS Appl. Mater. Interfaces* **2017**, *9*, 17499–17507, doi:10.1021/acsami.7b06119

[139] Ferrone, A.; Maiolo, L.; Minotti, A.; Pecora, A.; Iacovo, D.; Colace, L.; Grayli, S.V.; Leach, G.W.; Bahreyni, B. Flexible near Infrared Photoresistors Based on Recrystallized Amorphous Germanium Thin Films. In Proceedings of the 2016 IEEE SENSORS; October 2016; pp. 1–3

[140] Casiraghi, C.; Macucci, M.; Parvez, K.; Worsley, R.; Shin, Y.; Bronte, F.; Borri, C.; Paggi, M.; Fiori, G. Inkjet Printed 2D-Crystal Based Strain Gauges on Paper. *Carbon* **2018**, *129*, 462–467, doi:10.1016/j.carbon.2017.12.030

[141] Mazzoli, F.; Alghisi, D.; Ferrari, V. Real-Time Velocity Estimation Algorithm for a Multivariable Motion Sensor. In Proceedings of the 2022 IEEE 27th International Conference on Emerging Technologies and Factory Automation (ETFA); September 2022; pp. 1–4

[142] Mapps, D.J. Magnetoresistive Sensors. *Sens. Actuators Phys.* **1997**, *59*, 9–19, doi:10.1016/S0924-4247(97)80142-2

[143] Mirzaei, A.; Kim, J.-H.; Kim, H.W.; Kim, S.S. Resistive-Based Gas Sensors for Detection of Benzene, Toluene and Xylene (BTX) Gases: A Review. *J. Mater. Chem. C* **2018**, *6*, 4342–4370, doi:10.1039/C8TC00245B

[144] Liao, X.; Zhang, Z.; Kang, Z.; Gao, F.; Liao, Q.; Zhang, Y. Ultrasensitive and Stretchable Resistive Strain Sensors Designed for Wearable Electronics. *Mater. Horiz.* **2017**, *4*, 502–510, doi:10.1039/C7MH00071E

[145] Borghetti, M.; Cantù, E.; Sardini, E.; Serpelloni, M. Preliminary Study on Wireless Passive Resistive Sensor Applied for Smart Objects. In Proceedings of the 2021 IEEE International Workshop on Metrology for Industry 4.0 & IoT (MetroInd4.0&IoT); June 2021; pp. 150–155

[146] Bona, M.; Borghetti, M.; Sardini, E.; Serpelloni, M. Telemetric Technique for Passive Resistive Sensors Based on Impedance Real Part Measurement at Fixed Frequency. *IEEE Trans. Instrum. Meas.* **2018**, *67*, 2160–2168, doi:10.1109/TIM.2018.2811279

[147] Bona, M.; Borghetti, M.; Sardini, E.; Serpelloni, M. Novel Telemetric Technique for Passive Resistive Sensors Based on Impedance Phase Angle Measurement at Constant Frequency. In Proceedings of the 2017 IEEE International Instrumentation and Measurement Technology Conference (I2MTC); May 2017; pp. 1–6

[148] Comerford, R. An Introduction to Crystal Oscillators. *Electron. Prod.* 2015

[149] Shanghai South Ocean Electron Co.,LTD. Basic Terminology for Quartz Crystal Resonators Available online: http://www.sssoe.com/103-eng.htm (accessed on 21 December 2023)

[150] Hartz, J.; Emanetoglu, N.; Howell, C.; Vetelino, J. Lateral Field Excited Quartz Crystal Microbalances for Biosensing Applications. *Biointerphases* **2020**, *15*, 030801, doi:10.1116/6.0000144